POLITECNICO DI MILANO

DIPARTIMENTO DI MECCANICA

CORSO DI DOTTORATO IN INGEGNERIA MECCANICA

INVESTIGATION OF GEOMETRY TRANSFERABILITY OF LEMAITRE'S CONTINUUM DAMAGE MECHANICS MODEL

Nima Allahverdizadeh Shikhlou

Supervisor: Prof.Marco Giglio

Co-Supervisor: Prof.Andrea Manes

Tutor: Prof.Andrea Collina

Coordinator of Ph.D program: Prof.Bianca M.Colosimo

XXVI CICLO - 2011/2013

Abstract

Damage mechanics is one of the main frameworks dealing with failure of materials and structures. Several damage mechanics models based on different concepts have been proposed during the last decades. Lemaitre's damage mechanics model as one of the most important continuum damage mechanics models has been investigated in this research. A comprehensive experimental test program has been carried out on the different specimen geometries and loading conditions. Multiaxial torsion and uniaxial tensile tests have been done on the round and flat smooth and notched specimens. Test material is ti-6Al-4V titanium alloy. All of the experiments has been reproduced using finite element models. Lemaitre's continuum damage mechanics model and plasticity constitutive law has been calibrated for ti-6Al-4V titanium alloy and implemented into finite element models. Accuracy of the predictions of the CDM model in the different loading conditions has been evaluated especially experimental and numerical load-displacement results has been compared. Advantages and drawbacks of the Lemaitre's model have been evaluated under different loading conditions and potential errors of the application of the model have been clarified. Different loading conditions and stress states in the experiments which leads to different fracture mechanism has been shown by determination of the stress triaxiality and lode angle parameters from the finite element models. Scanning electron microscope images of the failure surface of the tested specimens has been studied and different fracture mechanisms in the experiments have been shown also.

I

Sommario

La damage mechanics é uno delle principali metodologie per affrontare il problema della modellizzazione del cedimento di componenti e strutture. Nel quadro della damage mechanics, nel corso degli anni, sono stati proposti vari modelli basati su differenti assunzioni. Il modello di Lemaitre é uno dei pi importanti tra la categoria dei modelli di tipo continuum damage mechanics. Un completo programma sperimentale basato su provini aventi differenti geometrie e sottoposti a carichi di varia natura é stato realizzato. In particolare sono state svolte prove multi e uniassiali su provini piani e a sezione circolare con e senza intaglio. Il materiale oggetto dello studio é una lega di titanio del tipo ti-6Al-4V. Tutta la campagna sperimentale é stata propriamente riprodotta numericamente sviluppando modelli agli elementi finiti. Un modello continuum damage mechanics del tipo Lemaitre e un opportuno legame costitutivo sono stati calibrati e implementati nei modelli numerici per la lega ti-6Al-4V. L'accuratezza delle predizioni del modello CDM sono state valutate confrontando in particolare le curve forza-spostamento numeriche e sperimentali. Possibili vantaggi e svantaggi del modello di Lemaitre sono state evidenziate per differenti condizioni di carico e potenziali errori del modello sono stati chiarificati. Triassilitá e angolo di Lode sono stati calcolati per differenti geometrie e carichi per mezzo dei modelli agli elementi finiti mostrando la loro influenza sulla frattura. Le superfici di frattura corrispondenti ai differenti tipi di carico sono poi state indagate utilizzando un microscopio a scansione.

Acknowledgements

Whatever you do will be insignificant, but it is very important that you do it.
(Mahatma Gandhi)

Contents

Notations

σ_H	hydrostatic stress
σ_{vm}	Von Mises stress
ε_f	plastic strain at failure
σ_1	largest principal stress
ε_p	plastic strain
ε_e	elastic strain
S	surface
S	damage model parameter
S_D	damage surface
D	scalar damage variable
M	material point
$\vec{n}$	unit normal vector
X	uniaxial kinematic back stresss
σ_y	yield stress
R	isotropic hardening internal variable
f	yield function of plastic criterion
ψ	free energy
ψ_e	elastic strain energy
ψ_p	plastic strain energy
T	temperature
Y	damage energy release rate
ρ	density
W_e	density of elastic strain energy
S_0	damage model parameter
s_0	damage model parameter
ν	Poisson's ration
M	Parameter of Romberg-Osgood equation for plastic strain hardening
K	Parameter of Romberg-Osgood equation for plastic strain hardening
$\dot{\gamma}$	plastic multiplier
$\boldsymbol{D}$	isotropic elasticity tensor
r	material parameter
r	third stress invariant
q	second stress invariant
t	time
σ_n	normal stress
υ	elastic volumetric strain
$\boldsymbol{S}$	stress deviator
p	hydrostatic pressure
q	Von Mises equivalent stress
ϕ	Von Mises type yield function
G	shear modulus
e^e	elastic strain deviator
K	bulk modulus
ν^e	elastic volumetric strain
ω	material integrity
$\varepsilon_{necking}$	necking strain
$\boldsymbol{a}$	fourth order tensor of elasticity
$\boldsymbol{q}$	heat flux
$\boldsymbol{I}$	second order identity tensor

List of Figures

List of Tables

Chapter 1

Introduction

Fracture of the structures has an old history as long as existence of the man-made structures. By improving the technology which makes the structures more and more complex, this problem is also more important and dangerous. Therefore, failure analysis of structures plays an important role in the design process. Having a comprehensive knowledge about the failure behavior of materials and the ability of forecasting fracture can significantly reduce the costs related to possible catastrophic failures of structures. There are different frame works dealing with failure in the structures and materials. Damage mechanics is one of these engineering fields which is aimed to simulate and predict degradation of materials. During last decades, several damage models have been proposed based on different approaches. However, all of these models can be classified into three main groups:

- Phenomenological models

- Porosity models

- Continuum Damage Mechanics (CDM) models

Johnson-Cook[1], Rice-Tracey[2], Leroy[3], Cockroft-Latham[4], Ayada et al.[5] are some of the most famous phenomenological damage models. Generally according to the phenomenological models failure occurs when a specific parameter defined inside the model reaches to its critical value. Equation 1.1 shows the governing equation of the phenomenological models:

$$\int_0^{\varepsilon_f} f(\boldsymbol{\sigma}, \varepsilon_f) d\varepsilon \geq C \tag{1.1}$$

Table1.1 summarizes some of the phenomenological ductile fracture criteria:

Table 1.1: Phenomenological models equations

Criterion	Formula
Rice-tracey[2]	$\int_0^{\varepsilon_f} exp(\frac{3}{2}\frac{\sigma_H}{\sigma_{vm}})d\varepsilon = C$
Leroy[3]	$\int_0^{\varepsilon_f} (\sigma_1 - \sigma_H)d\varepsilon = C$
Cockroft-Latham[4]	$\int_0^{\varepsilon_f} \frac{<\sigma_1>^1}{\sigma_{vm}}d\varepsilon = C$
Ayada[5]	$\int_0^{\varepsilon_f} \frac{\sigma_H}{\sigma_{vm}}d\varepsilon = C$
Brozzo[6]	$\int_0^{\varepsilon_f} \frac{2<\sigma_1>}{3<\sigma_1-\sigma_H>}d\varepsilon = C$
Oyane[7]	$\int_0^{\varepsilon_f} < 1+A\frac{\sigma_H}{\sigma_v m} > d\varepsilon = C$

Phenomenological models are increasingly used in the industrial applications due to their relatively easy calibration and their wide implementation in several commercial finite element codes. According to these models, failure occurs when a damage parameter reaches a critical value. Generally, phenomenological models are uncoupled, hence they assume that the damage process does not affect at all the plastic behavior of material. This assumption makes phenomenological models relatively easy to implement and to calibrate but the main drawback is that there is no physical explanation of the damage process. This lack of a strong theoretical background could potentially lead to a decrement of the model ability to predict failure for general applications. This is very true in case of complex loading conditions when commonly, loading conditions could be much different from the one adopted in the calibration stage. Bao-Wierzbicki model [8],[9] and modified Mohr-Coulomb model [10],[11] are two recently proposed popular phenomenological models due to the promising results of their application into failure simulations in very different and extreme load conditions and on real components (good geometry transferability) [12], [13], [14], [15]. It is well known that stress triaxiality plays an important role in the ductile fracture [16], [17], [18]. However, its effect commonly was considered only as a continuous ductility decrement as long as triaxiality increases (failure strain decreases with triaxiality). Bao and Wierzbicki [8],[9] questioned this assumption showing that failure strain trend

---

[1] $<>$ is the Mac Auley bracket $< x >= x$ if $x > 0$, $< x >= 0$ if $x \leq 0$.

versus the stress triaxiality is not just monotonic but it could be much more complex. Bao-Wierzbicki's model born from consideration that for different triaxiality, fracture phenomena are different. In fact, the fracture locus (stress triaxiality versus fracture strain curve) despite the other damage models, is not continuous but there are three different regions: compression, shear dominant and tension dominant. Wierzbicki et al.[8],[9] showed the existence of these discontinuities in the fracture locus for an 2024-T351 Aluminum alloy. A series of experimental tests has been done on 2024-T351 Aluminum alloy, including upsetting and tensile tests. Two totally different fracture mechanisms have been clearly observed from microfractographs of upsetting and tensile specimens. Wierzbiki et al[8] concluded that it is not possible to capture all features of ductile crack formation in different stress states with a single criterion and therefore, different functions are necessary to predict crack formation. Numerical simulations of each test has been performed and based on the experimental and numerical results, the relation between the equivalent strain to fracture versus stress triaxiality has been quantified and it has been showed that there are three different distinct branches of this function with possible slope discontinuities in the transition regime. Wierzbicki et al[8] have also lead to this result that for negative stress triaxialities, fracture is governed by shear mode. For large triaxialities void growth is the dominant failure mode, while at low stress triaxilies between above two regimes, fracture may develop as a combination of shear and void growth modes. Giglio et al.[12] also reported a similar phenomenon in Ti-6Al-4V titanium alloy. However, Bonora et al.[19] showed that fracture locus is continuous for some materials. Bonora et al.[19] have been experimentally studied the effect of stress state (by means of stress triaxiality) on the equivalent plastic strain at fracture for different steels and high purity copper in the range of stress triaxiality from 0(pure torsion) up to 1.2. In the most majority of the damage models stress triaxiality is considered as the only parameter of stress state which affects fracture locus. However, recently also the importance of another parameter, called lode angle, has been highlighted [10],[11] and the Modified Mohr-Coulomb model considers also its effect on fracture. In the Modified Mohr-Coulomb fracture locus is no longer just a curve in a 2D plane (stress triaxiality-failure strain) but it is rather a surface in the 3D space (triaxiality-lode angle- failure strain).

Porosity models are another approach to investigate fracture. The most important porosity model which is called GTN initially developed by Gurson and subse-

quently modified by Tveergaard and Neeedleman[20],[21]. Porosity models are based on micromechanical concepts and governing equations which are responsible for the effects of microvoids growth in the material. Despite the phenomenological models, porosity models are much more complex to calibrate. In GTN model, nine parameters has to be determined for each material. Damage evolution and plasticity are also coupled in porosity models which means damage evolution affect the plasticity behavior of material.

The last damage framework, which is worth to describe, is the continuum damage mechanics (CDM). Lemaitre[22] proposed the first CDM model based on the effective stress concept of Kachanov [23] and constitutive laws of thermodynamic aiming to describe ductile damage. During the last decades different CDM models have been proposed by researchers. In 1998 Bonora[24] proposed another CDM model which considers nonlinear function for the damage evolution and is different from Lemaitres model which the damage evolution function is linear. For each material according to Lemaitre's model three parameters has to be determined while Bonora's CDM model needs five different parameter in order to calibrate the model for each material. There are other different CDM models in the literature [25], [26], [27] which are basically similar to each other and mostly use the same concepts of Lemaitre's CDM model. The application area of the CDM models has been extended to various fields and it is not just limited to the ductile damage anymore. In some applications, the assumption of isotropic damage is not satisfactory, and a comprehensive model, which takes the effect of anisotropy in damage distribution into account, is needed. Chow et al[28] have developed an anisotropic theory of continuum damage mechanics for ductile fracture. A new anisotropic damage evolution equation and a constitutive equation of plasticity have been formulated using a damage effect tensor proposed by authors. A generalized damage characteristic tensor which is compatible with damage effect tensor has been developed also to characterize anisotropic damage evolution. Lemaitre et al.[29] established a formulation for anisotropic damage in the framework of the principle strain equivalence. The damage variable is still related to the surface density of microcracks and microvoids and as its evolution is governed by plastic strain, it is represented by a second order tensor and is orthotropic. The coupling of damage with elasticity has been written through a tensor on a deviatoric part of the energy and through a scalar taken as its trace on the hydrostatic part. The kinetic law of damage evolution is an extension of the isotropic case. The princi-

pal components of the damage rate tensor are proportional to the absolute value of principal components of the plastic strain rate tensor and are a nonlinear function of the effective elastic strain energy. The proposed damage evolution law did not introduce any other material parameter. Voyoiadiss and Park[30] also proposed a fourth order damage tensor through the concept of the effective stress within the framework of continuum damage mechanics.

Damage closure effects and cyclic loading are further applications for CDM models. In case of presence of compressive loading it is necessary to apply some modifications to the general CDM models and in several papers this issue has been addressed. Yang et al.[31] studied the low cycle fatigue damage evolution by use of continuum damage mechanics theory. Based on thermodynamics, on a continuum damage variable and on the effective stress concept, a continuum damage model of isotropic low cycle fatigue has been derived and used to analyze the strain-controlled low cycle fatigue damage evolution of steam turbine blade material 2Cr13 steel. Pires et al.[32] extended a previous established model formulated by Perzyna[33] to include isotropic damage. Such an extension has been obtained by incorporating the constitutive equations introduced by Lemaitre[22] for ductile plastic damage into the original model. Proposed modification of Pires et al.[32] takes into account the partial crack closure effect with isotropic damage which in its original version Lemaitre's model did not distinguish tension and compression in the damage evolution law. Bonora and Pirondi[34] extended Bonora's previously proposed model[24] on the basis of a plausible physical description in order to account for the occurrence of repeated tension-compression overloads causing failure in the low cycle regime controlled by plastic strain. The modified damage model has been implemented into commercial finite element codes (MARC, ABAQUS) and tested on a single element and Round notch bar geometry to simulate material survivability under severe constant strain amplitude fatigue loading. Using the above mentioned extended model of Bonora and Pirondi[34] and the porous metal plasticity model of leblond, Perrin and Devaux[35], steglich et al.[36] has done a numerical investigation on the possibility to simulate and predict cyclic plastic response incorporating damage. To this purpose, unit cell and continuum approaches based on porous metal plasticity and continuum damage mechanics have been considered.

Some CDM models for the prediction of creep behavior of materials have been proposed also. Bhattacharya et al.[37] assuming that damage occurs isotropically

under uniaxial loading, obtained closed form solutions for ductile damage as a function of plastic strain, for creep damage as a function of time and for fatigue damage as function of number of cycles. Jing et al.[38] proposed a nonlinear continuum damage mechanics model to assess the creep-fatigue life of a steam turbine rotor, in which effects of complex multiaxial stress and coupling of fatigue and creep have been taken into account. The nonlinear evolution of damage has been also considered. The model has been applied to a 600 MW steam turbine under a practical start-stop operation. Hayhurst et al.[39] developed constitutive equations for 316 stainless steel at 550 C. Firstly time independent plastic straining at high temperature has been considered and secondly, mechanisms-based creep constitutive equations has been described and have been formulated. Constitutive equations for time dependent creep based on the theory of CDM mechanics has been developed. Hayhurst et al[39] discussed how the time independent and time dependent models may combined in a finite element analysis code to predict inelastic straining due to initial loading and to stress redistribution encountered in inherent cracking of welded pressure vessels.

Damage models are generally related to the micromechanic. Therefore, model parameters only depends on material and damage models are theoretically supposed to be independent from the geometry and loading conditions. This is an interesting advantage in comparison with other frameworks like fracture mechanics. However, practically geometry may affect the results of the damage models. It is common to calibrate a model in a specific loading condition and geometry and then apply such calibration to other scenarios. This approach may lead in some circumstances even to relevant errors. In order to avoid such unwanted drawback, damage models should be investigated for wide loading conditions. Each model can produce perfect results for some cases and at the same time may fail to have an acceptable predictions for a different loading condition. A correct calibration of the damage model parameters plays a significant role in the accuracy of the results. Some studies have been done in order to investigate different damage models in the different loading conditions during the last years.

Choung et al.[40] has done some experiments on the API-2W50 and DNV-DH32TM steel smooth and notched round and flat specimens. From incremental tensile tests for smooth specimens, average true stress-logarithmic true strain curves have been obtained and by using Bridgmans formula for round specimen and Choung's formula for flat specimens, average true stress has been rectified. Tensile tests for

notched specimens with various notch radiuses have been carried out and damage tests have been performed to identify material parameters of damage mechanics model. Shear fracture model, Lemaitre's CDM model and Gurson's model have been investigated by comparison of these models predictions with the experimental results.

Another study has been done by Coppola et al.[41] Tensile, torsion, flattening and bending tests have been carried out covering a wide range of stress triaxiality and Lode angle. This study has been done to investigate the effect of the Lode angle on the fracture locus. Numerical simulations of each test have been set up to provide additional information whenever direct measures could not be feasible. Three steel grades for cold working applications, each characterized by two different heat treatments have been investigated in the experimental campaign. The results stated that fracture limits in the failure strain-triaxiality plane can be confined between two boundary curves, characterized by the values 0 and 1 for the lode angle. The paper proposed that this evidence is a consequence of the application of Tresca criterion for shear failure. It has been furthermore theoretically derived and experimentally verified that two limits are linked together through the material hardening behavior. It has been also discussed that an asymmetry between tension and compression states could exist as a consequence of the proposed approach.

Wierzbicki et al.[42] and Bao et al.[8] have done a comprehensive study on the 2024-T351 aluminum alloy. Upsetting and tensile tests have been done on various specimen geometries and different phenomenological models have been investigated comparing the results with the experimental data. Seven criteria including constant equivalent strain criterion[43], the Xue-Wierzbicki fracture criterion[44], [45] the Wilkins[46], Johnson Cook[1] and the Crach FEM fracture models have been calibrated and evaluated. Additionally, the maximum shear stress model and fracture forming limit diagram[47] have been evaluated in this paper. All criteria have been formulated in the general 3-D case for the power low hardening materials and one-to-one mapping from plane stress condition. Among the investigated models, old maximum stress failure criterion had the best results. This criteria not only followed the trend of experimental points with engineering type accuracy but requires only one test for calibration which make it easy to apply also. However maximum shear stress model could not predict the failure in the axisymmetric loading condition. The Xue-Wierzbicki fracture criterion could predict fracture in

all types of experiments with superior accuracy. However it requires four different tests for calibration. The Wilkins criterion recognizes the importance of both hydrostatic and deviatoric states on fracture. Good predictions has been obtained either in the range of large or small stress triaxiality but not in both. It has been shown also that Jhonson-Cook, the fracture forming limit diagram approach and the constant equivalent strain method can only be used in a situation when stress triaxiality and or the lode angle vary in vary narrow ranges which are known ahead of time.

Geometry transferability of the Bonora's CDM model[24] in occurrence of ductile damage under different stress triaxiality conditions in ferritic steels have been investigated by Bonora et al[48]. Geometry transferability of the model parameters have been investigated both in the low and high triaxiality region. It has been shown that Bonora's CDM model allows good prediction of the failure for tensile test on round notch specimen. In the high triaxiality region which has been investigated by means of properly cracked specimens, very good agreement between the experimental and numerical data has been shown also. It has been demonstrated that, in the numerical simulation, providing the material plastic flow curve accurately determined for the post-necking regime, the specimen or component, global and local response features can be correctly predicted without the need to invoke the influence of other effects, such as damage softening; while damage modeling is necessary to predict time and location of the occurrence of failure, to simulate ductile failure processes and associated material stiffness. The geometry transferability of the damage model parameters has been demonstrated firstly on round notched bar configuration. It has been shown that the proposed damage model allows to predict and understand correctly the failure locus in the stress triaxiality vs strain space, not only for the proportional loading case but also for variable load paths. In addition, the numerical simulations, performed with the damage model, found confirmation not only in the very good agreement of the geometry structural responses with the experimental data, but also with the damage maps observed in sectioned samples at different load levels. Similar very good agreement has been found for high stress triaxiality range which has been tested in cracked geometries and again the geometry transferability of model parameters has been demonstrated as well as the possibility to predict geometry constraint on material resistance to ductile crack advance.

The most comprehensive study about the application of different ductile damage

criterion in very different scenarios, probably has been done by Li et al.[49]. In this study, several criteria under the categories of uncoupled damage criterion and the coupled damage criterion, including the continuum damage mechanics model of Lemaitre and Gurson-Tveergaard-Needleman model, have been investigated to determine their reliability in ductile failure prediction. To create diverse stress and strain states and fracture modes, different deformation scenarios have been generated using tensile and compression tests of Al-alloy 6061 with different sample geometries and dimensions. The experimental and numerical simulation have showed that a decrease in stress triaxiality reduces the accuracy of ductile fracture prediction for both categories of ductile fracture criteria due to the interplay between principal stress dominant and shear-stress dominant fracture. For deformations with higher triaxiality value, both coupled and uncoupled damage model categories were able to predict the failure location reasonably well. For deformation with a lower or even negative triaxiality value, The Gurson-tveergaard-Needleman and Lemaitres model, as well as some of the uncoupled criteria, including Cockroft and Lotham[4], Ayada[5] and Oyan models[7], provided relatively reasonable predictions. Only Tresca and Freudenthal models[50] can properly predict shear dominant fracture. The reliability sequence in terms of time to fracture and fracture moment prediction was the Gurson-Tveergaard-Needleman, Lemaitre's model and then uncoupled models.

In spite of the researches above mentioned more studies are still needed to investigate the geometry transferability of damage models especially Lemaitre's continuum damage mechanics model which is the mostly used and important CDM model. Therefore, in this paper Lemaitres model have been investigated. Particular attention have been devoted to highlight the critical aspects of the model and to remark advantages and disadvantages of application of the model in the different stress states. A comprehensive experimental test program has been carried out on various specimen geometries and under different loading conditions in order to cover wide range of stress triaxiality and lode angle which are the two main parameters represent the stress state inside the component. Experimental tests include four different series of experiments:

1. Multiaxial torsion+tension tests which has been carried out on the round specimen which covers the loading conditions for the zero and low triax-

iality values. These series of tests includes also one uniaxial tensile test performed on the specimen similar to the specimen of the torsion test however with a notch and one uniaxail tensile test on the flat smooth specimen.

2. Uniaxial tensile test of the flat specimens with five different geometries which leads to different failure mechanism varies from the shear dominant to tension dominant fracture.

3. Uniaxial tensile test of the round smooth and notched specimens with different notch radiuses.

4. Three point bending test of the notched specimen as a further application for the model.

Lemaitre's CDM model and plasticity constitutive law has been calibrated first for the test material which is Ti-6Al-4V titanium alloy using the uniaxial tensile test of the round smooth specimen and the parameters of the model has been obtained for Ti-6Al-4V titanium alloy. All of the experimental tests has been reproduced using the finite element models and implementing the calibrated model into the finite element models. The experimental results have been compared with the predictions of the damage models obtained from the finite element models. Load-displacement/torque-rotation data and also failure displacement has been obtained from the experimental tests and the results has been compared with the numerical predictions. Analyzing the scanning electron microscope images of the failure surface and also stress state analysis of the specimens during the loading proves the existence of the different failure mechanism in the experiments which satisfies the aim of covering a wide range of loading condition and investigating of the model in the different conditions. Advantages and limitations of the model have been properly investigated and critical points and possible errors of the application of the model for each experiment has been discussed. The choice of Ti-6Al-4V titanium alloy is due to its importance and large application in the industry specially in the aerospace structures which comes from high strength and low density of Ti-6Al-4V titanium alloy. Nevertheless, its importance and wide usage, Ti-6Al-4V titanium alloy has not been studied in detail in the literature so far. There are few researches dealing with the application of the damage models in Ti-6Al-4V titanium alloy. Giglio et al.[12], [13] have calibrated a damage model

based on the phenomenological damage model of Bao-Wierzbicki[9] for Ti-6Al-4V titanium alloy and applied a calibration of the damage model to investigate a real rotor hub of a helicopter. To assess the behavior of the component, a fatigue test until failure has been done by Giglio et al.[13] on real Ti-6Al-4V hub. Katani et al.[51] developed a simulation method to predict the effect of microstructural morphology in mechanical properties and failure mechanism of Ti-6Al-4V titanium alloy. Finite element models have been created based on a clarification of a damage mechanism to control the ductile cracking. Simulation of the dimple failure of the failure of the material, using Gurson-Tveergaard-Needleman model, has been presented also in Katani et al's.[51] article.

This thesis includes six chapters. Chapter two is about the theoretical background of the Lemaitre's continuum damage mechanics model. Definition of damage in continuum damage mechanics, derivation of the governing equations of the Lemaitre's CDM model and one of the mostly used algorithm proposed for the implementation of the Lemaitre's model in the numerical simulations has been discussed in chapter 2. Chapter 3 gives detailed information about all of the experimental tests has been carried out. Different geometries of the specimens, loading conditions and test set up can be found in this chapter. Numerical simulations and procedure of making the finite element models has been discussed in chapter 4. Chapter 5 has been devoted to results and discussions. Information about the calibration of the model, comparison of the experimental and numerical results, error analysis of the predictions of the model are included in this chapter. Finally chapter 6 discusses about the conclusions and suggestions for the future researches in this field.

Chapter 2

Theoritical Background

All materials are composed of atoms, which are held together by bonds resulting from the interaction of electromagnetic fields. Elasticity is directly related to the relative movement of atoms. The physical study of the properties of an atomic lattice leads to the theory of elasticity, but much easier way is to write the mathematical constitutive equations directly at the mesoscale level using the property of reversibility of strain, which implies a one-to-one relationship, and eventually incorporate the properties of linearity and isotropy.

When debonding occurs, this is the beginning of the damage process. For example, metals are organized in crystals or grains: a regular array of atoms except on many lines of dislocations where atoms are missing. If a shear stress is applied, the dislocations may move by the displacement of bonds, thus creating a plastic strain by slip without any debonding.

If dislocation is stopped by a microdefect or microstress concentration, it creates a constrained zone in which another dislocation may be stopped. This second process cannot occur without a debonding damage. Several arrests of dislocations nucleate a microcrack. Other damage mechanisms in metal are intergranular debonding and decohesion between inclusions and the matrix. All these mechanisms create plastic microstrains.

- In polymers, damage occurs by breakage of bonds that exist between the long chains of molecules.

- In composites damage is the bonding between fibers and the polymeric matrix.

- In ceramics it is mainly microdecohesions between aggregates and the cement with the complex influence of water.

- In wood, the weak point where damage occurs is the bonding of the celulosic cells.

In all cases elasticity is directly influenced by the damage, since the number of atomic bonds responsible for elasticity decreases with damage. This coupling, which occurs at the level of the state of the material defined here by elastic strain and damage, is called a state coupling[52].

Plasticity is directly related to slips. In metals, slips occur by movement of dislocations or by the climbing of dislocations and twinning. In no case does it induce any appreciable volume change. In other materials, irreversible strains may occur by different mechanisms:

- Rearrangement of molecules in polymers;

- Microcracks in ceramics where the large lattice resistance does not allow movements of dislocations;

- Slips along surfaces of decohesions in concrete;

- Rearrangement of cells in wood.

They may induce a volume change.

In all cases, damage influences plastic or irreversible strains only because the elementary area of resistance decreases as the number of bonds decreases. The damage does not directly influence the mechanism of slip itself; that is, there is no state coupling. The indirect coupling owing to an increase in the effective stress arises only in the kinetic constitutive equation, it is called kinetic coupling.

- Elasticity takes place at the level of atoms.

- Plasticity is governed by slips at the level of crystals or molecules.

- Damage is debonding from the level of atoms to the mesoscale level for crack initiation.

Continuum mechanics deals with quantities defined at a mathematical point. From the physical point of view, these quantities represent averages on a certain volume. The Representative Volume Element(RVE), must be small enough to avoid smoothing of high gradients but large enough to represent an average of microprocesses. For experimental purposes and numerical analysis it is useful to consider the following orders of magnitude of representative volume element which is the scale of mesomechanics[52]:

- metals and ceramics: $0.1mm^3$

- polymers and most composites: $1mm^3$

- wood: $10mm^3$

- concrete: $100mm^3$

Another important property to consider is that the damage is always much more localized than the strain. Remember that the damage, or debonding of atoms, is restricted to a surface, although the strains, being movements of atoms by variation of their distance or by many slips, occur throughout the volume. If damage exists in a single plane at the mesoscale, there is no way to study it by classical continuum mechanics. Fortunately, most often it exists on many planes at the microscale, but always with a high space gradient. Micromechanics helps a great deal in for modeling the damage behavior.

In conclusion:

- the microscale is the scale of the mechanisms used to consider strains and damage;

- the mesoscale is the scale at which the constitutive equations for mechanics analysis are written;

- the macroscale is the scale of engineering structures.

2.1 Different manifestations of damage

Even if damage at the microscale is governed by one general mechanism of debonding, at the mesoscale it can manifest itself in various ways depending upon the

nature of the materials, the type of loading and the temperature.

Brittle damage

The damage is called brittle when a crack is initiated at the mesoscale without a large amount of plastic strain. Just to give an order of magnitude, let us say that the ratio of plastic strain to elastic strain is below unity: $\frac{\varepsilon_p}{\varepsilon_e} < 1$

This means that the cleavage forces are below the forces that could produce slips but higher than the debonding forces. The degree of localization is high.

Ductile damage

On the other hand, the damage is called ductile when it occurs simultaneously with plastic deformations larger than a certain threshold p_D. It results from the nucleation of cavities due to decohesions between inclusions and the matrix followed by their growth and their coalescence through the phenomenon of plastic instability. As a consequence, the degree of localization of ductile damage is comparable to that of plastic strain.

Creep Damage

When a metal is loaded at elevated temperature, for instance a temperature above 1/3 of the melting temperature, the plastic strain involves viscosity; that is, the material may be deformed at constant stress. When the strain is large enough, there are intergranular decohesions which produce damage and an increase of the strain rate through the period of tertiary creep. As for ductile damage, the gradients of creep damage are similar to the visco-plastic strain gradients.

Low cycle fatigue damage

When a material is subjected to cyclic loading at high values for stress or strain, damage develops together with cyclic plastic strain after a period of incubation preceding the phases of nucleation and propagation of microcracks. The degree of damage localization is higher than for ductile or creep damage. Because of the high values for stress, the low cycle fatigue is characterized by low values of the number of cycles to rupture, N_R:

$N_R < 10000$ cycles

If the material is strain loaded, the damage induces a drop of the stress amplitude for two stress-strain loops corresponding to the stabilized cycle and cycle to the rupture.

For metals, the damage can be either intergranular or transgranular microcracking following slip-ban arrests.

High Cycle fatigue

When a material is loaded with lower values for stress, the plastic strain at the mesolevel remains small and is often negligible. It may be high at some points at note that for brittle damage and high cycle fatigue damage, a stress-strain curve obtained from a classical tension-compression test at the meso-scale usually does not represent the true behavior for strain and damage because the space localization induces microplastic and damage zones much smaller than those of the specimens. Nevertheless, it is used because mechanical experiments at the microscale are difficult to perform; but the results are averages of nonuniform quantities over a mesovolume. The microhardness test may help to characterize a microvolume as it involves a size of order of microns but its state of stress is complex. The microlevel where transgranular microcracking occurs only on some planes and most often at the surface of the specimen by the mechanism of intrusion-extrusion. The number of cycles to failure may be very large[52]:

N_R>10000 cycles

As a consequence, the localization of damage is high.

2.2 Mechanical representation of damage

2.2.1 One dimensional surface damage variable(L.M.Kachanov)

It follows from the preceding section that damage may be interpreted at the microscale as the creation of micro surfaces of discontinuities: breaking of atomic bonds and plastic enlargement of microcavities. At the mesoscale, but number of broken bonds or the pattern of microcavities may be approximated in any plane by the area of intersections of all the flaws with that plane. In order to manipulate a dimensionless quantity, this area is scaled by the size of the representative volume element. This size is of primary importance in the definition of a variable continuous in the sense of continuum mechanics. At one point, it must be representative effect on failure of microdefects over the mesoscale volume element. It is similar to plasticity where the plastic strain ε_p represents, at one point, the average of many slips.

If a damaged body and a representative volume element (RVE) at a point M oriented by plane defined by its normal $\vec{n}$ and its abscissa x along the direction $\vec{n}$ as it has been shown in figure 2.1 is being considered where:

17
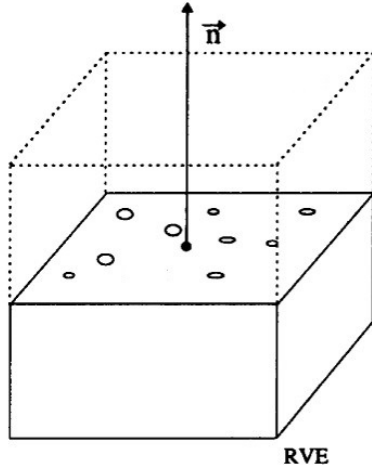
Figure 2.1: Physical definition of damage.

- δS is the area of intersection of the plane with RVE

- δS_{Dx} is the effective area of the intersections of all microcracks or micro-cavities which lie in δS;

The value of damage D(M, $\vec{n}$, x) attached to the point M in the direction $\vec{n}$ and at the abscissa x is:

$$D(M,\vec{n},x) = \frac{\delta S_D}{\delta S} \tag{2.1}$$

In order to define a continuous variable over the RVE for its deterioration to failure in two parts, one must look at all the planes varying with x and consider that which is most damaged:

$$D_{(}M,\vec{n}) = Max[D(M,\vec{n},x)] \tag{2.2}$$

The coordinate x disappears, and:

$$D_{(}M,\vec{n}) = \frac{\delta S_D}{\delta S} \tag{2.3}$$

18

It follows from this definition that the value of scalar variable D(which depends upon the point and the direction considered) is bounded by 0 and 1: $0 < D < 1$;

D=0 $\longmapsto$ undamaged RVE material;

D=1 $\longmapsto$ fully broken RVE material in two parts.

In fact, the failure occurs for $D < 1$ through a process of instability. Consideration of the simple one-dimensional case of a homogeneous damage leads to the simple definition of damage as the effective surface density of microdefects:

$$D = \frac{S_D}{S} \tag{2.4}$$

2.3 Effective stress concept

If the RVE is loaded by force $\vec{F} = \vec{n}F$, the usual uniaxial stress is:

$$\sigma = \frac{F}{S} \tag{2.5}$$

If all the defects are open in such a way that no microforces are acting on the surfaces of microcracks or microcavities represented by S_D, it is convenient to introduce an effective stress $\tilde{\sigma}$ related to the surface that effectively resists the load, namely (S-S_D):

$$\tilde{\sigma} = \frac{F}{S - S_D} \tag{2.6}$$

Introducing the damage variable $D = \frac{S_D}{S}$,

$$\tilde{\sigma} = \frac{F}{S(1 - \frac{S_D}{S})} \qquad or \qquad \tilde{\sigma} = \frac{\sigma}{1 - D} \tag{2.7}$$

This definition is the effective stress on the material in tension. In compression, if some defects close, the damage remaining unchanged, the surface that effectively resists the load is larger than S-S_D. In particular, if all the defects close, the effective stress in compression $\tilde{\sigma}$ is equal to the usual stress σ.

Coming back to the definition of the effective area of microcracks δS_D, effective has to be understood as strength, taking into account the microstress concentrations and mutual interactions of defects loaded in tension or shear. Only micromechanics may give a precise meaning of this concept which will be taken into account globally at the mesoscale through identification of the damage variable by means of its coupling with elasticity or plasticity.

2.4 Strain equivalence principle

A way to avoid a micromechanical analysis for each type of defect and each type of mechanism of damage is to postulate a principle at the mesoscale.

In thermodynamics, the method of local state assumes that the thermomechanical state at a point is completely defined by the time values of a set of continuous state variables depending upon the point considered. This postulate applied at the microscale imposes that the constitutive equations for the strain of microvolume element are not modified by neighboring microvolume element containing a microcrack. Extrapolating to the mesoscale, this means that the strain constitutive equations written for the surfaces δS-δS_D are not modified by the damage or that the true stress loading on the material is the effective stress $\tilde{\sigma}$ and no longer σ. The following principle results:

Any strain constitutive equation for damaged material may be derived in the same way as for a virgin material except that usual stress is replaced by the effective stress.

This statement is a principle because it has been demonstrated only in some particular cases of damage through homogenization techniques. It will be applied either to elasticity or plasticity.

2.5 Coupling between strains and damage

In accordance with description of the damage mechanics and direct application of the strain equivalence principle, one may write the uniaxial laws of elasticity and plasticity of damaged material.

2.5.1 Elasticity law

This direct state coupling through the concept of effective stress:

Undamaged material   Damaged material

D=0   0<D<1

$\varepsilon_e = \frac{\sigma}{E}$ $\varepsilon_e = \frac{\sigma}{E(1-D)}$

Contraction for isotropic damage:

$$\varepsilon_{22}^e = \varepsilon_{33}^e = -\nu\varepsilon_e \tag{2.8}$$

E is Youngs modulus of the undamaged material and ν is Poissons ratio.

The elasticity modulus of the damaged material defined by the ratio E=$\frac{\sigma}{\varepsilon_e}$ is:

$$\tilde{E} = E(1-D) \tag{2.9}$$

2.5.2 Plasticity

This is a kinetic coupling on the evolution of plastic strain which has to be written in the plasticity criterion used to derive the kinetic constitutive equations.

In order to model plasticity two kinds of strain hardening are usually considered:

- the isotropic hardening related to the density of dislocations or flow arrests;

- The kinematic hardening related to the state of internal microstress concentrations. The corresponding back stress defines the center of the elastic domain in tension compression(or in three dimensions).

If σ_y is the yield stress, R the stress due to isotropic hardening and X the back stress, both functions of the plastic strain, the one dimensional plasticity criterion defining the current threshold of yield limit is:

$$\sigma = \sigma_y + R + X \qquad or \qquad f = |\sigma - X| - R - \sigma_y = 0 \tag{2.10}$$

f is the yield function from which the kinetic constitutive equation for plastic strain is derived:

$\dot{\varepsilon}_p \neq 0$ if $f = 0$ and $\dot{f} = 0$

$\dot{\varepsilon}_p = 0$ if $f < 0$ or $\dot{f} < 0$

To achieve this, let us write the total strain as:

$$\varepsilon = \varepsilon_e + \varepsilon_p \qquad (2.11)$$

When damage occurs, according to the principle of equivalence, the yield function f must be written as:

$$f = |\frac{\sigma}{1-D} - X| - R - \sigma_y = 0 \qquad (2.12)$$

Experiments and equation:

$$\sigma = (\sigma_y + R + X)(1 - D) \qquad (2.13)$$

Show that the damage equally decreases the yield stress, the isotropic strain hardening stress and the back stress.

2.6 Lemaitres model

Taking the free-enrgy ψ thermodynamic potential, it is assumed that it is a function of all observable and internal variables. Using the hypothesis that elasticity and plasticity behaviors are uncoupled gives:

$$\psi = \psi_e(\mathbf{e}^e, T, D) + \psi_p(T, p) \qquad (2.14)$$

In order to obtain linear elasticity coupled with damage by means of the effective stress, ψ_e must be quadratic in $\boldsymbol{e^e}$ and linear in $(1 - D)$. If $\mathbf{a}$ is the fourth order tensor of elasticity and ρ the density:

$$\psi_e = \frac{1}{2\rho}\mathbf{a} : \boldsymbol{\varepsilon}^e : \boldsymbol{\varepsilon}^e (1-D) \tag{2.15}$$

The damaged elasticity law is:

$$\boldsymbol{\sigma} = \rho\frac{\partial\psi_e}{\partial\varepsilon^e} = \mathbf{a} : \boldsymbol{\varepsilon}^e (1-D) \tag{2.16}$$

And the variable y associated with D, by the power dissipation $(-y\dot{D})$ in the phenomenon of damage, is defiend by:

$$y = \rho\frac{\partial\psi_e}{\partial D} = -\frac{1}{2}a : \boldsymbol{\varepsilon}^e : \boldsymbol{\varepsilon}^e \tag{2.17}$$

The density of elastic strain energy has being defined as:

$$d\mathbf{W}_e = \boldsymbol{\sigma} : d\boldsymbol{\varepsilon}^e \tag{2.18}$$

If we replace $d\boldsymbol{\varepsilon}^e$ by its value taken from the damage elasticity law written for $d\boldsymbol{\sigma} = 0$ at constant temperature it will be obtained that $-y$ is one half of variation of W_e due to an infinitesimal increase of damage at constant stress and temperature. This gives for $-y$ the name of damage strain energy release rate

$$-y = \frac{1}{2}\frac{dW_e}{dD})\sigma, T \tag{2.19}$$

The expression of y and W_e show that:

$$-y = \frac{W_e}{1-D} \tag{2.20}$$

W_e is calculated as the sum of shear strain energy and volume dilatation energy with the tensor of elasticity written in terms of Youngs modulus $\mathbf{E}$ and Poissons ratio ν, that is the following relations between elastic strain deviator $\boldsymbol{e}^e$ and stress deviator $\mathbf{S}$, the hydrostatic strain $\varepsilon_H^e = \frac{1}{3}tr(\boldsymbol{\varepsilon}^e)$ and hydrostatic stress $\sigma_H = \frac{1}{3}tr(\boldsymbol{\sigma})$:

$$\mathbf{e}^e = \frac{1+\nu}{E}\frac{\mathbf{S}}{1-D}, \qquad \varepsilon_H^e = \frac{1-2\nu}{E}\frac{\sigma_H}{1-D} \tag{2.21}$$

We obtain:

$$-y = \frac{1}{2}[\frac{1+\nu}{E}\frac{\mathbf{S}:\mathbf{S}}{(1-D)^2} + 3\frac{1-2\nu}{E}\frac{\sigma_H^2}{(1-D)^2}] \tag{2.22}$$

23

With the Von Mises equivalent stress for plasticity:

$$\sigma_{eq} = (\frac{3}{2}\mathbf{S} : \mathbf{S})^{1/2} \tag{2.23}$$

$$-y = \frac{\sigma_{eq}^2}{2E(1-D)^2}[\frac{2}{3}(1+\nu) + 3(1-2\nu)(\frac{\sigma_H}{\sigma_{eq}})^2] \tag{2.24}$$

This quantity can be calculated for an equivalent one dimensional case defined by its stress σ^*:

$$\sigma_{eq} = \sigma^*, \qquad \sigma_H = \frac{1}{3}\sigma^* \tag{2.25}$$

$$-y = \frac{\sigma^{*2}}{2E(1-D)^2} \tag{2.26}$$

y is the variable associated with D, it means that evolution of D is governed by values of y; by analogy with the Von Mises equivalent stress for plasticity, the quantity:

$$\sigma^* = \sigma_{eq}[\frac{2}{3}(1+\nu) + 3(1-2\nu)(\frac{\sigma_H}{\sigma_{eq}})^2]^1/2 \tag{2.27}$$

σ^* is called dame equivalent stress and can act as a criterion for damage just as σ_{eq} acts as a criterion for plasticity. $\sigma^*/(1-D)$ is the damage equivalent effective stress and:

$$-y = \frac{\tilde{\sigma}^{*2}}{2E} \tag{2.28}$$

σ^* is equal to the Von Mises equivalent stress multiplied by a factor function of the triaxiality σ_H/σ_{eq} which is very important for damage function as shown by many experimental and theoretical studies.

Within the hypothesis of coupling between intrinsic mechanical and thermal dissipations, the second law of thermodynamics imposes summation of mechanical dissipation being positive:

$$\boldsymbol{\sigma} : \dot{\boldsymbol{\varepsilon}}^p - R\dot{p} - y\dot{D} \geq 0 \tag{2.29}$$

Due to the fact that processes of plasticity and damage may be independent, we must have separately:

$$\boldsymbol{\sigma} : \dot{\boldsymbol{\varepsilon}}^p - R\dot{p} \geq 0, \qquad -y\dot{D} \geq 0 \tag{2.30}$$

$-y$ being positive $\dot{D}$ must be positive which is trivial result. $(-y\dot{D})$ is the energy dissipated within the damage process for decohesion of material.

In order to derive constitutive equations for evaluation of dissipative variables, the existence of a potential of dissipation is assumed: a scalar convex function of flux variables ($\dot{\boldsymbol{\varepsilon}}^p, \dot{p}, \dot{D}$ and the heat flux $\mathbf{q}$) the state variables acting as parameters:

$\varphi(\dot{\boldsymbol{\varepsilon}}^p, \dot{p}, \dot{D}, \mathbf{q}; \boldsymbol{\varepsilon}^e, T, p, D)$

Other equivalent potentials can be obtained by means of the Legendre-Fenchel transform, in particular the partial transform changing $\dot{D}$ to its dual variable y:

$\varphi^*(\dot{\boldsymbol{\varepsilon}}^p, \dot{p}, y, \mathbf{q}; \boldsymbol{\varepsilon}^e, T, p, D)$

The constitutive equation for damage evolution D is given by the normality property of that potential:

$$\dot{D} = \frac{\partial \varphi^*}{\partial y} \tag{2.31}$$

Restricting ourselves to isotropic plasticity and isotropic damage, mathematical models are of a scalar nature. Ductile plastic damage, as plasticity, is a phenomenon which does not depend explicitly upon time.

Within these hypothesis the main features of ductile plastic damage can be described by potential of dissipation restricted to three variables:

$\varphi^*(y, \dot{p}, T)$

Written as a power function of y for convenience and linear in $\dot{p}$ to ensure the non explicit dependency of D with time:

$$\varphi^* = \frac{S_0}{(s_0 + 1)} \left(\frac{-y}{s_0}\right)^{s_0+1} \dot{p} \tag{2.32}$$

Where s_0 and S_0 are material and temperature dependent. The complementary law of evolution of damage derives from φ^* by:

$$\dot{D} = -\frac{\partial \varphi^*}{\partial y} = \left(\frac{-y}{S_0}\right)^{s_0+1} \dot{p} \tag{2.33}$$

Ductile plastic damage generally occurs with large deformations and in metal forming calculations. Large strain theory must then be used. Now:

- $\boldsymbol{\varepsilon}$ is the green Lagrange strain tensor,

- $\boldsymbol{\sigma}$ is the Cauchy stress tensor,

- $\boldsymbol{\varepsilon}^e$ is the elastic strain tensor defined with respect to the unstressed state.

Due to the large strain hypothesis the damage is written as function of total strain instead of plastic strain. Then:

$$\dot{p} = (\frac{2}{3}\boldsymbol{\varepsilon} : \boldsymbol{\varepsilon})^{1/2} \tag{2.34}$$

From the potential of dissipation:

$$D = (\frac{-y}{S_0})^{s_0}\dot{p} \tag{2.35}$$

In the expression for y:

$$-y = \frac{\sigma_{eq}^2}{2E(1-D)^2}[\frac{2}{3}(1+\nu) + 3(1-2\nu)(\frac{\sigma_H}{\sigma_{eq}})^2] \tag{2.36}$$

Replace σ_{eq} by its value, taken from the Romberg-Osgood hardening law coupled with damage and written for three dimensional case:

$$p = [\frac{\sigma_{eq}}{(1-D)K}]^M or \frac{\sigma_{eq}}{1-D} = Kp^{\frac{1}{M}} \tag{2.37}$$

Then:

$$\dot{D} = (\frac{K^2}{2ES_0}[\frac{2}{3}(1+\nu) + 3(1-2\nu)(\frac{\sigma_H}{\sigma_{eq}})^2]p^{\frac{2}{M}})^{s_0}\dot{p} \tag{2.38}$$

This is the governing equation for ductile damage evolution as derived in its original form by Lemaitre[22]. However, as it has been mentioned in chapter 1, Lemaitre's model has been extended for more general conditions. More details about the more general forms of the model can be found in[52] and [53]. As an example, following equations show set of equations which has to be solved for the isotropic hardening and more general constitutive low rather than Romberg- Osgood which has been considered in Lemaitre's original model[22]. The evolution of the stress tensor, $\boldsymbol{\sigma}$, plastic strain, $\boldsymbol{\varepsilon}^p$, and variables D and R is governed by the following set of elastoplasticity equations[54]:

$$\begin{aligned}
\dot{\boldsymbol{\varepsilon}}^e &= \dot{\boldsymbol{\varepsilon}} - \dot{\boldsymbol{\varepsilon}}^p \\
\dot{\boldsymbol{\varepsilon}}^p &= \dot{\gamma}\frac{\partial\phi}{\partial\boldsymbol{\sigma}} \\
\dot{R} &= \dot{\gamma} \\
\dot{D} &= \dot{\gamma}\frac{1}{1-D}(-Y)^s
\end{aligned} \tag{2.39}$$

Where the plastic multiplier $\dot{\gamma}$ is consistent with the classical loading/unloading conditions:

$$\dot{\gamma} \geq 0, \qquad \phi \leq 0, \qquad \dot{\gamma}\phi = 0 \tag{2.40}$$

In the above equations, *s* is experimentally determined material parameter associated to damage evolution and *Y* is the damage energy release rate defined as:

$$Y = \frac{-1}{2(1-D)^2}\boldsymbol{\sigma}:\mathbf{D}^{-1}:\boldsymbol{\sigma} = \frac{-q^2}{6G(1-D)^2} - \frac{p^2}{2K(1-D)^2} \tag{2.41}$$

2.7 Numerical Analysis of damage

Damage is essentially a nonlinear phenomenon often coupled with plasticity, also a nonlinear phenomenon. Therefore we can not expect simple closed-form solutions of mesocrack initiation problems except for rough approximations of simple cases.

For early design of mechanical components, the coupling of strain behavior with the damage may be neglected and a post-processing of damage evolution is possible after a classical structure analysis(D.Hayhurst and F.A.Leckie). This approach is the uncoupled analysis based on a reference plastic computation. For localized plasticity and damage, this reference computation can even be purely elastic with a local energetic correction to estimate the plastic strain fast.

For accurate engineering applications and when the coupling between strains and damage is strong, plasticity, damage, and possible cracks distributed over whole structure deem a fully coupled analysis necessary. The constitutive equations need to be implemented within a finite element computer code and the numerical analysis encounters the classical difficulties of convergence of linearized schemes. It needs special algorithms, much care, and large computer times.

When damage is localized on the mesoscale, there is the possibility to use the two scale damage model in which damage occurs on microscale only. This locally coupled analysis mainly applies to high cycle fatigue (fatigue in the elastic range), eventually with initial plastic strain and damage. The analysis can be performed by post-processing an elastic computation for elastic fatigue or plastic computation if the process of creation of non-trivial initial conditions has been modeled. Another area that requires numerical analysis is the precise identification of the

material parameters. Even if a fast, rough identification is possible using simple methods, an adjustment or updating of parameters from more complex tests or similar studies needs numerous iterations and robust optimization techniques.

In order to apply the Lemaitre CDM ductile damage model in the numerical simulations, the most general algorithm has been proposed by Doghri[55] which includes kinematic hardening for the plasticity.In order to apply Doghri[55] algorithm series of 14 equations has to be solved in the same time. E.A. de Souza Neto[54] simplified Doghri et al[55] algorithm for the isotropic hardening and reduced the number of equations which has to be solved to one non linear equation. In the following section E.A. de Souza Neto[54] method has been explained.

2.7.1   One equation algorithm for Lemaitre ductile damage model

In the finite element context, the numerical integration of elasto-plasticity constitutive equations is typically carried out by means of the so-called elastic predictor/return mapping schemes. Such methodologies are extensively described elsewhere[56].

Let us consider what happens to a typical Gauss point of the finite element mesh within a (pseudo-) time interval $[t_n, t_{n+1}]$. Having the values σ_n, ε_n^p, R_n and D_n at t_n and given a strain increment $\Delta\varepsilon$ corresponding to the interval$[t_n, tn + 1]$, the numerical integration algorithm should obtain the updated values at the end of interval,σ_{n+1}, ε_{n+1}, R_{n+1} and D_{n+1} in a manner consistent with the constitutive equations of the model.

The first step in the algorithm is the evaluation of the elastic trial state, where the increment is assumed purely elastic with no evolution of internal variables (internal variables frozen at t_n). Then , the elastic trial stress has to be calculated:

$$\boldsymbol{\sigma}^{trial} = (1 - D_n)\mathbf{D} : \boldsymbol{\varepsilon}^{etrial} \tag{2.42}$$

Or, equivalently, in terms of stress deviator and hydrostatic pressure:

$$\mathbf{S}^{trial} = (1 - D_n)2G\mathbf{e}^{etrial}, \qquad p^{trial} = (1 - D_n)K\upsilon^{etrial} \tag{2.43}$$

Where:

$$\boldsymbol{\varepsilon}^{etrial} = \boldsymbol{\varepsilon}_n^e + \Delta\boldsymbol{\varepsilon}, \quad \mathbf{e}^{etrial} = \mathbf{e}_n^e + \Delta\mathbf{e}, \quad \upsilon^{etrial} = \upsilon_n^e + \Delta\upsilon \tag{2.44}$$

The elastic trial value of the yield function is then evaluated as:

$$\Phi^{trial} := \tilde{q}^{trial} - \sigma_y(R_n) \tag{2.45}$$

Where we have defined the effective elastic trial Von Mises equivalent stress:

$$\tilde{q}^{trial} \equiv \frac{q^{trial}}{1 - D_n} = \frac{\sqrt{3J_2(\mathbf{S}^{trial})}}{1 - D_n} = \sqrt{\frac{3}{2}} \frac{||\mathbf{S}^{trial}||}{1 - D_n} \tag{2.46}$$

If $\Phi^{trial} \leq 0$ the process is indeed elastic within the interval and elastic trial state coincides with the updated state at t_{n+1}. Otherwise, we need to apply the return mapping procedure whose step-by-step derivation is described in the following. Straightforward specialization of standard return mapping procedures for the present constitutive law leads to the following set of discrete evolution equations:

$$
\begin{aligned}
\boldsymbol{\varepsilon}^e_{n+1} &= \boldsymbol{\varepsilon}^{etrial} - \Delta\gamma \sqrt{\frac{3}{2}} \frac{\mathbf{S}_{n+1}}{(1 - D_{n+1})||\mathbf{S}_{n+1}||} \\
R_{n+1} &= R_n + \Delta\gamma \\
D_{n+1} &= D_n + \frac{\Delta\gamma}{1 - D - n + 1} (\frac{-Y_{n+1}}{r})^s \\
\frac{q_{n+1}}{1 - D_{n+1}} &- \sigma_y(R_{n+1}) = 0
\end{aligned}
\tag{2.47}
$$

Which then needs to be solved for unknowns $\boldsymbol{\varepsilon}^e_{n+1}$, $\Delta\gamma$, R_{n+1} and D_{n+1}. The last of the above equations is the so-called consistency conditions that guarantees that the stress state at the end of plastic step lies on updated yield surface. As we shall see in what follows, analogously to what happens to the classical Von Mises model, the above system can be reduced by means of simple algebraic substitutions to a single non-linear equation for the incremental plastic multiplier $\Delta\gamma$.

To start with, let us consider the deviatoric/volumetric split of equation 2.47. Since the flow vector that multiplies $\Delta\gamma$ on the right-hand side of equation 2.47 is deviatoric, we have:

$$\mathbf{e}^e_{n+1} = \mathbf{e}^{etrial} - \Delta\gamma \sqrt{\frac{3}{2}} \frac{\mathbf{S}_{n+1}}{(1 - D_{n+1})||\mathbf{S}_{n+1}||} \upsilon^e_{n+1} = \upsilon^{etrial} \tag{2.48}$$

Expression 2.48 together with the elastic law gives the following updating relation for the hydrostatic pressure:

$$p_{n+1} = (1 - D_{n+1})\tilde{p}_{n+1} \tag{2.49}$$

29

Where we have defined:

$$\tilde{p}_{n+1} = K\upsilon_{n+1}^e = K\upsilon^{etrial} \tag{2.50}$$

With the introduction of the elastic law into 2.48, It follows that:

$$\mathbf{S}_{n+1} = (1 - D_{n+1})2G\mathbf{e}_{n+1}^e = (1 - D_{n+1})2G\mathbf{e}^{etrial} - 2G\Delta\gamma\frac{3}{2}\frac{\mathbf{S}_{n+1}}{||\mathbf{S}_{n+1}||} \tag{2.51}$$

And we obtain the update equation for stress deviator:

$$\mathbf{S}_{n+1} = (1 - D_{n+1})\tilde{\mathbf{S}}_{n+1}^{trial} - 2G\Delta\gamma\sqrt{\frac{3}{2}}\frac{\mathbf{S}_{n+1}}{||\mathbf{S}_{n+1}||} \tag{2.52}$$

Where we have defiend:

$$\tilde{\mathbf{S}}^{trial} \equiv 2G\mathbf{e}^{etrial} \tag{2.53}$$

From 2.52 it is clear that $\tilde{\mathbf{S}}_{n+1}^{trial}$ is proportional to $\mathbf{S}_{n+1}$ so that we may equivalently write:

$$\mathbf{S}_{n+1} = (1 - D_{n+1})\tilde{\mathbf{S}}_{n+1}^{trial} - 2G\Delta\gamma\sqrt{\frac{3}{2}}\frac{\mathbf{S}_{n+1}}{||\mathbf{S}_{n+1}||} \tag{2.54}$$

After a trival re-arrangement, the above equation yields the following simpler update formula for $\mathbf{S}_{n+1}$:

$$\mathbf{S}_{n+1} = (1 - D_{n+1} - \frac{3G\Delta\gamma}{\tilde{q}^{trial}})\tilde{\mathbf{S}}_{n+1}^{trial} \tag{2.55}$$

From this last expression and definition of the Von Mises equivalent stress, we obtain:

$$q_{n+1} = (1 - D_{n+1})\tilde{q}^{trial} - 3G\Delta\gamma \tag{2.56}$$

By introducing 2.56 into 2.47 we obtain the consistency equation:

$$\tilde{\Phi}(\Delta\gamma, D_{n+1}) \equiv \tilde{q}^{trial} - \frac{3G\Delta\gamma}{1 - D_{n+1}} - \sigma_y(R_n + \Delta\gamma) = 0 \tag{2.57}$$

With 2.56 and 2.49 introduce into definition of the damage energy release rate, 2.47, can be written as:

$$D_{n+1} - D_n - \frac{\Delta\gamma}{1 - D_{n+1}}(\frac{-Y(\Delta\gamma, D_{n+1})}{r})^s = 0 \tag{2.58}$$

Where:

$$-Y(\Delta\gamma, D_{n+1}) \equiv \frac{\left[(1-D_{n+1})\tilde{q}^{trial} - 3G\Delta\gamma\right]^2}{6G(1-D_{n+1})^2} + \frac{\tilde{p}_{n+1}^2}{2K} \qquad (2.59)$$

In summary, the return mapping has been reduced to the set of two scalar equations comprising equations 2.57 and 2.58. The unknowns of this system of equations are $\Delta\gamma$ and D_{n+1}. After solution, with $\Delta\gamma$ and D_{n+1} at hand, $\mathbf{S}_{n+1}$ and p_{n+1} are trivially updated, respectively, by equations 2.55 and 2.50. This two-equation return mapping has been proposed by Vaz Jr[57] in the context of fracture prediction in metal cutting processes. A similar two-equation algorithm has been adopted by Steinmann et al.[57] for a variation of the simplified Lemaitre model, where damage energy release rate depends only on the deviatoric part of the strain energy function.

The above system can be further reduced leading to a computationally more efficient single-equation return mapping algorithm. Firstly, for convenience, we define the material integrity as:

$$\omega \equiv 1 - D \qquad (2.60)$$

With the above definition and equation 2.57 we may write:

$$\omega_{n+1} \equiv 1 - D_{n+1} = w(\Delta\gamma) \equiv \frac{3G\Delta\gamma}{\tilde{q}^{trial} - \sigma_y(R_n + \Delta\gamma)} \qquad (2.61)$$

In addition, by combining equations 2.57 and 2.59, the updated damage energy release rate may be expressed as a function of $\Delta\gamma$ only, i.e. we may re-define:

$$-Y(\Delta\gamma) \equiv \frac{[\sigma_y(R_n + \Delta\gamma)]^2}{6G} + \frac{\tilde{p}_{n+1}^2}{2K} \qquad (2.62)$$

Finally, by combining equations 2.61 and 2.62 with equation 2.61, return mapping procedure is reduced to the solution of the following scalar equation for $\Delta\gamma$:

$$F(\Delta\gamma) \equiv \omega(\Delta\gamma) - \omega_n + \frac{\Delta\gamma}{\omega(\Delta\gamma)}\left(\frac{-Y(\Delta\gamma)}{r}\right)^s = 0 \qquad (2.63)$$

Once a solution $\Delta\gamma$ has been found, hardening and damage variables has to be updated, the hydrostatic stress and stress deviator using the relevant equations listed above. The overall algorithm is conveniently listed in figure 2.2.

It should be noted that, in view of definition equation 2.61 , the left-hand side of
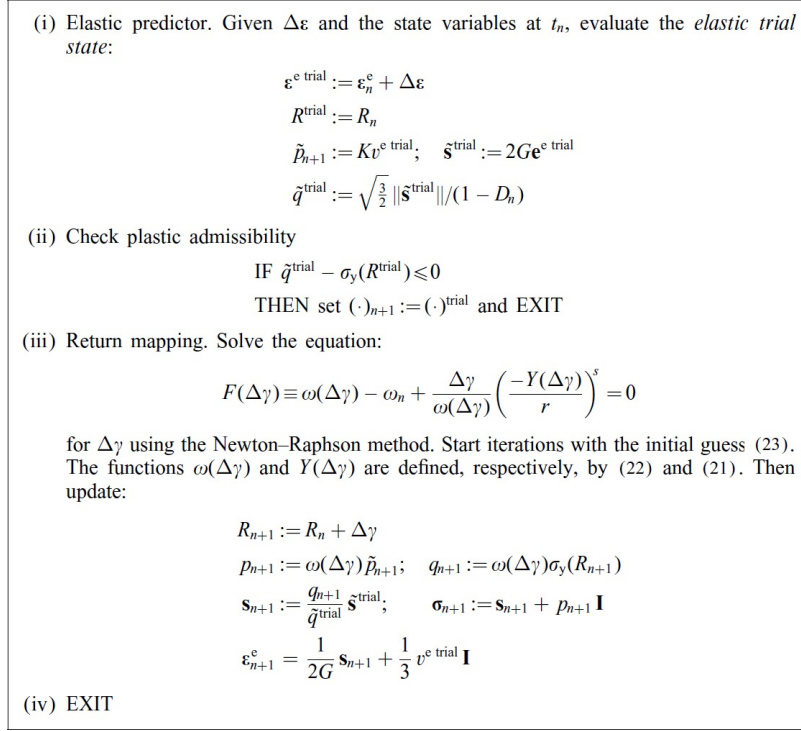
(i) Elastic predictor. Given $\Delta\varepsilon$ and the state variables at t_n, evaluate the *elastic trial state*:

$$\varepsilon^{\text{e trial}} := \varepsilon_n^{\text{e}} + \Delta\varepsilon$$

$$R^{\text{trial}} := R_n$$

$$\tilde{p}_{n+1} := K v^{\text{e trial}}; \quad \tilde{\mathbf{s}}^{\text{trial}} := 2G \mathbf{e}^{\text{e trial}}$$

$$\tilde{q}^{\text{trial}} := \sqrt{\tfrac{3}{2}} \, \|\tilde{\mathbf{s}}^{\text{trial}}\| / (1 - D_n)$$

(ii) Check plastic admissibility

$$\text{IF } \tilde{q}^{\text{trial}} - \sigma_{\text{y}}(R^{\text{trial}}) \leqslant 0$$

$$\text{THEN set } (\cdot)_{n+1} := (\cdot)^{\text{trial}} \text{ and EXIT}$$

(iii) Return mapping. Solve the equation:

$$F(\Delta\gamma) \equiv \omega(\Delta\gamma) - \omega_n + \frac{\Delta\gamma}{\omega(\Delta\gamma)} \left(\frac{-Y(\Delta\gamma)}{r} \right)^s = 0$$

for $\Delta\gamma$ using the Newton–Raphson method. Start iterations with the initial guess (23). The functions $\omega(\Delta\gamma)$ and $Y(\Delta\gamma)$ are defined, respectively, by (22) and (21). Then update:

$$R_{n+1} := R_n + \Delta\gamma$$

$$p_{n+1} := \omega(\Delta\gamma)\tilde{p}_{n+1}; \quad q_{n+1} := \omega(\Delta\gamma)\sigma_{\text{y}}(R_{n+1})$$

$$\mathbf{s}_{n+1} := \frac{q_{n+1}}{\tilde{q}^{\text{trial}}} \tilde{\mathbf{s}}^{\text{trial}}; \qquad \sigma_{n+1} := \mathbf{s}_{n+1} + p_{n+1} \mathbf{I}$$

$$\varepsilon_{n+1}^{\text{e}} = \frac{1}{2G} \mathbf{s}_{n+1} + \frac{1}{3} v^{\text{e trial}} \mathbf{I}$$

(iv) EXIT

Figure 2.2: One-equation elastic predictor/return mapping algorithm for simplified version of Lemaitre's damage model[54].

the return mapping equation 2.63 is singular at $\Delta\gamma = 0$. Thus, the initial guess $\Delta\gamma^{(0)} = 0$ usually adopted to start up the newton-Rophson iterations in classical return mappings, cannot be used in the present context. One possible alternative is to set:

$$\Delta\gamma^{(0)} = \frac{[\tilde{q}^{trial} - \sigma_{\text{y}}(r_n)]\omega_n}{3G} \tag{2.64}$$

Which corresponds to perfectly plastic solution for increment with frozen damaged yield surface at t_n. Numerical experiments have shown that an extremely stable algorithm results from use of the Newton-Raphson scheme with the above initial guess. The need for line searches does not appear necessary since convergence is attained for well-sized increments even at highly damaged states with D approaching unit.

Chapter 3

Experimental Tests

3.1   Introduction

Experimental results are most trustful data which can be used in a comprehensive research program. Experimental results can be used in order to validate and calibrate the analytical and numerical models. Before the application of any model it has to be validated and the accuracy of the predictions of the model has to be investigated in comparison with some other available reference data which in the most of the cases, these data has been obtained from experimental tests. Moreover, generally models have some parameters which has to be determined before the application based on some preknown data. Experimental data are also useful for this purpose. Once the calibration and validation of a model has been completed, experimental data can still be used as an investigator for the accuracy of the models predictions in other cases. Therefore, in this research, a comprehensive test program has been designed and carried out. A wide range of loading conditions and deformation modes has been investigated. Tests has been designed in a way that, different stress states which can be represented by stress triaxiality and Lode angle has been covered. Experiments include the stress triaxiality values starts from near zero until the high triaxiality regions(around 1). Value of stress triaxiality(η) and Lode angle(θ) is defined according to equations 3.1 and 3.2. The fracture phenomena is also different in the experiments which can be a good measure to check damage model under different failure mechanisms. Different specimen geometries including notched and smooth round/flat specimens under the uniaxial tensile, multiaxial torsion and three point bending loading has

been tested. Load-displacement/torque-rotation data has been extracted from the
experiments and has been used as the main data for the comparisons between nu-
merical models and experimental tests. Four different series of experiments has
been done which more detailed explanation about all of these experiments can be
found in the following sections. Test material is Ti-6Al-4V titanium alloy a widely
used material in the industry.

$$\eta = \frac{\sigma_H}{\sigma_{vm}} \tag{3.1}$$

$$\begin{aligned} \theta &= 1 - arccos\frac{\xi}{\pi} \\ \xi &= (\frac{r}{q})^3 \end{aligned} \tag{3.2}$$

3.2 Ti-6Al-4V titanium alloy

Ti-6AL-4V, also known as grade 5, is the most commonly used titanium alloy. It
is significantly stronger than commercially pure titanium while having the same
stiffness and thermal properties(excluding thermal conductivity which is about
60% lower in Ti-6Al-4V titanium alloy than commercially pure titanium). Among
its many advantages, it is heat treatable. This Ti Alloy is an excellent combina-
tion of strength, corrosion resistance, weld and fabric ability. This alloy is the
workhorse of the titanium industry. The alloy is fully heat treatable in section size
up to 15mm and is used up to approximately 400 C. Over 70% of all alloy grades
melted are a sub-grade of Ti-6Al-4V, its uses vary in many aerospace airframe
and engine components uses and also major non-aerospace applications in the
marine.[58]. Titanium alloys are generally classified into three main categories:
Alpha alloys, which contain neutral alloying elements (such as Sn) and/or alpha
stabilizers (such as Al, O) only and are not heat treatable; Alpha + beta alloys,
which generally contain a combination of alpha and beta stabilizers and are heat
treatable to various degrees; and Beta alloys, which are metastable and contain
sufficient beta stabilizers (such as Mo, V) to completely retain the beta phase upon
quenching, and can be solution treated and aged to achieve significant increases
in strength. Ti-6Al-4V offers a combination of high strength, light weight, forma-
bility and corrosion resistance which have made it a world standard in aerospace
applications. Ti-6Al-4V may be considered in any application where a combina-
tion of high strength at low to moderate temperatures, light weight and excellent

corrosion resistance are required. Some of the many applications where this alloy has been used include aircraft turbine engine components, aircraft structural components, aerospace fasteners, high-performance automotive parts, marine applications, medical devices, and sports equipment[59]. Chemical composition of the tested ti-6Al-4V titanium alloy has been showed in table 3.1.

Table 3.1: Chemical composition of Ti-6Al-4V titanium alloy[60].

Element	Ti	Al	V	N	H	Fe	O	C
Et.%	Bal.	6.38	4.17	0.01	0.001	0.15	0.16	0.01

Figure 3.1 shows the microstructure of the tested Ti-6Al-4V titanium alloy. This image has been taken from the etched surface of the material using an optical microscope. Krolls reagent (94 ml distilled water, 5ml nitric acid and 1ml hydrofluoric acid) was used for surface etching. The alpha+beta phases are clearly visible in Figure 3.1 and the average grain size is approximately 20m.
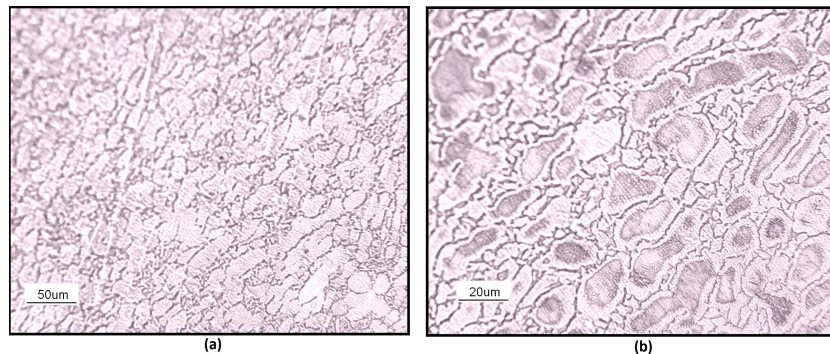
Figure 3.1: Microstructure of the tested Ti-6Al-4V titanium alloy (a) 200X. (b) 500X.

3.3 First series experimental tests: multiaxial torsion tests

This series of experiments includes multiaxial torsion tests carried out on the round specimens and tension test which has been performed on one round notched

and one smooth flat specimen.Three different type of specimen geometries have been tested which can be found by details in Table 3.2.

Table 3.2: torsion Test Specimens'Geometries

| Geometry A | Geometry B | Geometry C |
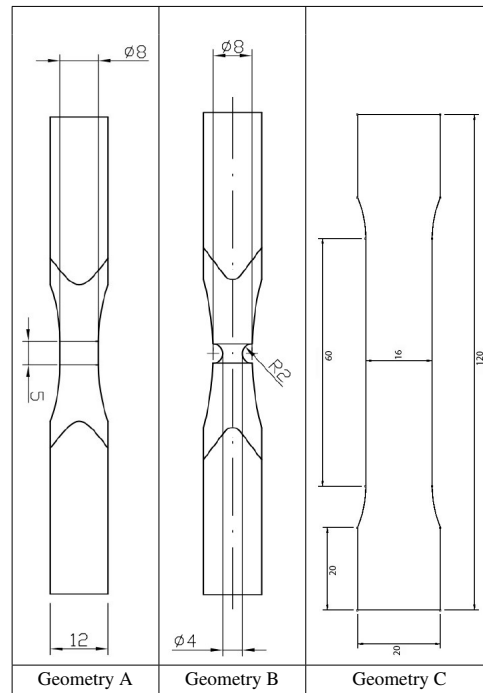
Specimen type A has been used for the multiaxial torsion tests. This type of specimen has been tested under the four different loading conditions which are a combination of torsion and different pre-tensile loads. Torque-rotation data has been obtained from the experiments. A multiaxial servo hydraulic MTS809 testing machine has been used to carry out the torsion tests and values of rotation and torque has been obtained from the load cell. Type B and C specimens has been tests under the uniaxial tensile load.Type A and B are round specimens while type C specimen is a flat specimen with 3mm thickness and rectangular cross section. For the uniaxial tensile tests an extensometer with the initial length of 12.5*mm* has been used to measure the displacement and a MTS alliance RF/150KN testing machine has been used to do the tension tests. Table 3.3 shows the explanation of the all loading conditions of the tests.

Figure 3.2shows the torsion test configuration and two specimens during test(Pure

Table 3.3: First series experiments characteristics

Test Type	Geometry	Axial Load(KN)
Pure torsion	A	0
Tension+torsion	A	20
Tension+torsion	A	30
Tension+torsion	A	40
Tension	B	-
Tension	C	

torsion and 30KN tensile+torsion). Figure 3.3 also shows some of the tested specimens after the tests.
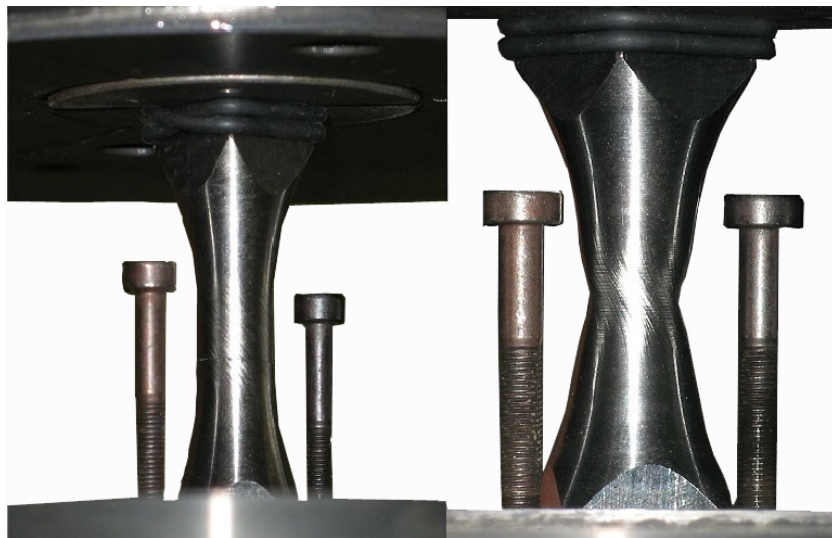
Figure 3.2: Torsion test configuration.

3.4 Second series experimental tests:Flat specimen

These serie of experiments include uniaxial monotonic tests which has been carried out on the flat specimens. These specimens has been designed in order to

Figure 3.3: Some of the first series specimens after failure.

Figure 3.4: Second series experiments set up.

create the plane stress condition in the tests. Different specimen geometries with different notch radiuses has been designed and manufactured to cover a wide range of stress state. Variation of the triaxiality from near zero to 0.6 is a good indicator for the different stress states in the specimens. Specimen geometries of these series of tests can be found in table 3.4 which includes four notched and one shear specimen. Tests are displacement control and has been done by a MTS alliance RT/100KN testing machine. An extensometer with initial length of 25mm for the notched specimens and 50mm for the shear specimen has been used to measure the displacement during the test. Figures 3.4 and 3.5 respectively shows test configuration for the specimen with hole and tested specimens after the failure.

3.5 Third series Experimental tests: Uniaxial tensile test on round notched specimens

Third series of the experiments includes the tests which has been don on the small round notched specimens. These tests has been done with collaboration of Universitta'degli studi di Cassino and research group of prof.Nicola Bonora. The tests are uniaxial displacement control tensile tests which have been carried out on the round specimens with different notch radiuses in order to have different stress

Table 3.4: Flat specimens'geometry
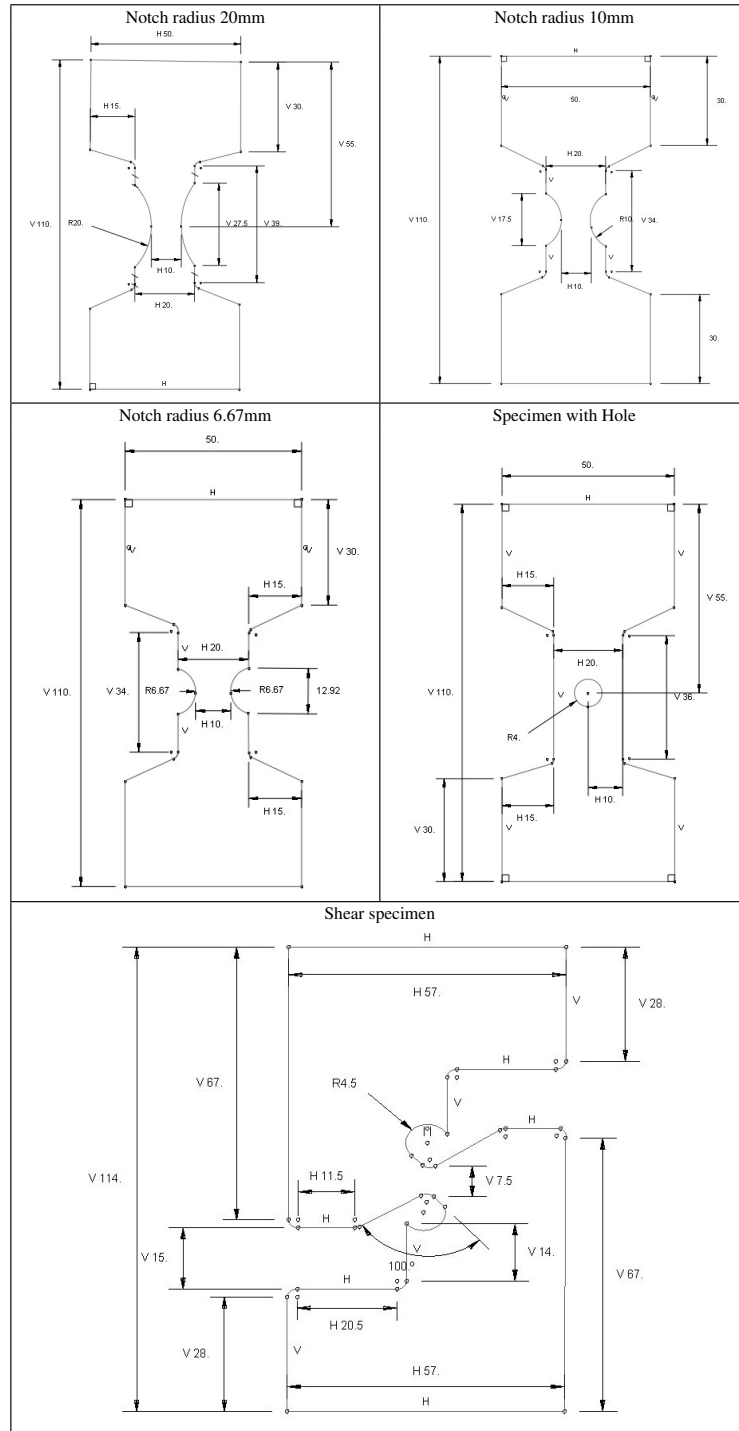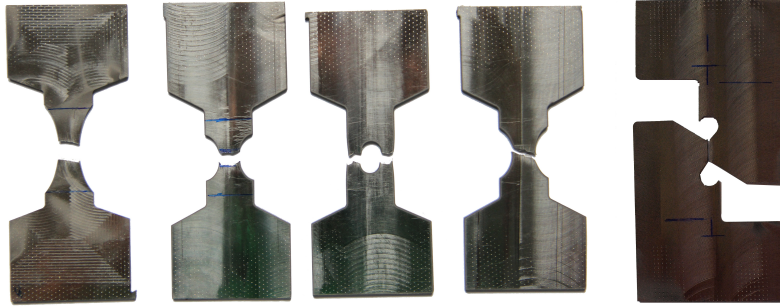
Figure 3.5: Flat specimens after the tests.

states. Round smooth specimens has been tested also. A more detailed information about the geometry of these series of specimens can be found in figure 3.6. Stress triaxiality value varies from around 0.35 in the smooth specimen to around 1.2 in the specimen with 1.5 notch radius. Similar to the other series of tests, an extensometer has been used to measure the displacement during the test, in this case the initial length of the extensometer is 12.5 mm. Failure diameter of the specimens has been measured also after the tests. Figure 3.7 shows some photos from the experiment during the test and measurement process.

3.6 Fourth series experimental test: Three point bending test

In order to have a test in the high triaxiality region and as a further application for the model, a three point bending test(TPBT) has been performed. The test has been done on the notch rectangular specimens. Due to the existence of the notch, extremely high stress concentration occurs in the notch tip which is a good test to investigate the model in the high stress triaxiality regions. Figure 3.8 shows the geometry of the tested specimens. The test has been carried out in monoaxial hydraulic testing machine. Load-displacement data measured from the displacement of the pusher has been obtained from the experiment. A laser sensor (MEL Mikroelektronik GMBH, M5L/20, range 20mm) has been used to measure the
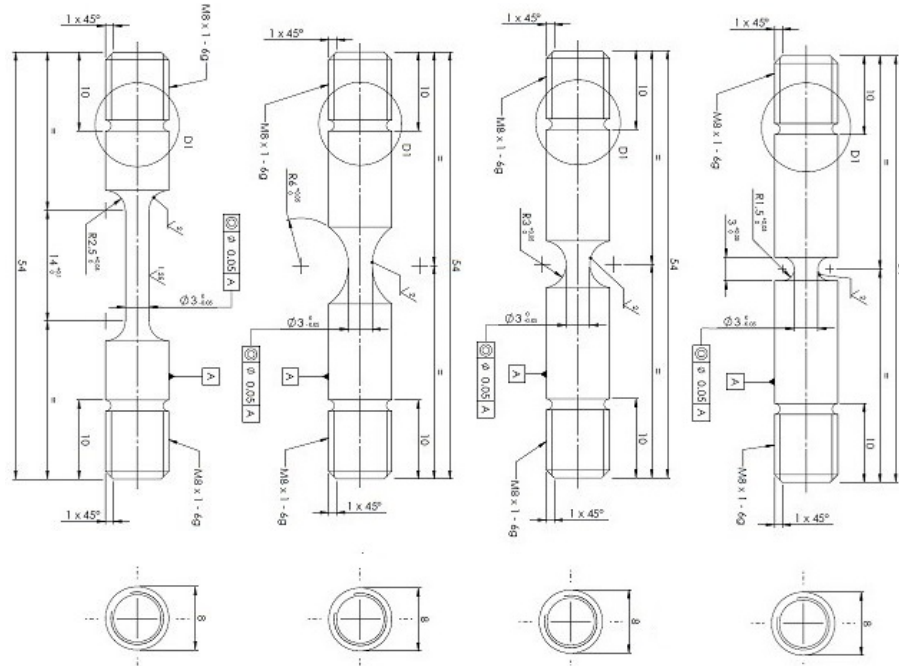
Figure 3.6: Specimen geometry of the third series of experiments.

displacement of the pusher.Figure 3.9 shows test set up of the experiment.

3.7 Summary of experiments

The main purpose of the experimental program was to cover a wide range of loading condition. Stress triaxiality and Lode angle are two important parameters which can be used as an indicator of the stress state. Experiments cover a wide range which is approximately from 0 to 1 for both of stress triaxiality and Lode angle. By performing all these experiments, a lot of experimental data with a wide variety has been obtained and being used to investigate damage model. Table 3.5 shows a summary of all experimental tests and related information about them.
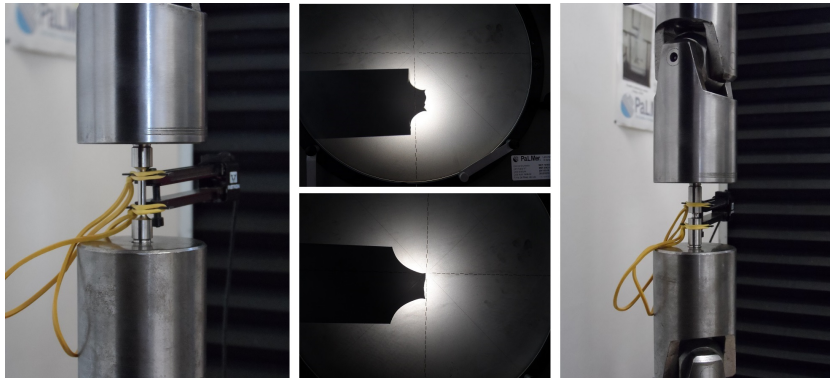
Figure 3.7: Test configuration and failure diameter measurement of the third series of experiments.
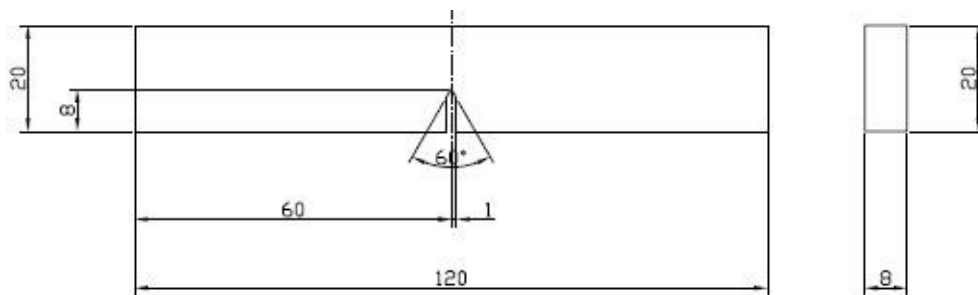
Figure 3.8: Three point bending test specimen's geometry.
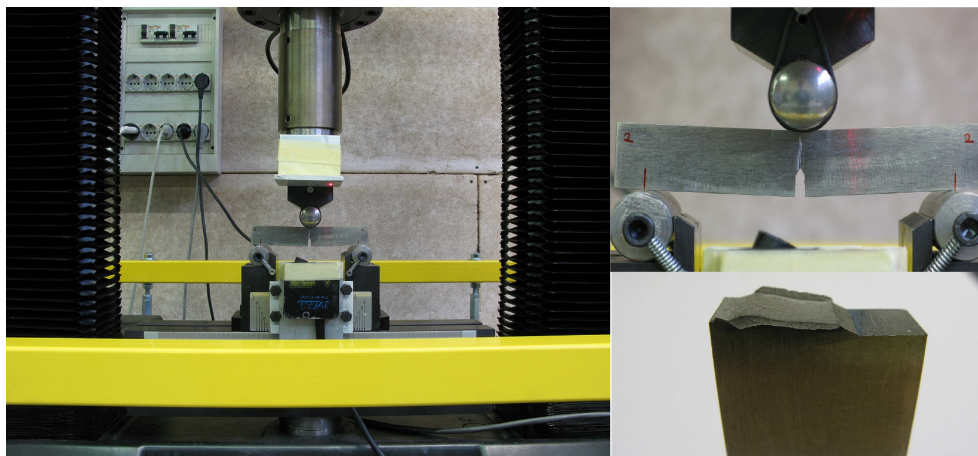
Figure 3.9: Three point bending test set up.

42

Table 3.5: Summary of experiments

Experiment series	Specimen type	Obtained experimental data
First series: Multiaxial torsion tests	A-Pure torsion(see tab.3.2)	Load cell torque-rotation
	A+20KN(see tab.3.2)	Load cell torque-rotation
	A+30KN(see tab.3.2)	Load cell torque-rotation
	A+40KN(see tab.3.2)	Load cell torque-rotation
	B(see tab.3.2)	Load-displacement-extensometer 25mm
	C(see tab.3.2)	Load-displacement-extensometer 25mm
Second Series: Uniaxial tensile test of flat specimens	Notch 20mm(see tab.3.4)	Load-displacement data-extensometer 25mm
	Notched radius 10mm(see tab.3.4)	Load-displacement data-extensometer 25mm
	Notched radius 6.67(see tab.3.4)mm	Load-displacement data-extensometer 25mm
	Specimen with hole(see tab.3.4)	Load-displacement data-extensometer 25mm
	Shear specimen(see tab.3.4)	Load-displacement data-extensometer 50mm
Third Series: Uniaxial tensile test of round specimens	Round smooth(see Fig.3.6)	(Load-displacement data-extensometer 12.5mm)+failure diameter
	Notch radius 6mm(see Fig.3.6)	(Load-displacement data-extensometer 12.5mm)+failure diameter
	Notch radius 3mm(see Fig.3.6)	(Load-displacement data-extensometer 12.5mm)+failure diameter
	Notch radius 1.5mm(see Fig.3.6)	(Load-displacement data-extensometer 12.5mm)+failure diameter
Fourth series:Three point bending test	Notched specimen(see Fig.3.8)	Load-diplacement(displacement of pusher) data

Chapter 4

Numerical Models

4.1   Introduction

Numerical models are a powerful tool in the research nowadays. Performing experimental tests are usually expensive and difficult. Numerical models, if properly build, can be a replace for the experiments. However, numerical models has to be used carefully and complete understanding of the models using inside the models and paying attention to the parameters which affect the FEM results are crucial. Despite the fact that numerical models are powerful and significantly useful they cannot totally replace the experiments and experimental tests are still an important part of research which cannot be ignored.

In this research in order to apply the CDM model, finite element simulation has been used. Finite element model(FEM) of all experiments has been build the experimental situation has been simulated. Abaqus, Ls-Dyna and Ls-opt softwares have been used to make the finite element analysis. More detailed information about the finite element(FE) models and simulation process can be found in the next sections.

4.2   Calibration of the plasticity constitutive low and damage model

First step in the application of the model is calibration and obtaining the model parameters. Plasticity Constitutive law and damage model has to be calibrated

before the application. Lemaitre's damage model has 3 parameters $(\varepsilon_{th}, S, D_{cr})$ which has to be calibrated for each material.

- ε_{th} threshold strain value which damage starts from.

- D_{cr} critical value of damage. Failure occurs when damage is equal to this value.

- S parameter related to the evolution of damage.

Inverse engineering try and error method has been used in this research in order to calibrate Lemaitres model. Smooth round specimen of the third series of experiments has been chosen as the calibration experiment. Damage model parameters has been obtained in a way that the FEM load-displacement data fit as much as possible to the experimental results. Finite element model of the smooth specimen has been made in ls-Dyna software. This model has been imported to ls-Opt which is an optimization software. Ls-opt had to solve the FEM model a lot of times in order to reach to the optimized solution. Therefore in order to decrease the running time, axisymmetric 2D model has been created. Load-displacement curve of the round smooth specimen has been given to the software as the target file. Possible range of the damage model and plasticity constitutive low parameters, has been indicated inside the model. Ls-opt using try and error and minimization of the mean square error between load-displacement data of the FEM and experiment, obtains needed parameters of the damage model and plasticity. Figure 4.1 shows the FE model. Software automatically changes the material model parameters in order to reduce the mean square error between the obtained and target curve. After the completion of the optimization process material model parameters which produce the best results have been determined. Best fitted curve to the experimental results for the round smooth specimen has been shown in figure 4.2. More detailed information about the optimization results can be found in section 5.1.
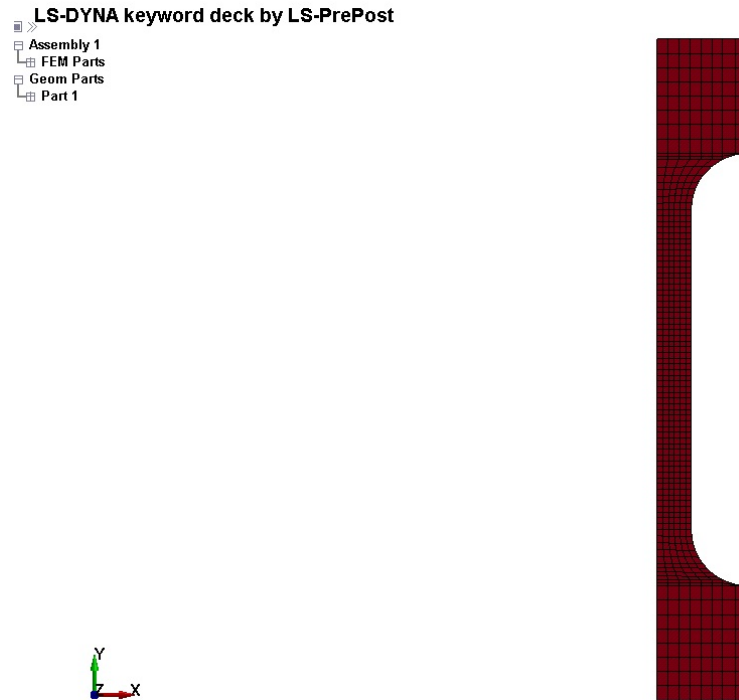
Figure 4.1: Axisymetric finite element model of the round smooth specimen.

4.3   Simulation of the experimental tests

4.3.1   First series:Multiaxial torsion tests

3D finite element model of the all specimens has been created. Reduced integrated cubic elements with the approximate size of the 0.1 mm in the critical region of the models, has been used. Loading conditions, according to the first series experimental situations has been simulated in the finite element model. Calibrated material model has been implemented inside the FE models. Figure 4.3 shows the finite element model of the all specimens of the first series tests.

4.3.2   Second series:Flat specimens

Three dimensional finite element models of all specimens have been created and due to symmetry a quarter of the specimens has been simulated in the notched and hole specimens. For the shear, whole specimen has been simulated however. The FE-model of the specimens has been implemented into the LS-DYNA software; cubic reduced integrated 8 node solid elements with the approximate size of 0.1
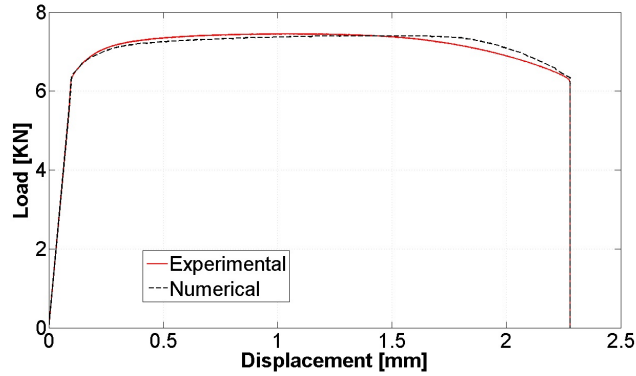
Figure 4.2: Best fitted load-displacement curve.
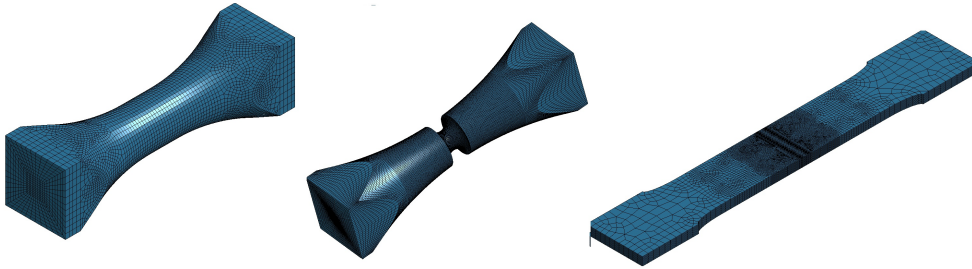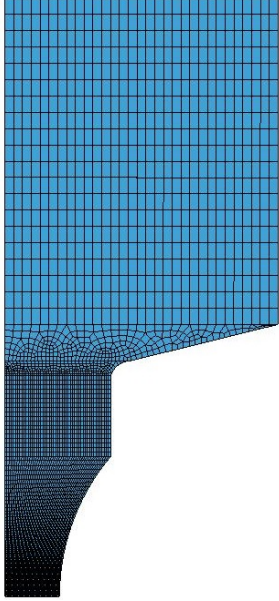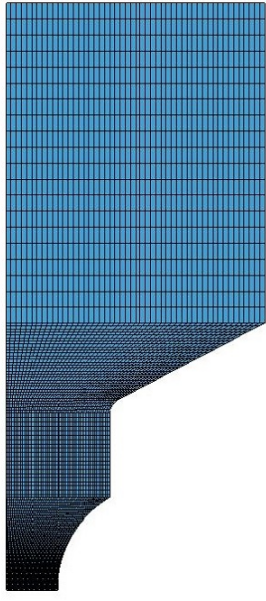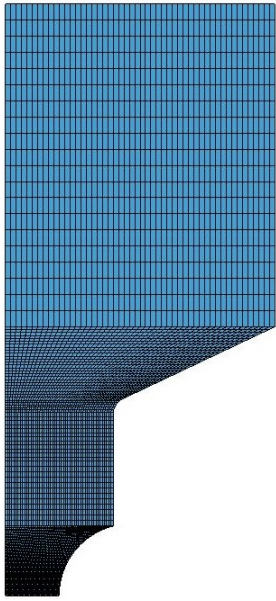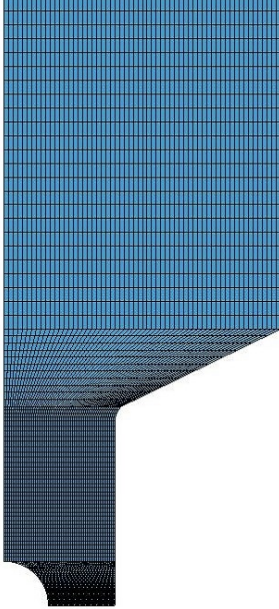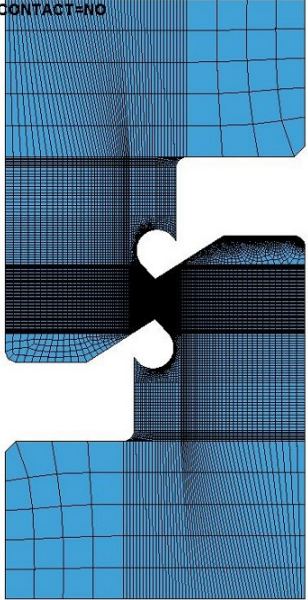
Figure 4.3: Finite element models of the first series experimental tests.

mm in the critical zone have been used. Table 4.1 shows the finite element models of the flat specimens.
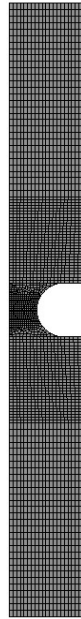
4.3.3 Third Series:Round notched specimens
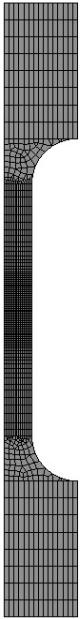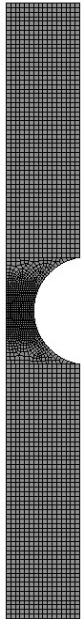
Experiments which has been done in the third series has been also simulated with finite element models. All specimen has been modeled both two and three dimensionally. 2*D* models have been created according to the existence of the asymmetry inside the models. Axisymmetric shell element with approximate length of 0.1mm in the notch region has been used in the 2*D* models. Material model without damage has been implemented to the 2D models and solved in ls-Dyna software. Table 4.2 shows 2D finite element models of the third series specimens. Three dimensional models has been simulated using 8 node solid reduced integrated elements with approximate size of 0.1 mm in the critical region. These models has been made both in ABAQUS and Ls-Dyna softwares. Material model

48

Table 4.1: Finite element model of the flat specimens.

Notch Radius 20mm	Notch Radius 10mm	Notch radius 6.67mm
Hole	Shear	

with damage have been implemented in Ls-Dyna. Table 4.3 shows the 3*D* FE models for the third series experimental tests.

Table 4.2: 2D Finite element model of the round notch specimens.

Smooth	Notch Radius 6mm	Notch Radius 3mm	Notch Radius 1.5mm

4.3.4   Fourth series:Three point bending test

A three dimensional finite element model of the specimen and the experimental test configuration has been made in Ls-Dyna commercial software. Reduced integrated cubic elements have been used in the simulations. Pusher and the supports has been simulated also and a contact surface has been defined between the specimen and the supports. In the presence of sharp notch, due to the sudden change of the stress field generally the numerical results of the FE simulations are very sensitive to the element size. Giglio et al.[12] has shown that for Ti-6Al-4V titanium alloy, the results of the finite element simulation using Bao-wierzbicki's damage model is so sensitive to the element size. In order to investigate the sensitivity of the CDM model to the mesh size three different mesh sizes with an approximate length of 0.2, 0.1 and 0.075 mm in the critical region around notch have been

Table 4.3: 3D Finite element model of the round notch specimens.

Smooth	Notch radius 6mm
Notch radius 3mm	Notch radius 1.5mm
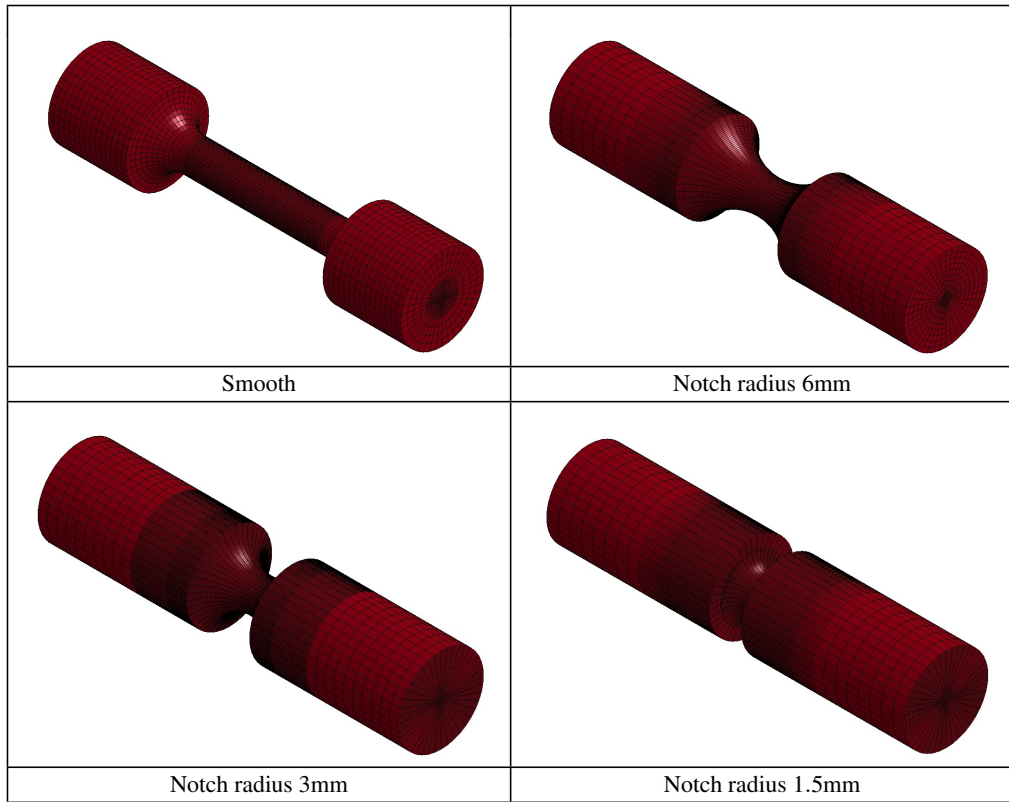
used in the FE models. Figure 4.4 shows the finite element model of the three point bending test. Calibrated damage model has been implemented inside the FE model.
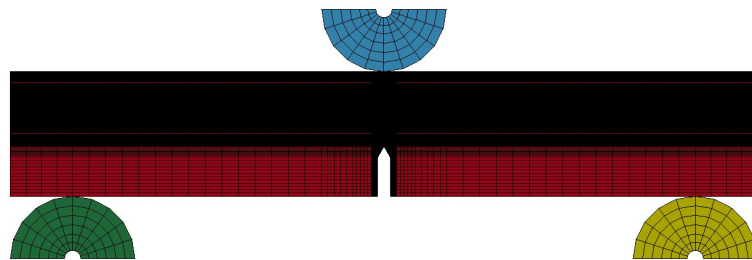

Figure 4.4: Finite element model of the TPBT configuration.

Chapter 5

Results and Discussion

5.1 Constitutive law and damage model calibration

Calibration of the constitutive law is fundamental in the finite element models. In this research three different plasticity models has been used inside the FEM models in order to simulate the behavior of Ti-6AL-4V titanium alloy. More detailed information about these plasticity models can be found in the following lines.

Giglio et al.[12] is calibrated a constitutive law for ti-6Al-4V titanium alloy according to the experimental results which has been obtained from the torsion specimens mentioned in section 3.3. Giglio et al.[12] have calibrated for each geometry and loading condition a specific plasticity model . Stress-strain curve can be divided into two different parts including before and after necking. Before necking, true stress and strain can be obtained from the engineering stress and strain. However, after necking due to the localization of the instabilities, value of the true stress and strain cannot be calculated directly from the experimental load-displacement data. Considering this fact, Giglio et al.[12] calibrated model is composed of two different parts responsible for before and after necking. First part of the model is in the form of the classical power law plasticity models with three parameters and is constant in all geometries and loading conditions. The second part of the constitutive law has been added in order to implement effect of the geometry and loading condition and is different in each test from the others. Equation 5.1 shows the general form of the plasticity model calibrated by Giglio et al[12].

$$\sigma = A + B\varepsilon_p^n \qquad\qquad \varepsilon_p \leq \varepsilon_{necking}$$
$$\sigma = A + B\varepsilon_p^n + C((\frac{\varepsilon_p}{\varepsilon_{necking}})^2 - 1) \qquad \varepsilon_p > \varepsilon_{necking} \tag{5.1}$$

Values of constants in equation 5.1 has been shown in table 5.1 for each geometry and loading condition.These parameters has been obtained by fitting the numerical load-displacement data to the equivalent experimental results for each case.

Table 5.1: Plasticity model parameters calibrated by Giglio et al[12].

Geometry	Load(KN)	A(MPa)	B(MPa)	n	$\varepsilon_{necking}$	C(MPa)
A	0	930	905.05	0.76	0.13525	-10
A	20	930	905.05	0.76	0.13525	-15.5
A	30	930	905.05	0.76	0.13525	-16.5
A	40	930	905.05	0.76	0.13525	-25
B	-	930	905.05	0.76	0.13525	-6

Despite the fact that above mentioned model properly simulate the behavior of the Ti-6AL-4V titanium alloy, the idea of using specific constitutive law for each test is not practical. Parameters of the model are specific for one test and by changing the loading condition they have to be changed. By considering this fact, an average of the plasticity models considered by Giglio et al[12] has been obtained and used as the second plasticity constitutive law in the FEM models. This plasticity model a classical power low with three parameters has been shown in equation(5.2):

$$\sigma(MPa) = 925.8 + 793.7\varepsilon_p^{0.6942} \tag{5.2}$$

Finally, general form of the last constitutive law, which has been used in all simulations and is the main model which is implemented inside the finite element models is shown in equation 5.3:

$$\sigma = \sigma_0 + Q_1(1 - exp(-C_1\varepsilon_p)) + Q_2(1 - exp(-C_2\varepsilon_p)) \tag{5.3}$$

As it can be seen in equation 5.3 this model has five parameters and has been obtained according to the experimental data obtained from smooth specimen of the third series experimental tests(more details about this experiment can be found in
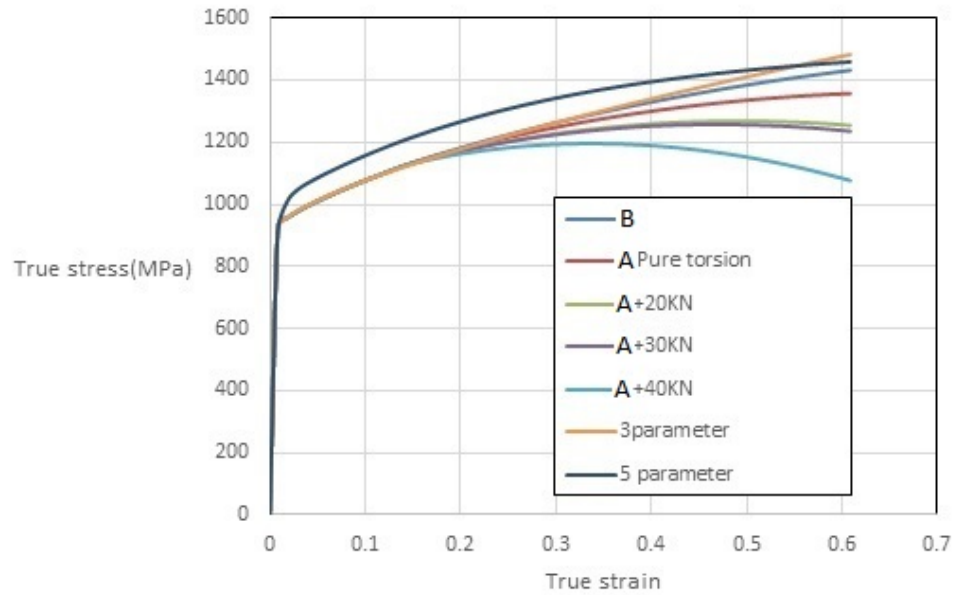
Figure 5.1: Different constitutive laws which has been used in the models.

section 3.5). The parameters of the model have been obtained in order to have the minimum difference between the load-displacement of the smooth specimen in the numerical and experimental results. Calibration has been done using an optimization software called ls-opt. Calibration of constitutive law has been done simultaneously with the calibration of the coupled damage model. Constitutive law mainly affects the load-displacement results before failure while damage model is mostly responsible for the failure moment. More information about the calibration process are available in section 4.2. Table 5.2 shows the model parameters obtained from the calibration.

5.2 Analysis of the experiments

5.2.1 First series experiments

Pure torsion

Above mentioned plasticity model with five parameters equation(5.3) have been implemented in the finite element model of the pure torsion test. Table5.2 shows the parameters of the plasticity flow rule and damage model which have been obtained from the calibration process explained in section 4.2. Figure 5.2 shows equivalent plastic strain(peeq) contour in the finite element model. Stress triaxiality, Lode angle and equivalent plastic strain values evolution during the test has been extracted from the finite element model. These values has been calculated in the critical element of the model which is the element with the greatest PEEQ value at the failure point. Figures 5.3 and 5.4 respectively show the PEEQ-triaxiality and PEEQ-Lode angle graphs for the pure torsion test. Average value of the triaxiality and Lode angle are important parameter which represent the stress state. These values can be calculated using equations 5.4 and 5.5. These average values have been calculated in the pure torsion test and the result can be found also in figures 5.3 and 5.4 . As it can be seen, the average value of the stress triaxiality is approximately zero which was predictable due to the dominance of the shear forces during the loading.

Figure 5.5 shows a comparison between the torque-rotation data obtained from the experiment and finite element model.

$$\eta_{avg} = \frac{1}{\varepsilon_f} \int_0^{\varepsilon_f} \eta d\varepsilon_f \qquad (5.4)$$

$$\theta_{avg} = \frac{1}{\varepsilon_f} \int_0^{\varepsilon_f} \theta d\varepsilon_f \qquad (5.5)$$

Table 5.2: Parameters of the calibrated model for plasticity and damage.

Plasticity					Damage		
$\sigma_{y_0}(MPa)$	$Q1(MPa)$	$C1$	$Q2(MPa)$	$C2(MPa)$	ε_{th}	$S(MPa)$	D_{cr}
912.712	499.715	3.627	103.215	146.212	0.2	25	0.1356
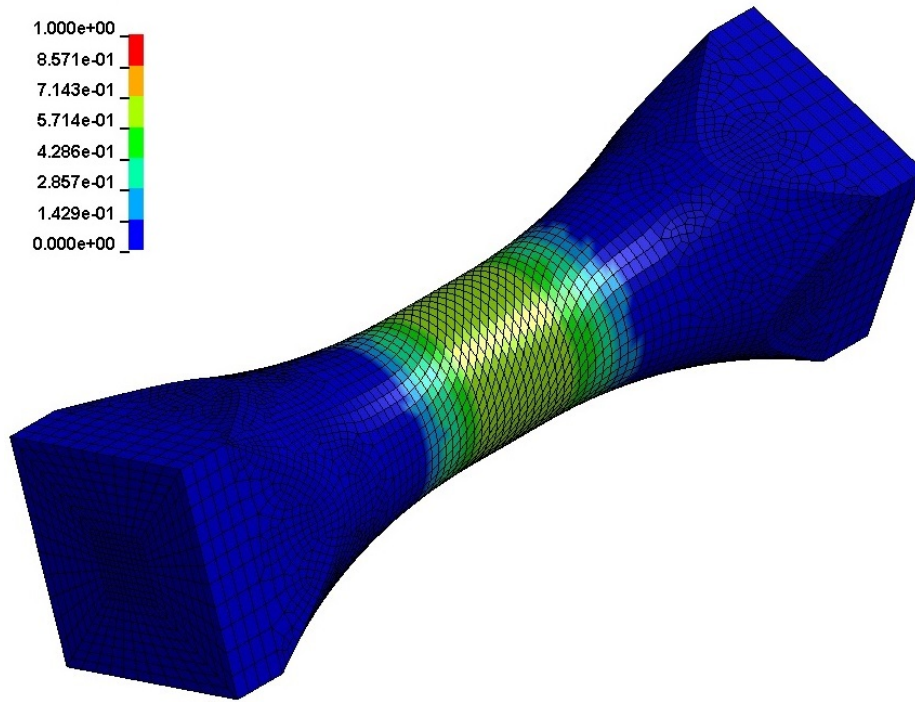
Figure 5.2: PEEQ contour at numerical failure point in the torsion test.
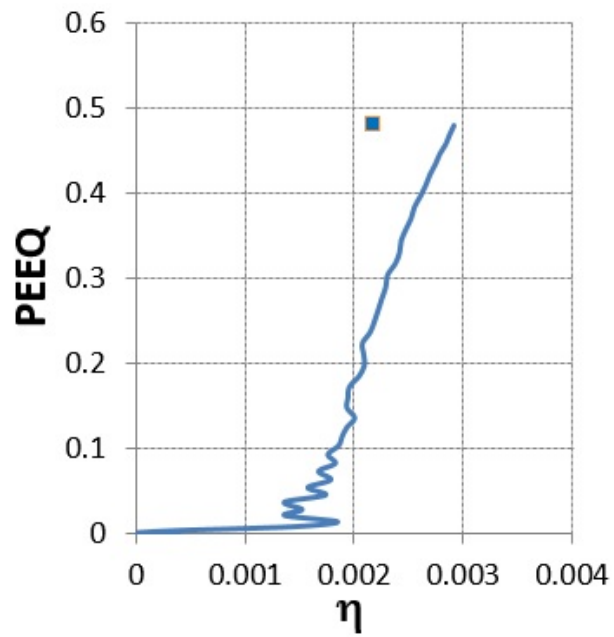
Figure 5.3: Triaxiality-PEEQ evolution curve in the pure torsion test.
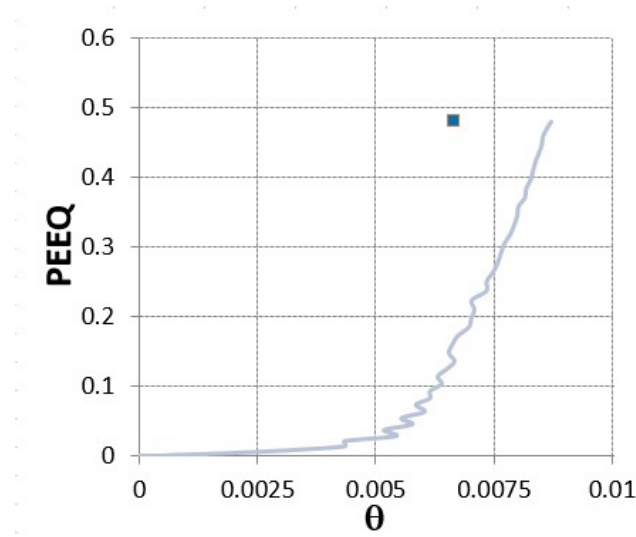
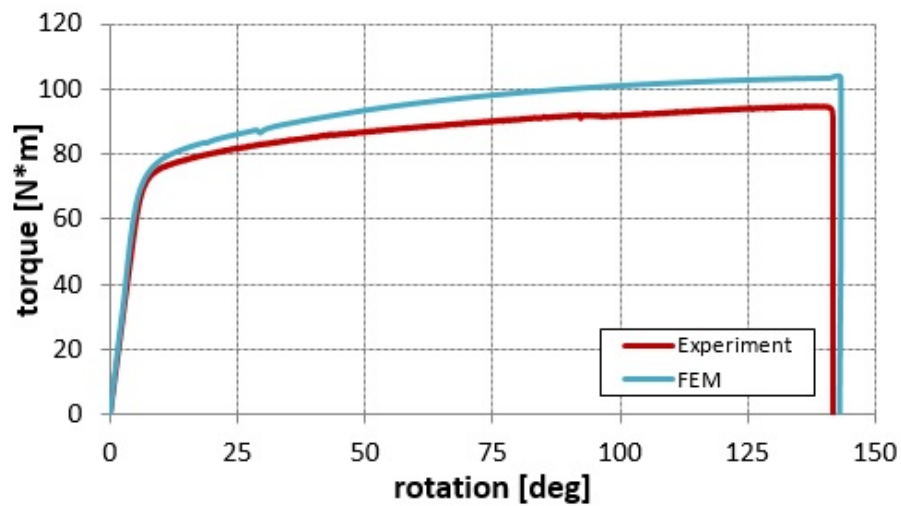Figure 5.4: Lode angle-PEEQ evolution curve in the pure torsion test.

Figure 5.5: Experimental and numerical torque-rotation data in the pure torsion test.

Torsion+20KN tension

The plasticity and damage model mentioned in table 5.2 has been implemented to the finite element model of the torsion+20KN tension test and also to the all tests in the following simulations. Figure 5.6 shows the distribution of the PEEQ in the
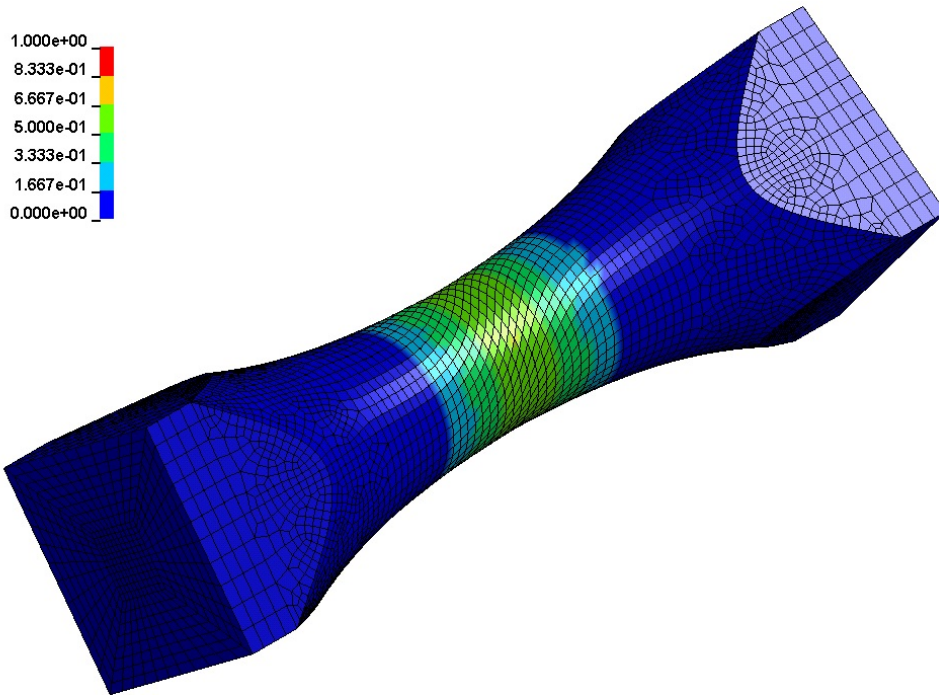
Figure 5.6: Equivalanet plastic strain contour at failure moment in the torsion+20KN tension test.

model at the numerical failure point. Figure 5.7 shows the damage, plasticity and Von Mises stress contour at failure moment in the middle cross section of the specimen which is the place of the failure occurrence. As it can be seen, failure starts from the outer surface of the specimen and evolves towards the center. Similar to the model of the pure torsion test, value of the equivalent plastic strain, triaxiality and Lode angle has been extracted in the critical element of the model. Figures 5.8 and 5.9 show the triaxiality-PEEQ and Lode angle-PEEQ graphs obtained from the analysis. These data has been obtained from the finite element model of the test with the material model without damage and the plasticity model which has been mentioned in section 5.1. Average value of the triaxility and Lode angle respectively according to the equations 5.4 and 5.5 has been calculated also and been shown in the figures. A comparison between the experimental and numerical torque-rotation data of the test is shown in figure 5.10. As it can be seen failure point is predicted properly by the finite element model.
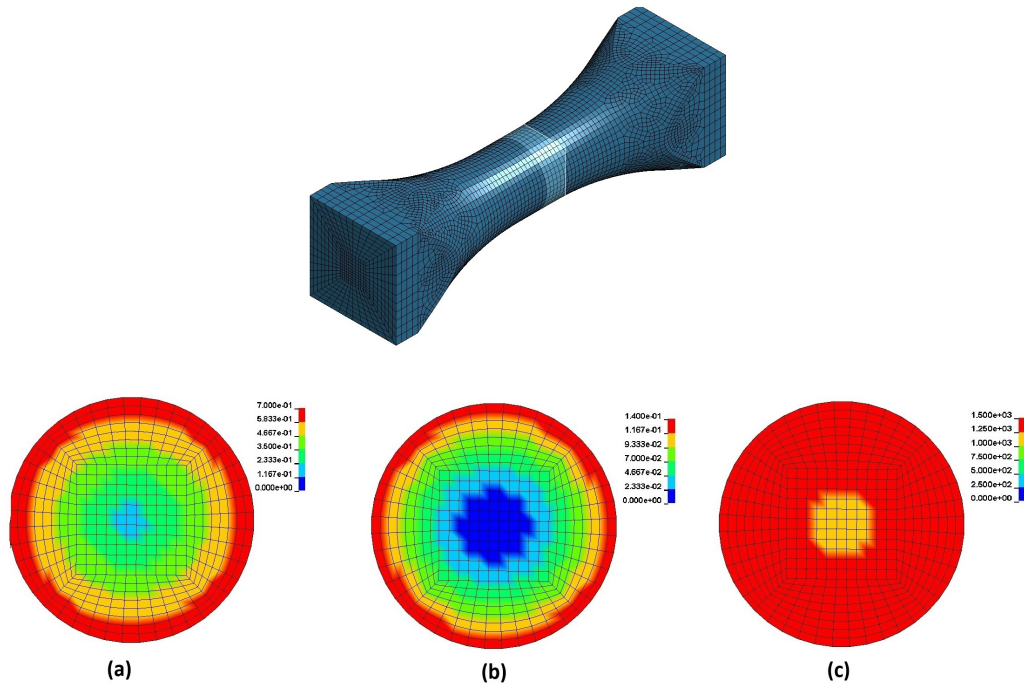
Figure 5.7: (a)PEEQ (b)Damage and (c)Von Mises stress contour in the middle cross section of the specimen of torsion+20KN tension test.
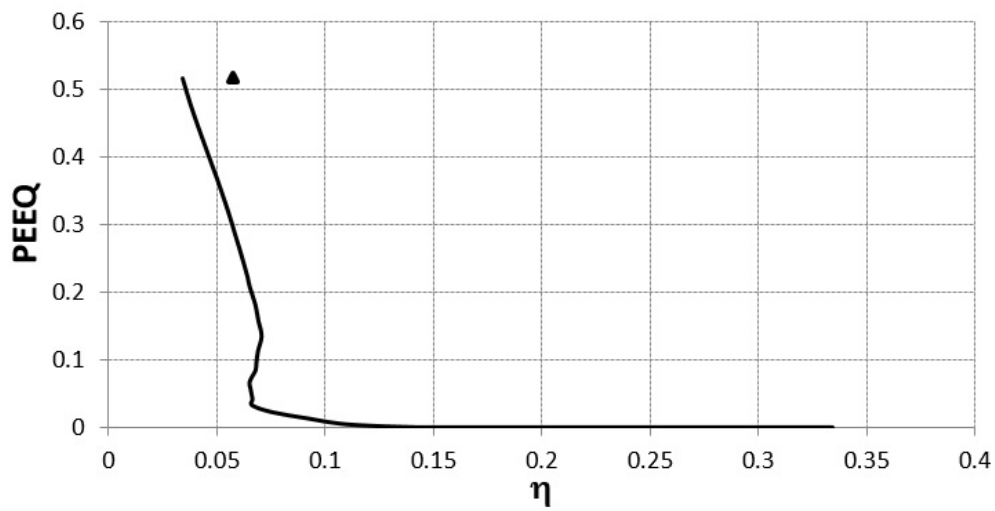
Figure 5.8: Triaxiality-PEEQ graph in the torsion+20KN tension test.

60
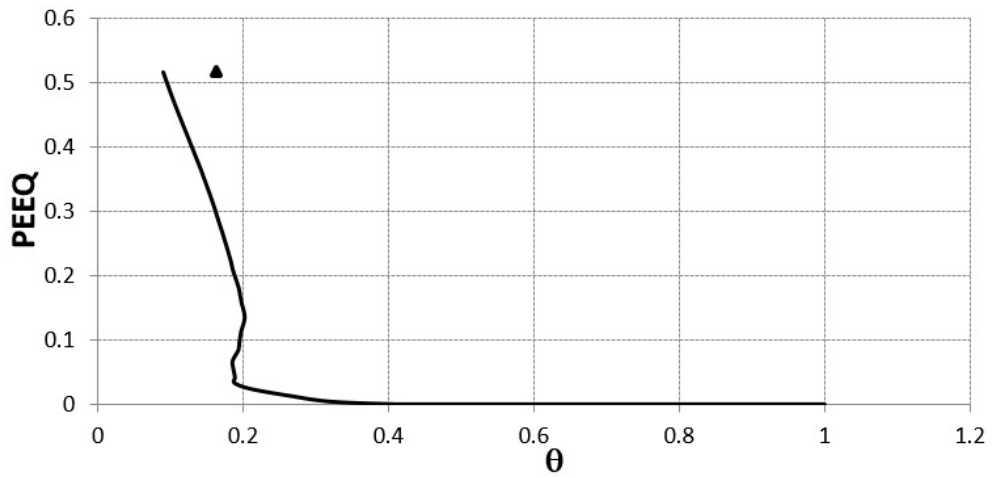
Figure 5.9: Lode angle-PEEQ graph in the torsion+20KN test.
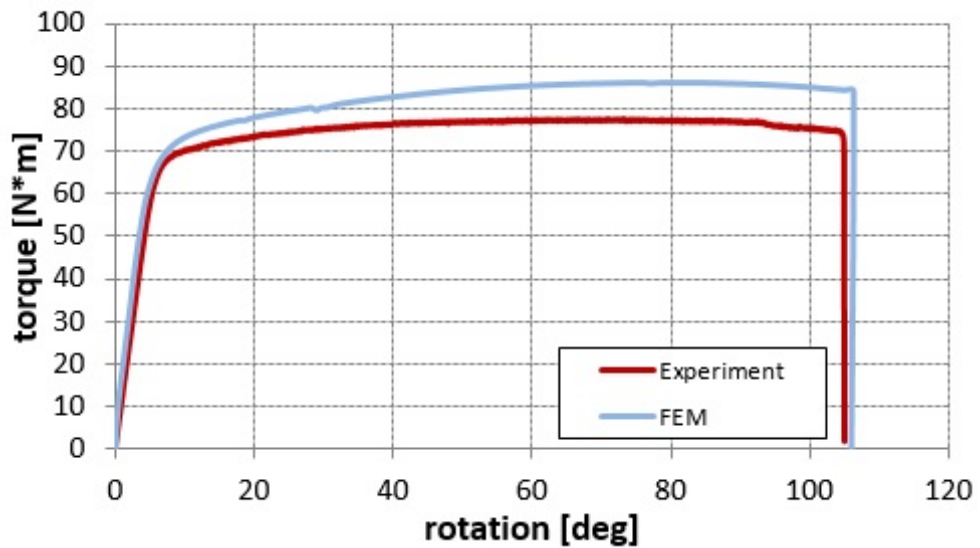

Figure 5.10: Comparison of the torque-rotation results of the experimental and numerical resluts in the torsion+20KN tension test.

Torsion+30KN tension

The similar analysis like the previous tests has been done for torsion+30KN tension test. Figure 5.11 shows the damage contour before and after failure of the specimen. Triaxiality-PEEQ and Lode angle-PEEQ evolution graphs and average values has been shown in figures 5.12 and 5.13 respectively. Damage starts from the outer surface and evolves towards the center. Comparison of the experimental

61
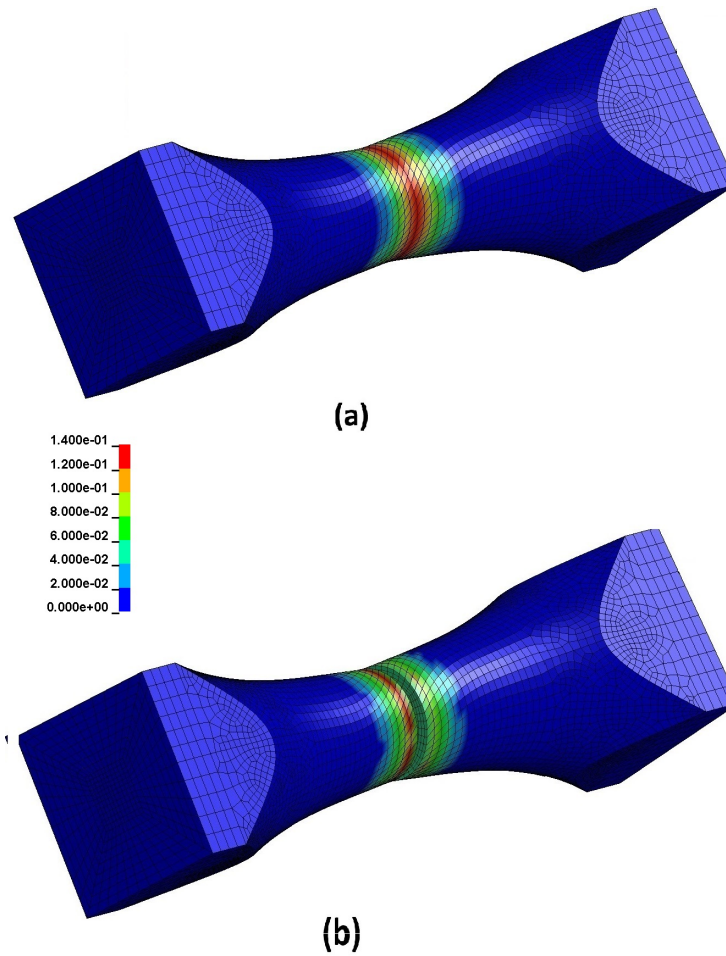
Figure 5.11: Damage contour (a)before and (b)after failure in the torsion+30KN tension test.

and numerical torque-rotation data has been shown in figure 5.14.

Torsion+40KN tension

The equivalent plastic strain contour at the failure moment, for torsion+40KN tension test has been shown in figure 5.15. The maximum values are in the middle of the specimen and failure starts from the outer surface of the middle cross section. Figure 5.16 demonstrate the failed specimen and the failure surface for torsion+40KN tension test. Triaxiality-PEEQ and Lode angle-PEEQ curves can
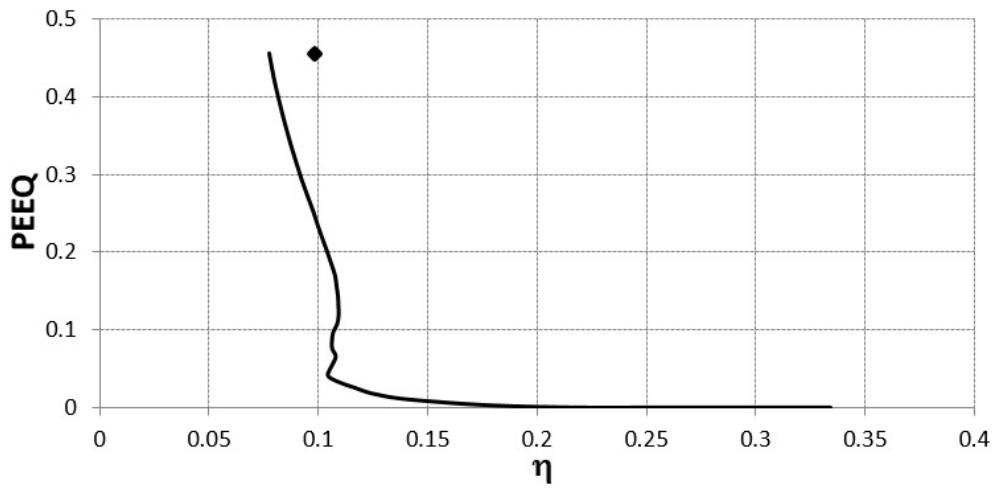
Figure 5.12: Triaxiality-PEEQ evolution curve and average values at failure in the torsion+30KN tension test.
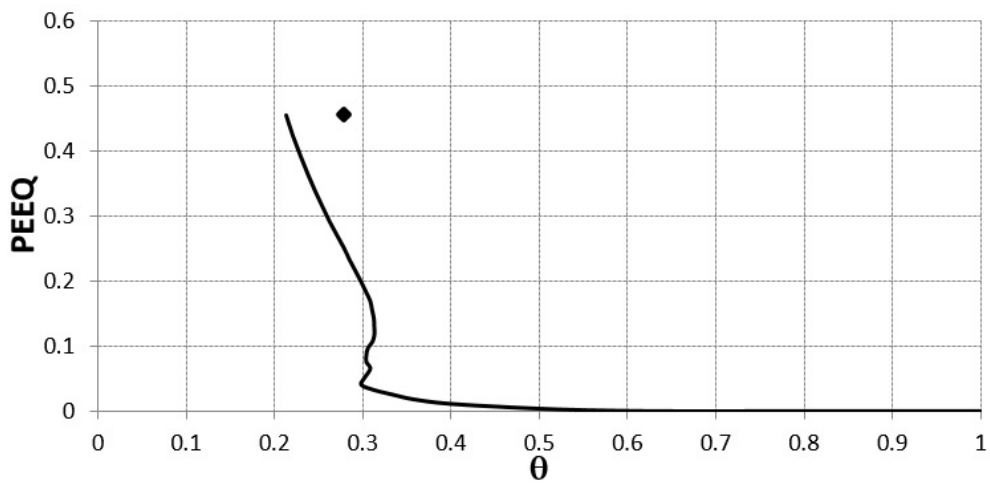
Figure 5.13: Lode angle-PEEQ evolution curve and average values at failure in the torsion+30KN tension test.

be found in figures 5.17 and 5.18 respectively. Torque-rotation data obtained from the experimental test and numerical analysis has been compared in figure 5.19.
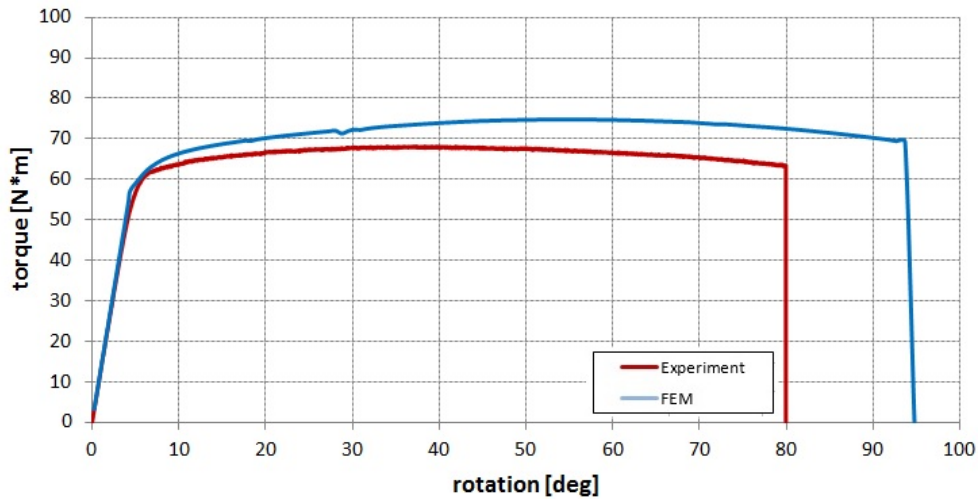
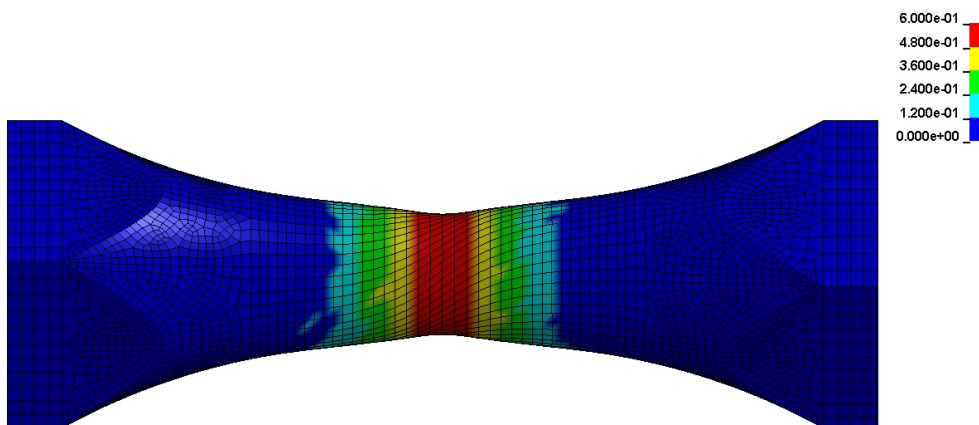Figure 5.14: Comparison of the torque-rotation results of the experimental and numerical results in the torsion+30KN tension test.

Figure 5.15: PEEQ contour at failure moment in the torsion+40KN tension test.

High triaxiality specimen (specimen B)

Specimen B is a specimen which has been designed in order to have high stress triaxialites and stress concentration in the test. Figure 5.20 shows Von Mises stress contour before failure. As it can be seen high values of stress has been concentrated in the notched region. Due to the symmetry and high values of stress, damage is also highly concentrated in the notch region and failure starts in the middle cross section A-A as it has been shown in figure 5.21(a). In the cross section A-A maximum values of damage are in the central region (figure 5.21(b)) and therefore according to the model, failure will start from the center of the specimen
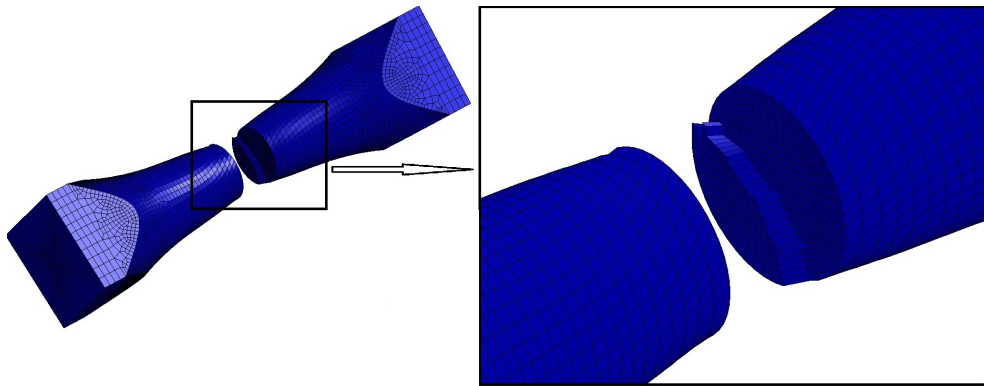
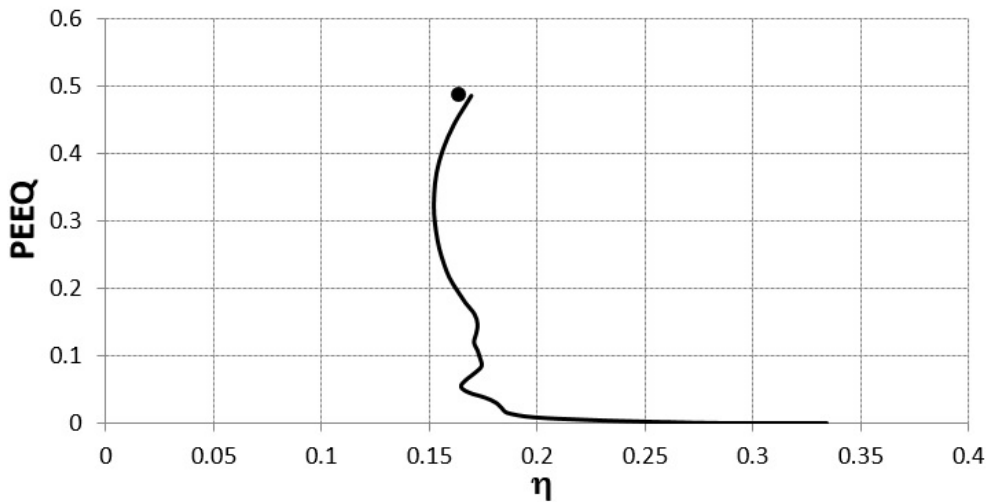Figure 5.16: Specimen after failure in the torsion+40KN tension test.

Figure 5.17: Triaxiality-PEEQ evolution curve in the torsion+40KN tension test.

and propagates towards the surface and is different from torsion tests which failure starts from the surface and not from the center (figure 5.7). Triaxiality-PEEQ and Lode angle-PEEQ evolution curves during the loading has been shown in figures 5.22 and 5.23 respectively. Failure points has been mentioned also in the figures and has been calculated according to the average values of the triaxiality and Lode angle during the loading according to the equations 5.4 and 5.5. Figure 5.24 shows experimental and numerical load-displacement data obtained for specimen B.
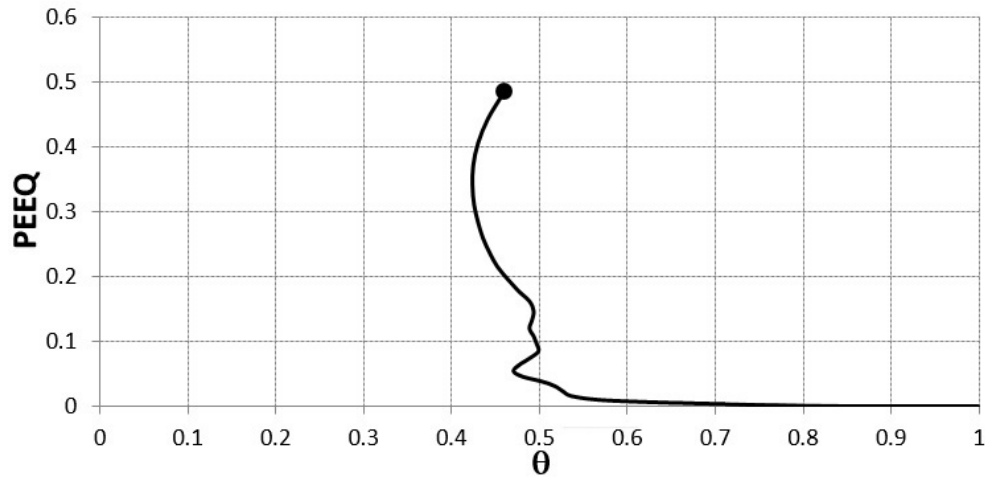
Figure 5.18: Lode angle-PEEQ evolution curve in the torsion+40KN tension test.
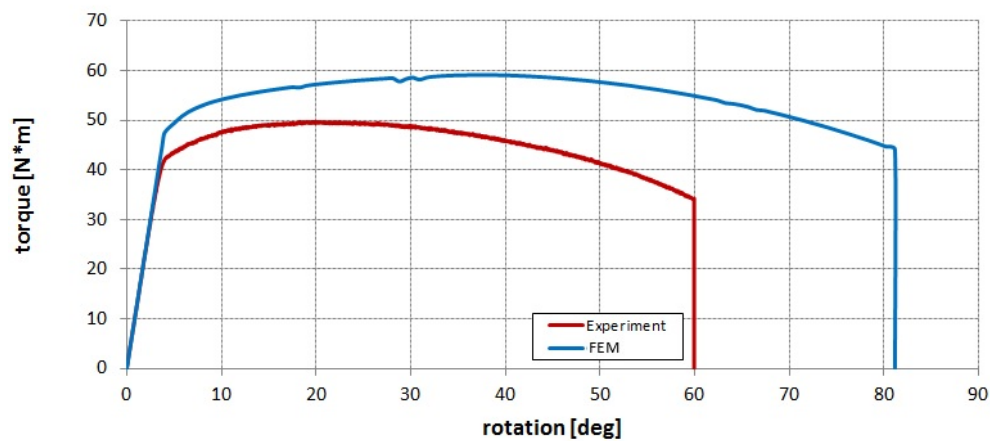

Figure 5.19: Comparison of the torque-rotation results of the experimental and numerical results in the torsion+40KN tension test.

Flat smooth specimen

Last specimen in the first series experimental tests is the flat one(see table 3.2). Load-displacement data comparison between the experimental and numerical results has been shown in figure 5.25. Like other experiments evolution of the triaxiality and Lode angle in the critical element of the FE model has been obtained which has been illustrated respectively in figures 5.26 and 5.27.
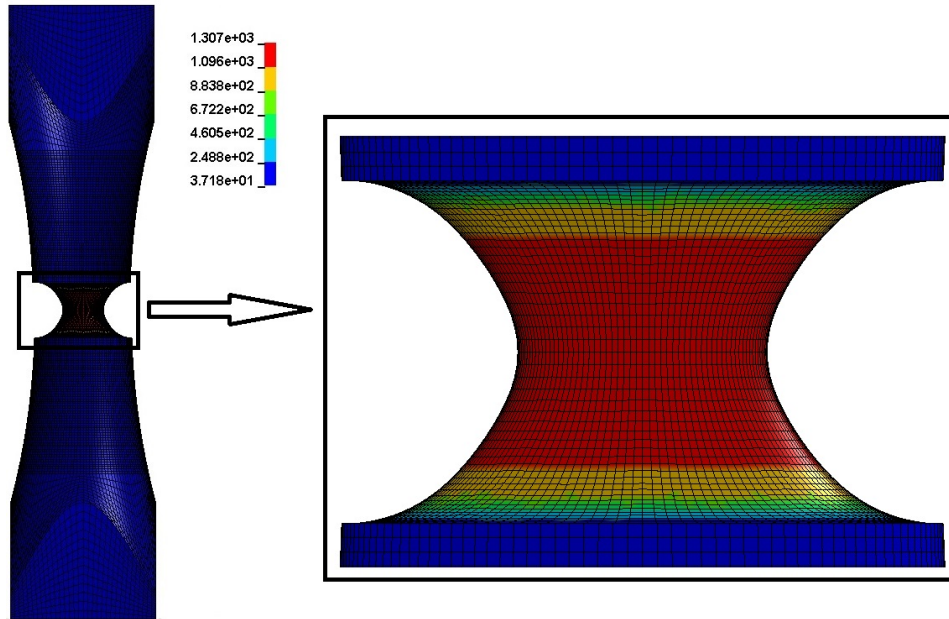
66

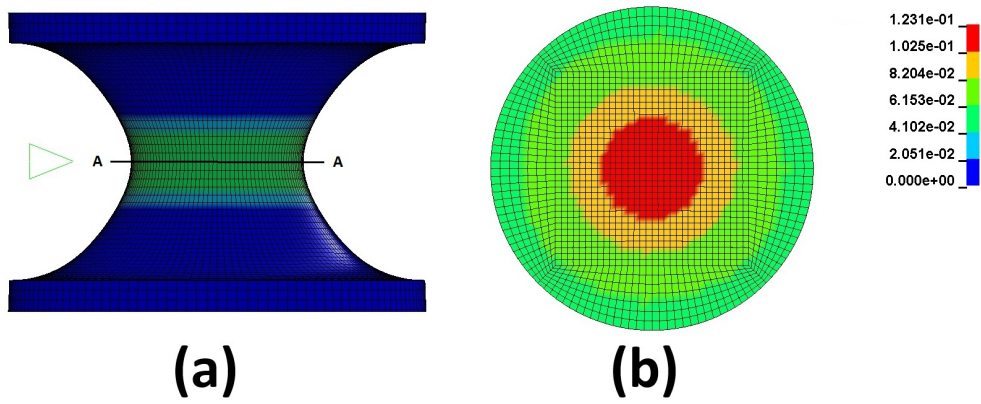Figure 5.20: Von Mises stress contour before failure in the notched specimen B.

Figure 5.21: (a)Damage contour in specimen B and location of cross section A-A(b)Damage contour in cross section A-A.
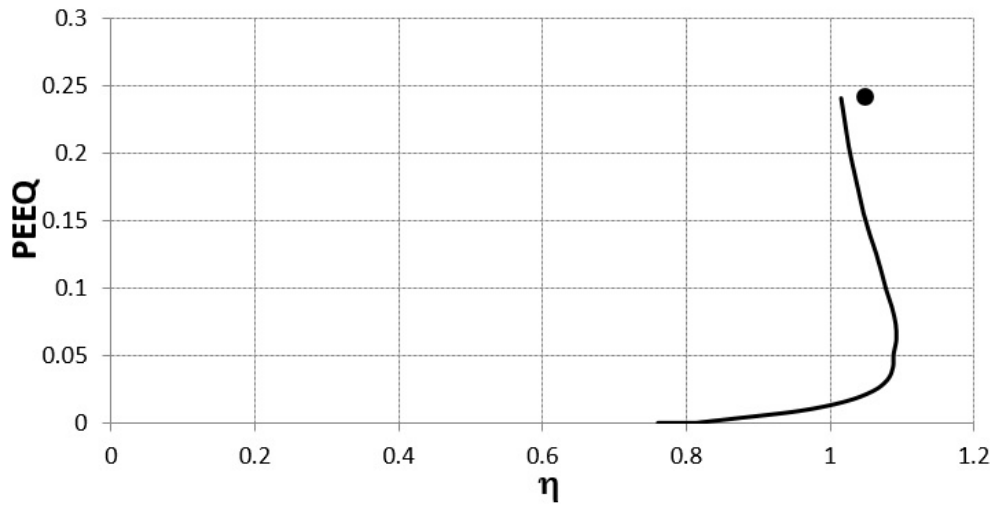
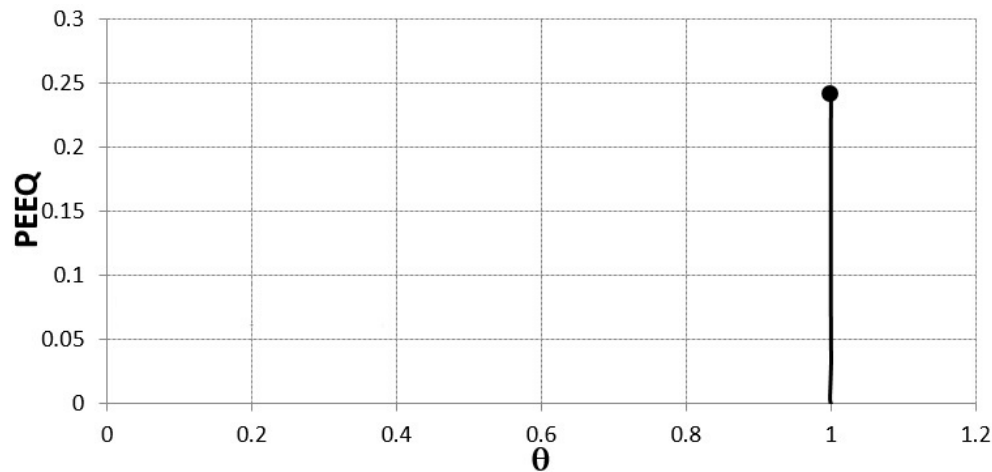Figure 5.22: Triaxiality-PEEQ evolution curve in specimen B during the loading.

Figure 5.23: Lode angle-PEEQ evolution curve in specimen B during the loading.

5.2.2 Second series of experiments:Flat specimens

20mm notched specimen

The first flat specimen in the second series of tests is specimen with 20mm notch radius which its geometry has been showed in table 3.2. As it has been mentioned in section 4.3.4 due to the symmetry one quarter of the specimen has been made in the finite element models. Like as previous models material model which has been mentioned in table 5.2 and has been obtained from the calibration, has been implemented inside the model in order to obtain numerical load-displacement results.
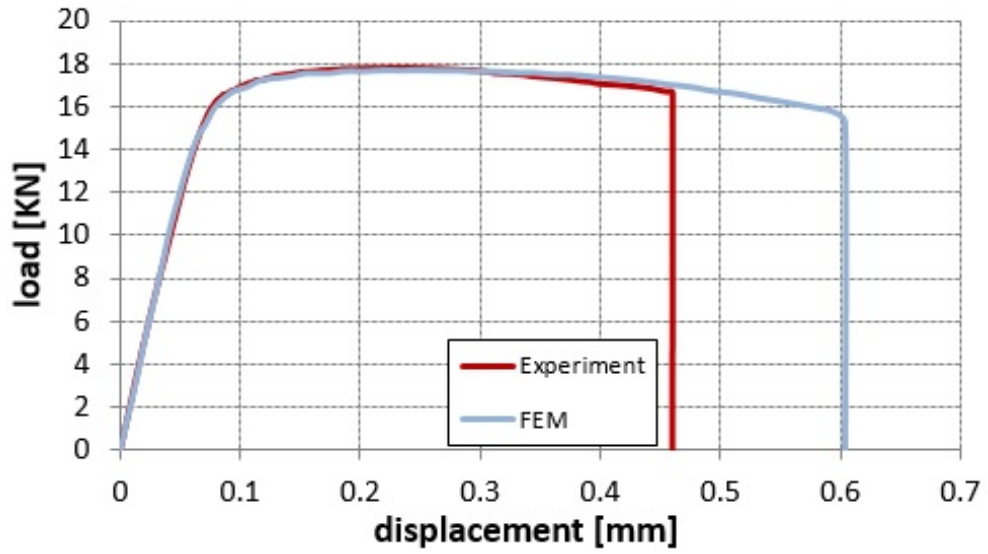
Figure 5.24: Comparison of the experimental and numerical load-displacement results in the tensile test of specimen B.
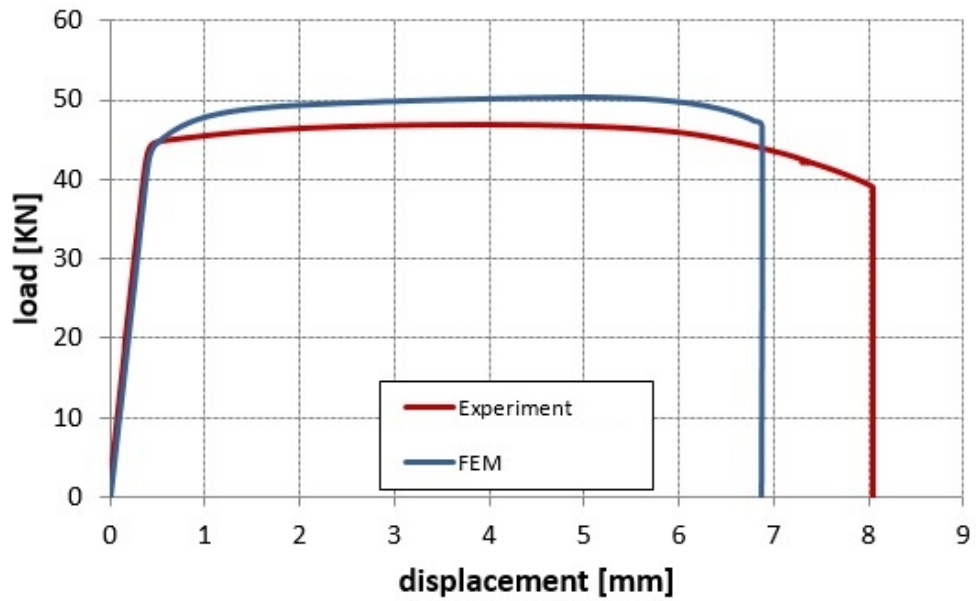

Figure 5.25: Comparison of the experimental and numerical load-displacement results in the tensile test of the smooth flat specimen.

Figure 5.28 shows the equivalent plastic strain contour before failure(numerical failure point) in the 20mm notched specimen.
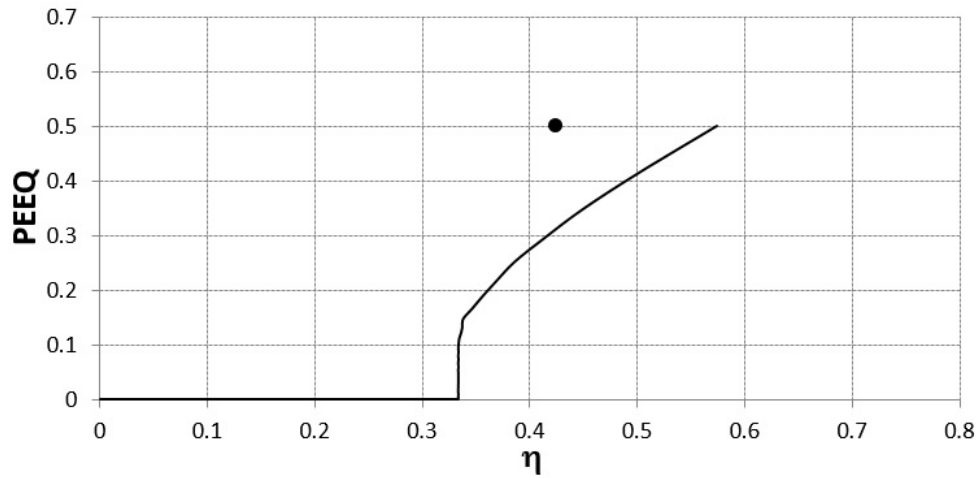
69

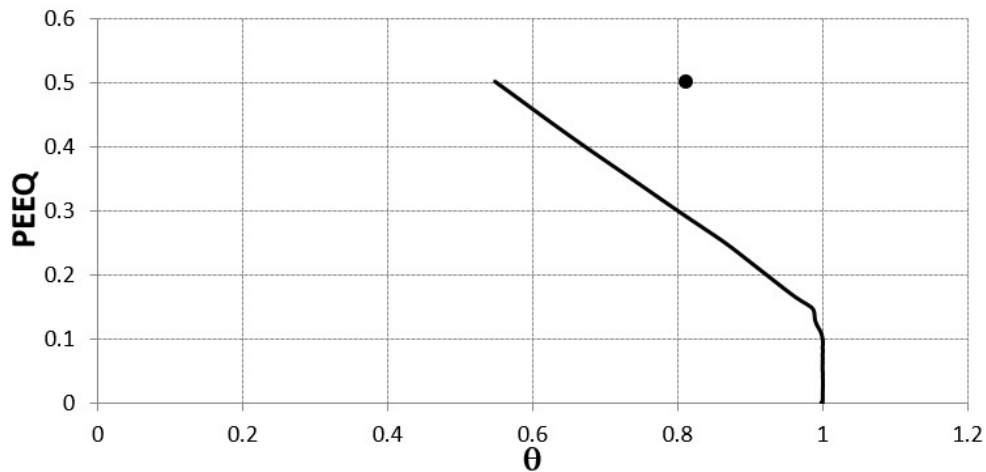Figure 5.26: Triaxiality-PEEQ curve in the smooth flat specimen.

Figure 5.27: Lode angle-PEEQ curve in the smooth flat specimen.

Due to the existence of notch, plastic strain is localized in the middle cross section of the specimen which has the smallest width. Maximum values of PEEQ and damage are located in the central region of the middle cross section of the specimen. Therefore failure starts in the middle cross section of the specimen which has the minimum width and inside the cross section propagates from center toward the surface of the specimen. Figure 5.29 shows respectively damage and PEEQ contour in the middle cross section.
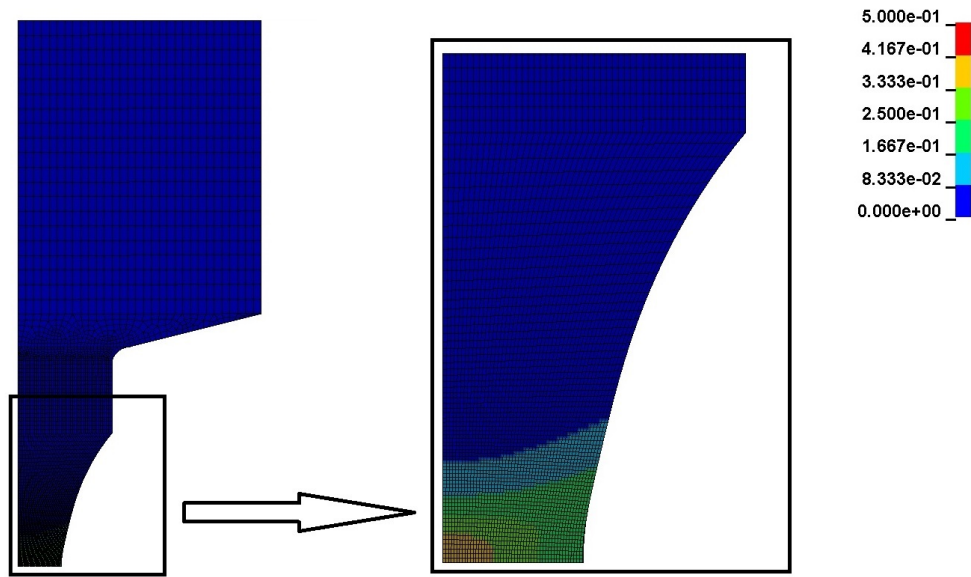
70

Figure 5.28: Equivalent plastic strain contour at failure point in the flat specimen with 20mm notch radius.
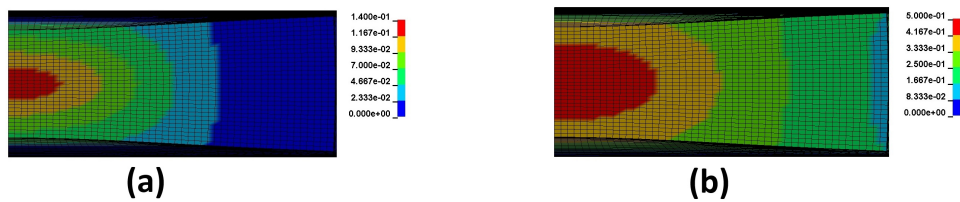

Figure 5.29: (a) Damage and (b) PEEQ contours in the middle cross section of the flat specimen with 20mm notch radius.

Similar to the other tests, triaxiality-PEEQ and lode angle-PEEQ evolution curves during the loading has been obtained also for the 20mm notched specimen and has been shown in figures 5.30 and5.31 respectively. These graphs has been obtained in the critical element (the element with the highest value of PEEQ at failure). Values of the PEEQ and average triaxiality and Lode angle has been shown also in figures 5.30 and 5.31. In order to make a comparison between the experiment and numerical model, load-displacement data obtained from experiment and finite element model has been showed in figure 5.32.
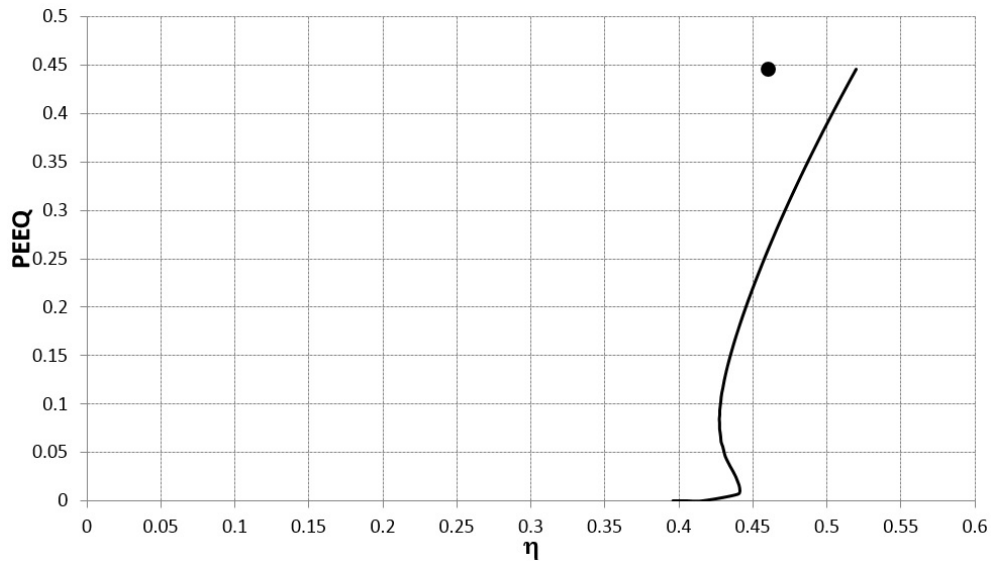
71

Figure 5.30: Triaxiality-PEEQ evolution curve during the loading in the flat speci-
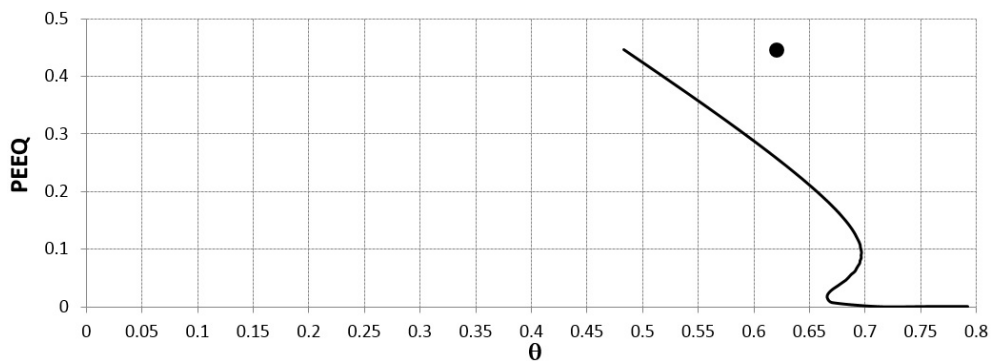men with 20mm notch radius.

Figure 5.31: Lode angle-PEEQ evolution curve during the loading in the flat spec-
imen with 20mm notch radius.

Flat specimen with 10mm notch radius

Due to the smaller value of the notch radius in this specimen relative to the pre-
vious test explained in the above section, stress is more concentrated and failure
occurs in smaller displacement. Figure 5.33 shows damage contour just before
failure in the finite element model which is a quarter of the real specimen. As it
can be seen also in this test according to the finite element models, failure starts
in the center of the specimen and propagates toward the surface and notch root.
Triaxiality-PEEQ and Lode angle-PEEQ evolution curves have been shown in fig-
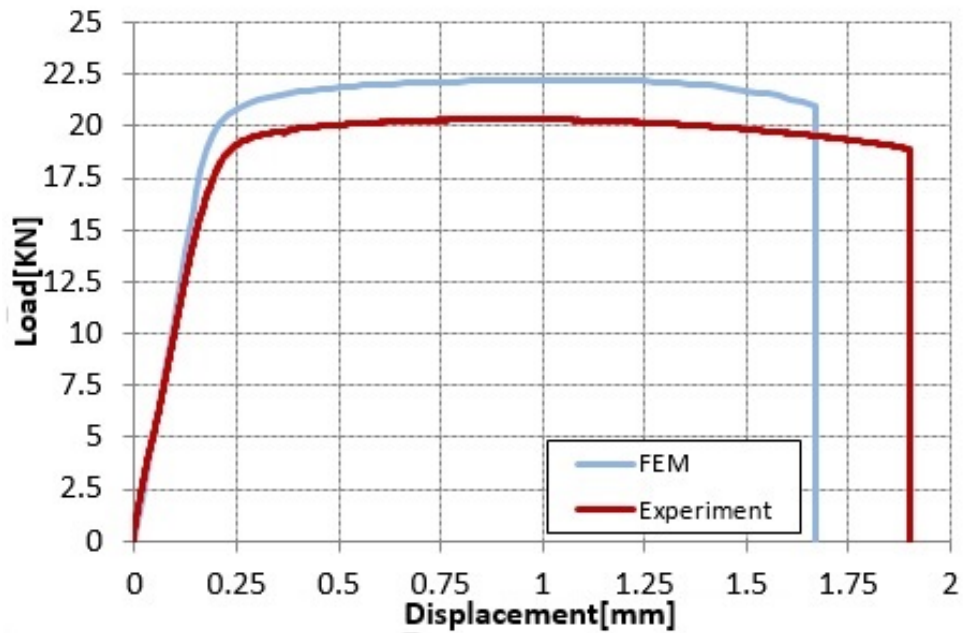
Figure 5.32: Comparison of the experimental and numerical load-displacement re-
sults in in the flat specimen with 20mm notch radius.

ures 5.34 and 5.35. Due to the existence of the sharper notch, average value of
triaxiality is higher in compare with flat specimen with 20mm notch radius. As
the most important parameter to investigate the damage models accuracy, experi-
mental and numerical load-displacement data has been compared in figure 5.36.

Flat specimen with 6.67 mm notch radius

The specimen with 6.67 mm notch radius is the specimen with the highest stress
triaxiality among the flat specimens. Triaxiality-PEEQ and Lode angle-PEEQ
evolution curves during loading has been shown in figures 5.37 and 5.38. Figure
5.39 shows experimental and numerical load-displacement data during the test. It
can be seen that displacement at failure is smaller in compare with other plane
stress specimens for the specimen with 6.67mm notch radius which is due to the
existence of higher stress triaxialities. Similar to the other notched plane stress
specimens failure starts from the center of the specimen and propagates toward
the notch root in the surface. Dunand and Mohr[61] carried out some experimen-
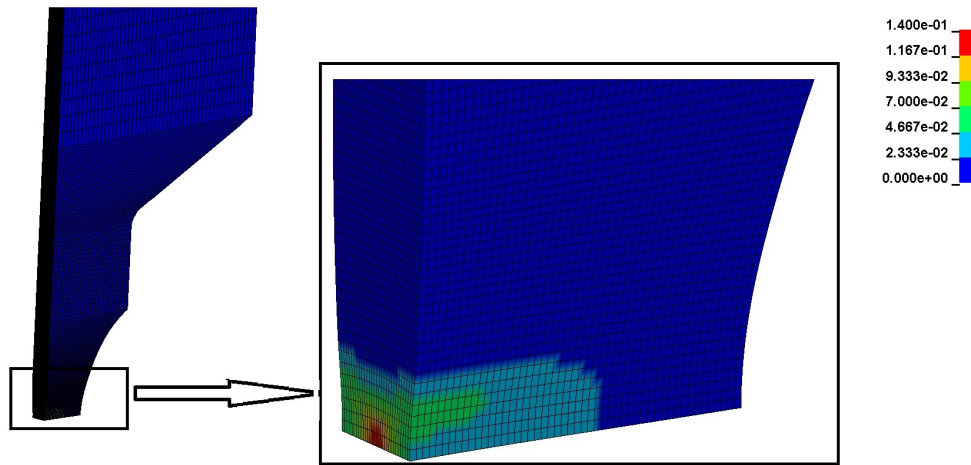
Figure 5.33: Damage contour just before the failure in the flat specimen with 10mm notch radius.

Figure 5.34: Triaxiality-PEEQ evolution curve during the loading in the flat specimen with 10mm notch radius.

tal tests and numerical simulations on the specimens made from TRIP780 steel and similar geometry of flat specimens of this research. Dunand and Mohr[61] also verified that crack will start from the center of the specimens and propagates toward center.
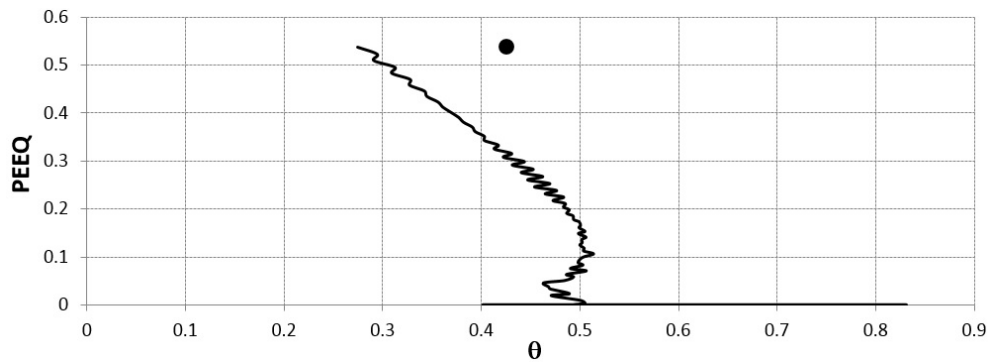
Figure 5.35: Lode angle-PEEQ evolution curve during the loading in the flat specimen with 10mm notch radius.

Figure 5.36: Comparison of the experimental and numerical load-displacement results in the plane stress specimen with 10mm notch radius.

Flat specimen with hole

Geometry of specimen with hole is slightly different from the other notched flat specimens. Evolution of stress triaxiality and Lode angle during loading is therefore different from the notched specimens. Value of stress triaxiality and Lode angle are approximately constant during the loading which is different from the

75
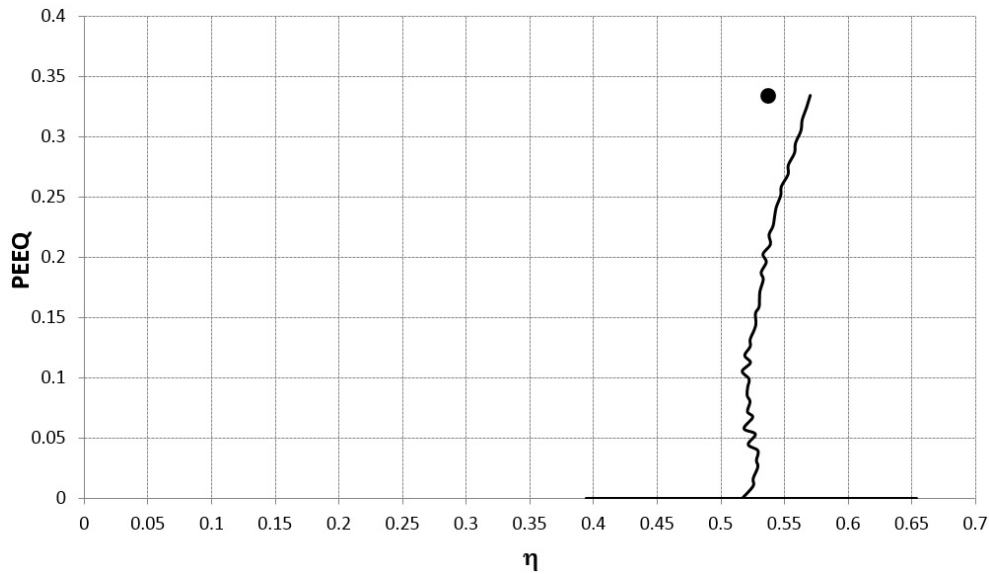
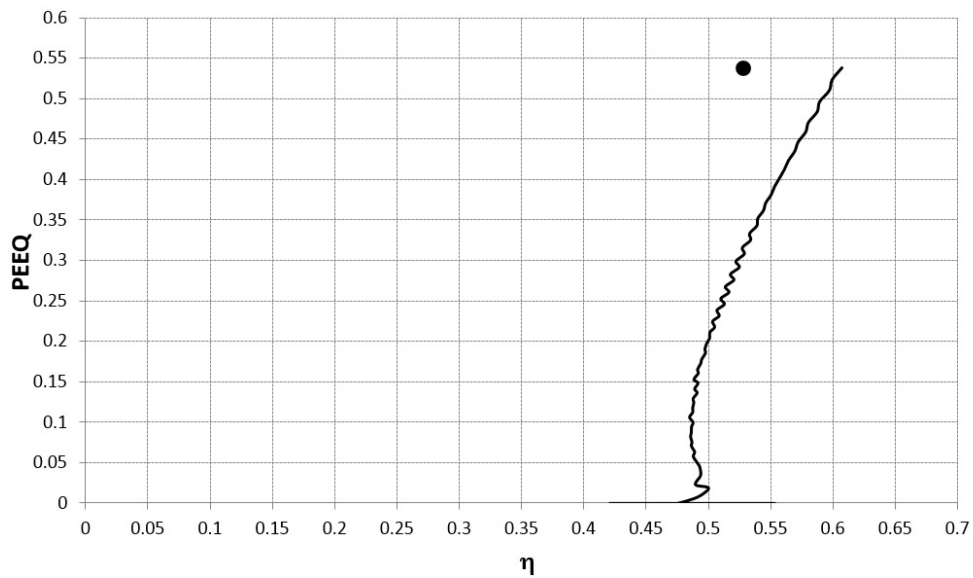Figure 5.37: Triaxiality-PEEQ evolution curve during the loading in the flat specimen with 6.67mm notch radius.
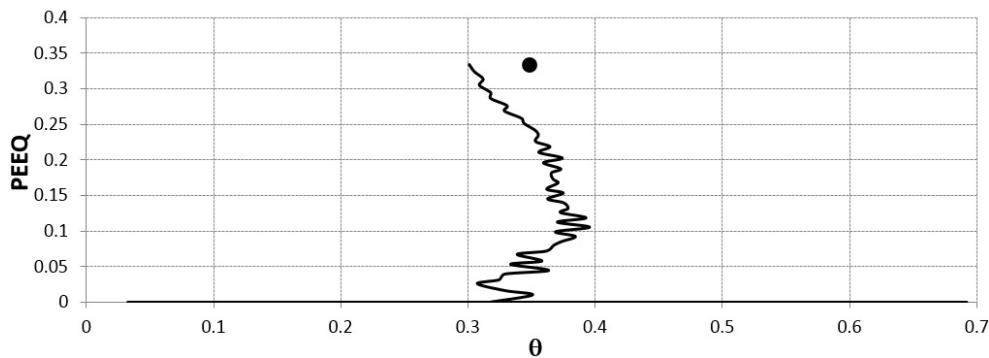
Figure 5.38: Lode angle-PEEQ evolution curve during the loading in the flat specimen with 6.67mm notch radius.

general trend of triaxiality and Lode angle in the notched flat specimens explained above. Average value of stress triaxility is smaller than the notched flat specimens however Lode angle is greater in the specimen with hole in compare with notched flat specimens. Figures 5.40 and 5.41 show triaxiality-PEEQ and Lode angle-PEEQ evolution curves during the loading and at the failure point.

From the point of view of fracture initiation, flat specimen with hole is similar to the notched flat specimens and fracture starts from the center of the specimen.
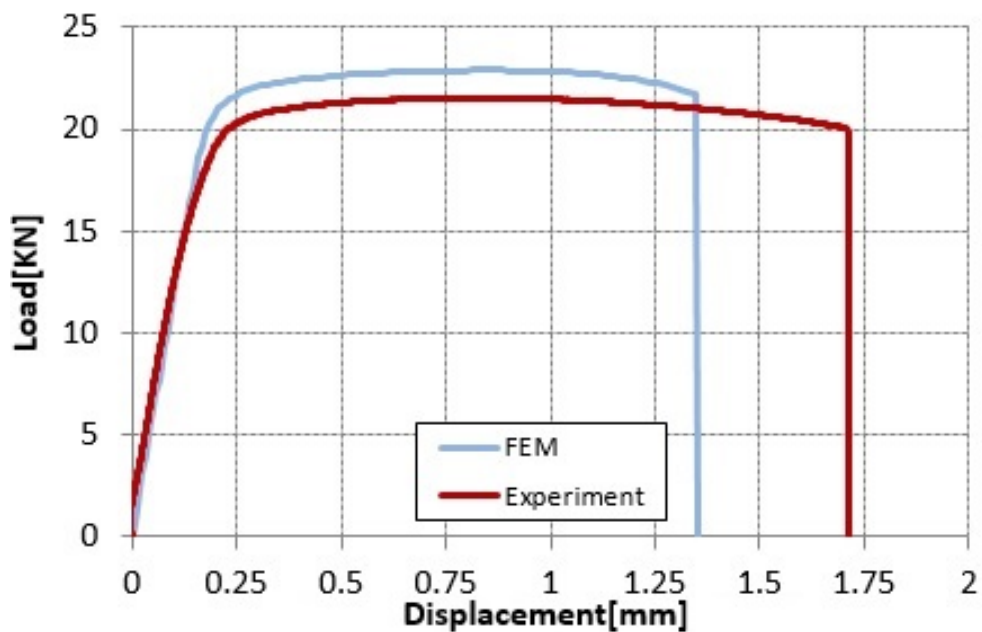
Figure 5.39: Comparison of the experimental and numerical load-displacement results in the flat specimen with 6.67mm notch radius.

Figure 5.40: Triaxiality-PEEQ evolution curve during the loading in the flat specimen with hole.

Damage contour and propagation of crack during the loading has been shown in
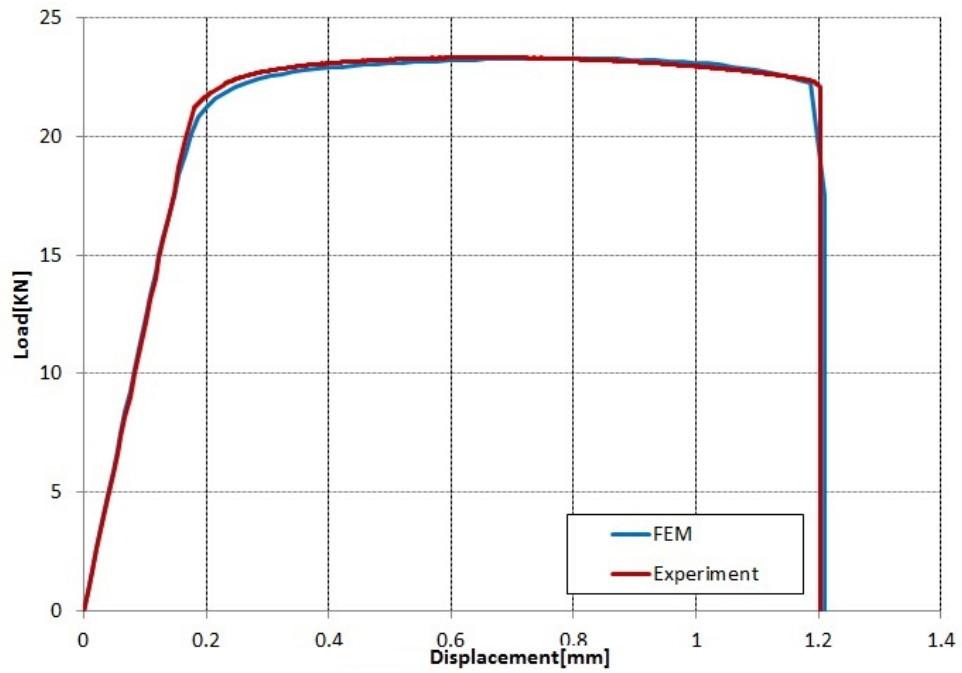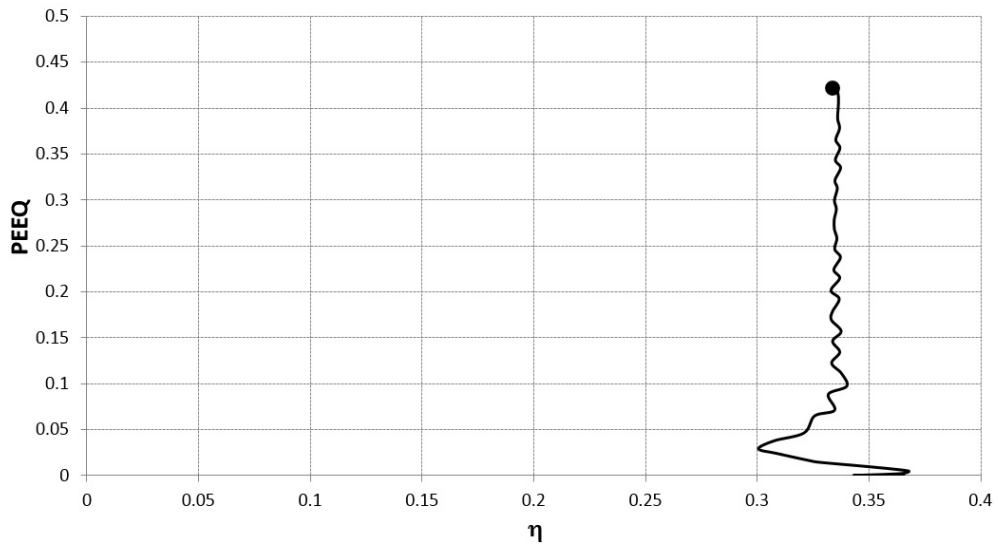
77
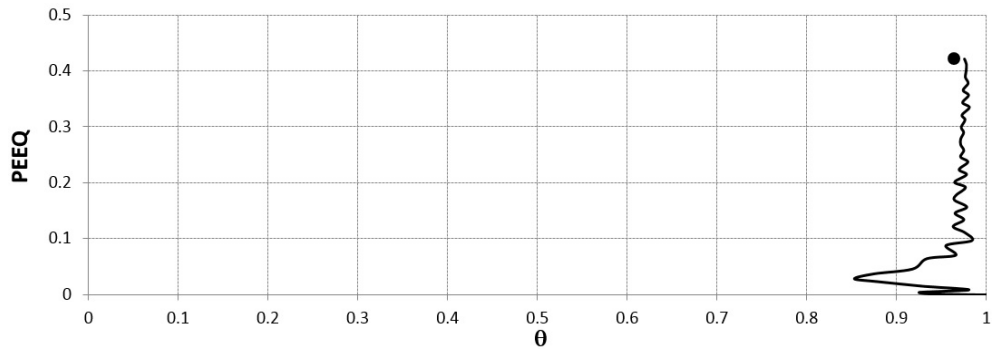
Figure 5.41: Lode angle-PEEQ evolution curve during the loading in the plane stress specimen with hole.
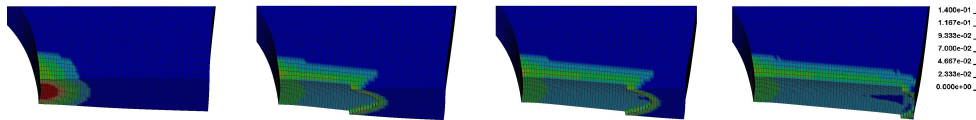
Figure 5.42: Damage contour and crack propagation in flat specimen with hole.

figure 5.42 and it is obvious that failure first stars from the center of the specimen. The fracture surface is the middle cross section of the specimen which has the minimum width and cross section area. Load-displacement data during the experiment and numerical model has been compared in figure 5.43.

Flat shear specimen

Last specimen in the flat specimen test series is the shear specimen. This specimen has been designed in order to have shear dominant failure. Figure 5.44 obviously shows that value of triaxiality during the loading is always around zero and the average value is so close to zero. This proves that failure is due to the shear and is different from the other flat specimens where failure occurs due to the tension. Figure 5.45 shows the FEM model of the shear specimen and damage contour in the failure region before and after failure. It can understood also from figure 5.45 that failure occurs due to the shear. Evolution curve of Lode angle-PEEQ during the loading at the critical element has been showed in figure 5.46. Similar to the triaxiality, Lode angle is always around zero during the test. Finally a comparison has been made between experimental and numerical load-displacement results in figure 5.47.
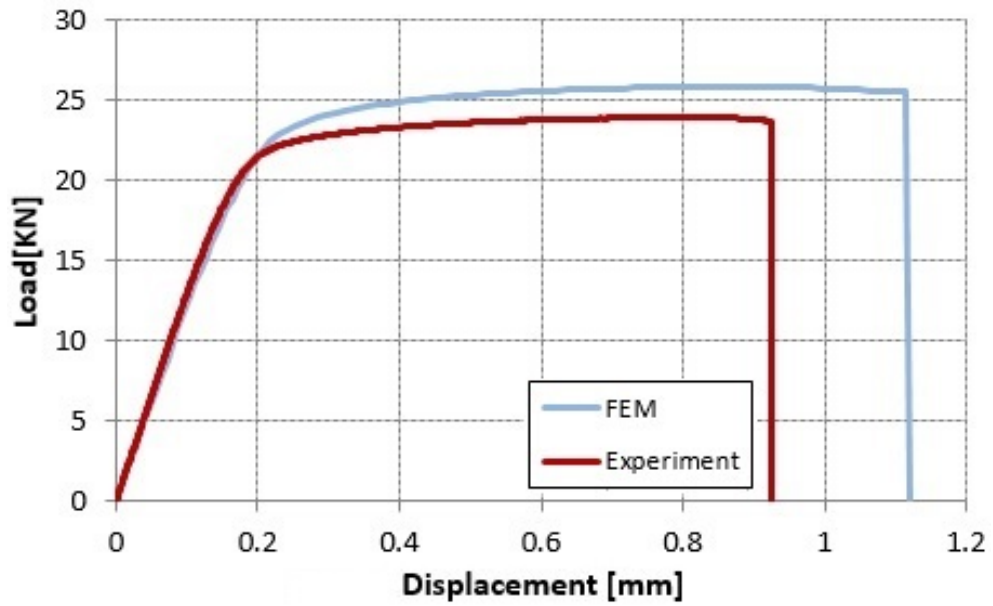
Figure 5.43: Comparison of the experimental and numerical load-displacement results in the flat specimen with hole.
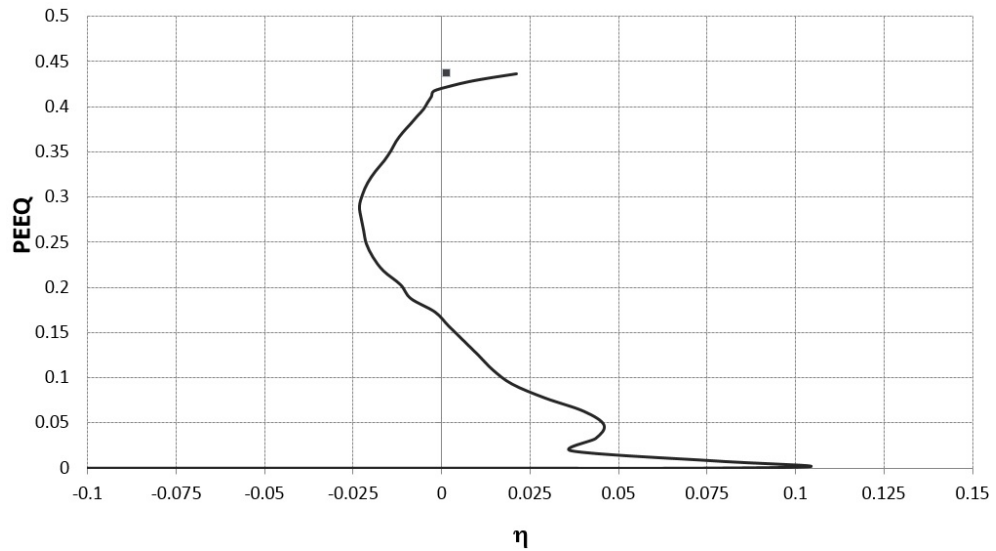
Figure 5.44: Triaxiality-PEEQ evolution curve during the loading in the flat shear specimen.
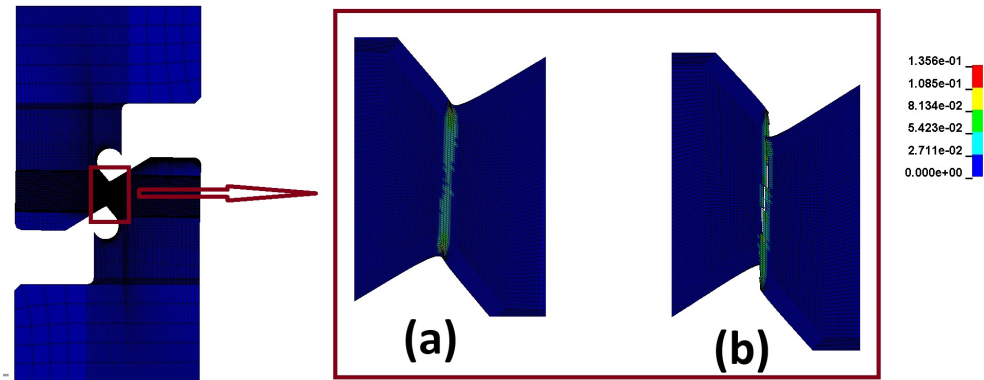
Figure 5.45: Damage contour in the flat shear specimen before and after failure.
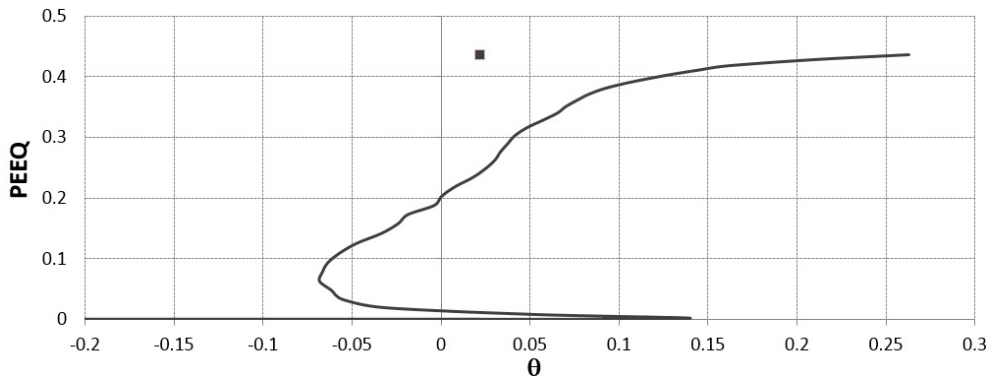
Figure 5.46: Lode angle-PEEQ evolution curve during the loading in the flat shear
specimen.

5.2.3 Third series tests: Round specimens

Round smooth specimen

Round smooth specimen of third series experimental tests has been used in order to calibrate material model (detailed information can be found in section 4.2). Therefore there is a very good agreement between the experimental and numerical load-displacement data as it can be seen in figure 4.2. Triaxiality-PEEQ and Lode angle-PEEQ curves during the loading has been extracted from the critical element of the model and has been shown in figures 5.48 and 5.49 respectively. Value of Lode angle is almost constant and equal to 1. Which is quite high relative
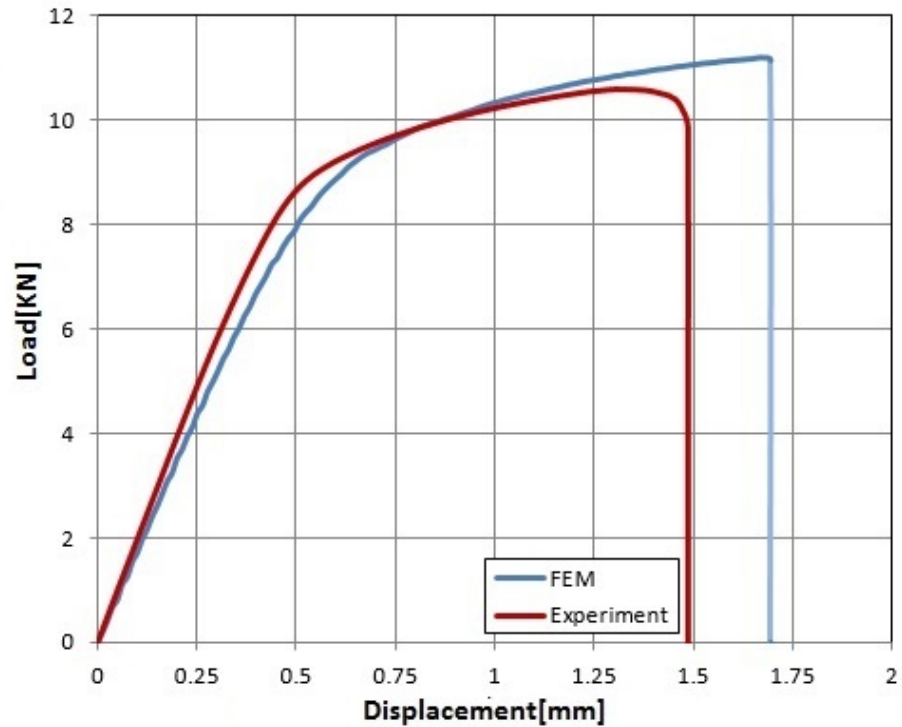
Figure 5.47: Comparison of the experimental and numerical load-displacement results in the plane stress shear specimen.

to the most of other tests in sections 5.2.1 and 5.2.2.

Round specimen with 6mm notch

Geometry of round specimen with 6mm notch can be found in table 3.6. Value of triaxiality has to be higher in the round notched specimens in compare with the round smooth specimen. Therefore as it can be seen in figures 5.50 and 5.51 which are the evolution curves of PEEQ-triaxiality and PEEQ-Lode angle, average value of triaxiality in 6mm notched specimen is higher than smooth. On the other hand failure PEEQ is smaller in compare with smooth specimen. PEEQ distribution contour at failure point has been shown in figure 5.52. Maximum PEEQ occurs in the middle of the notched region and then specimen fails also in the middle section and damage starts from the center of the specimen and propagates toward the surface. Load-displacement curves of experiment and numerical simulation has been shown also in figure 5.53.
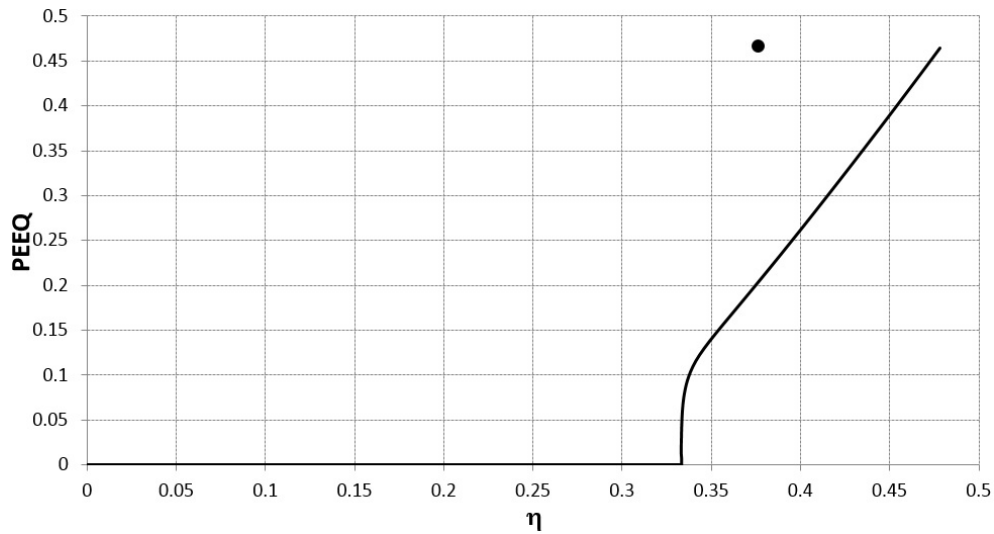
Figure 5.48: Triaxiality-PEEQ evolution curve during the loading in the round smooth specimen.
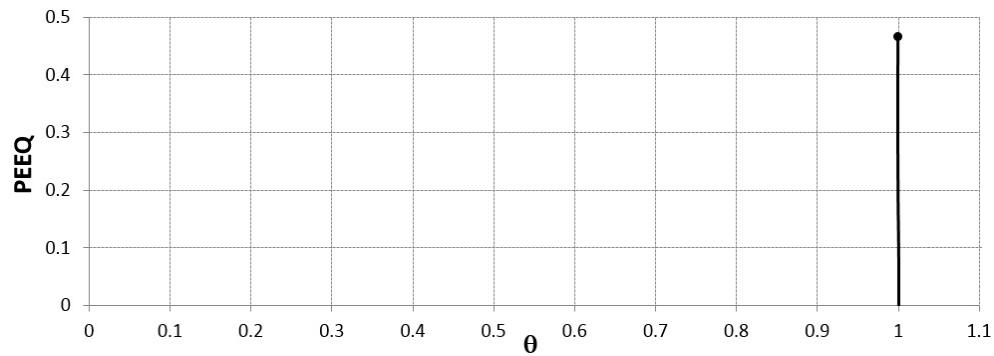
Figure 5.49: Lode angle-PEEQ evolution curve during the loading in the round smooth specimen.

Round specimen with 3mm notch

In the all of round specimens failure occurs in the middle cross section of the specimen which has the smallest diameter. Damage also starts in all cases from the center of the cross section and propagates towards the surface of the specimen. Figure 5.54 shows the evolution contours of the damage and PEEQ in the middle

82

Figure 5.50: Triaxiality-PEEQ evolution curve during the loading in the round smooth specimen with 6mm notch radius.
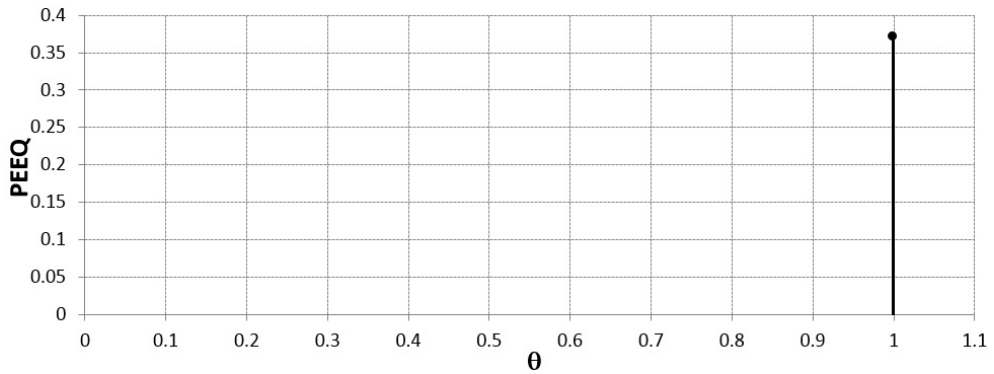
Figure 5.51: Lode angle-PEEQ evolution curve during the loading in the round specimen with 6mm notch radius.

cross section A-A during the loading which demonstrate that initially damage starts in the center. Similar to the other experiments, triaxiality-PEEQ and Lode angle-PEEQ curves have been shown also in figures 5.55 and 5.56 respectively. Average values of the triaxiality and Lode angle have been calculated and demonstrated also in figures 5.55 and 5.56. A comparison between the load-displacement data obtained from the experiment and numerical simulations has been shown in figure 5.57.
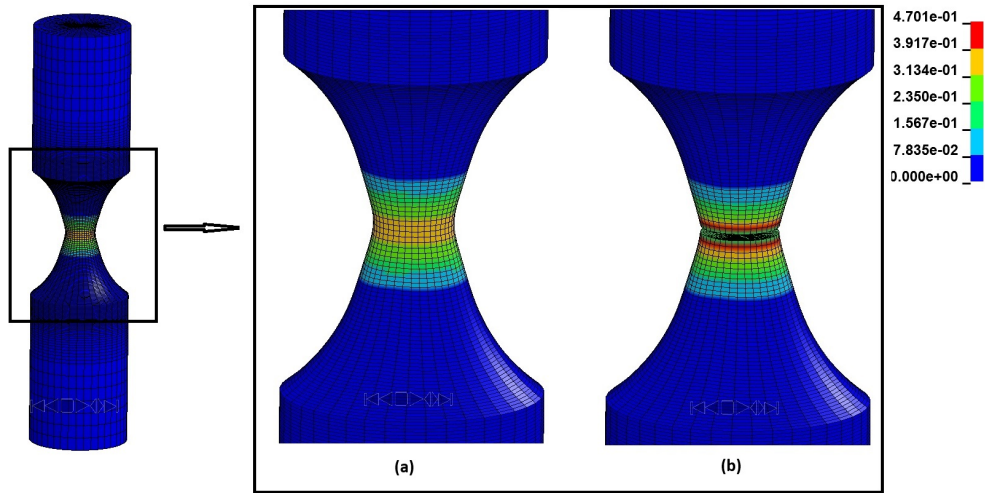
Figure 5.52: PEEQ distribution contour in the round specimen with 6mm notch radius.
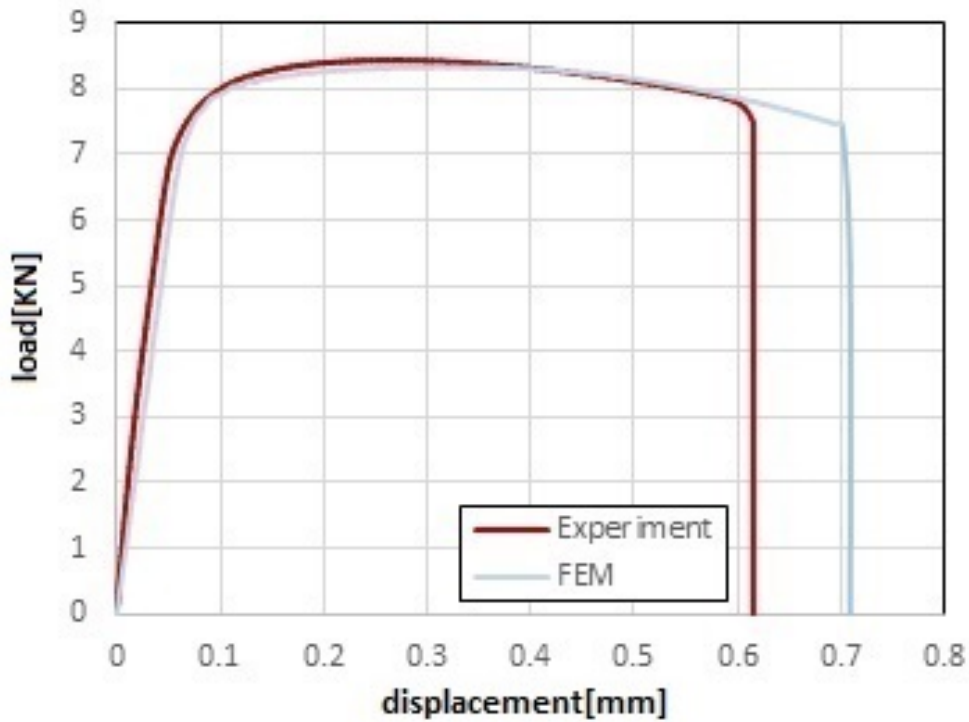
Figure 5.53: Load-displacement data comparison between experiment and numerical simulations in the round specimen with 6mm notch.
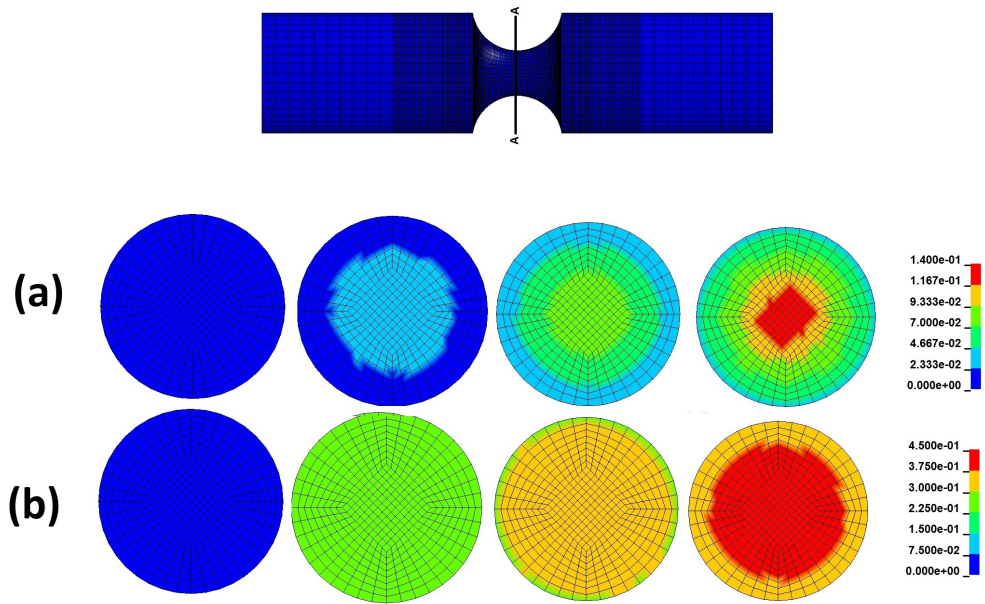
Figure 5.54: (a)Damage and (b)PEEQ contours during the loading in the round specimen with 3mm notch radius.
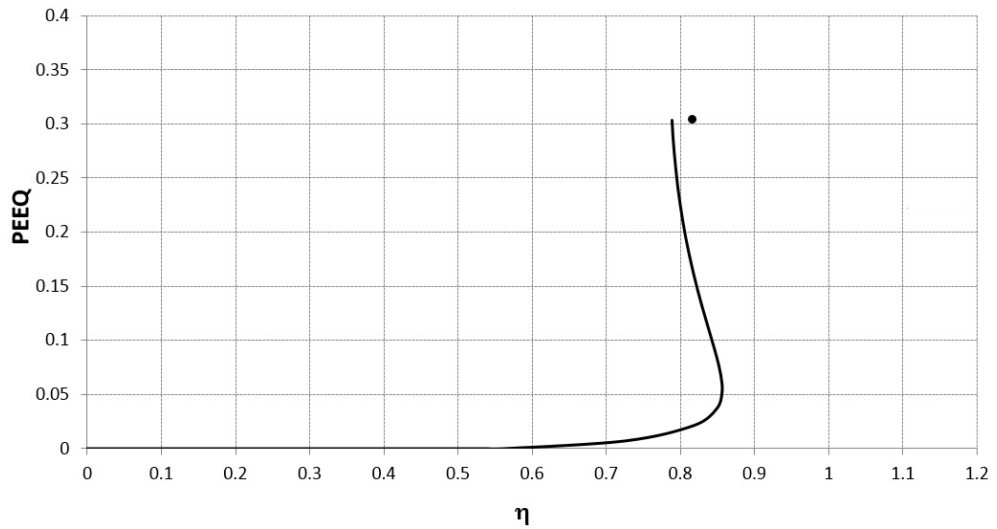
Figure 5.55: Triaxiality-PEEQ evolution curve during the loading in the round specimen with 3mm notch radius.

85
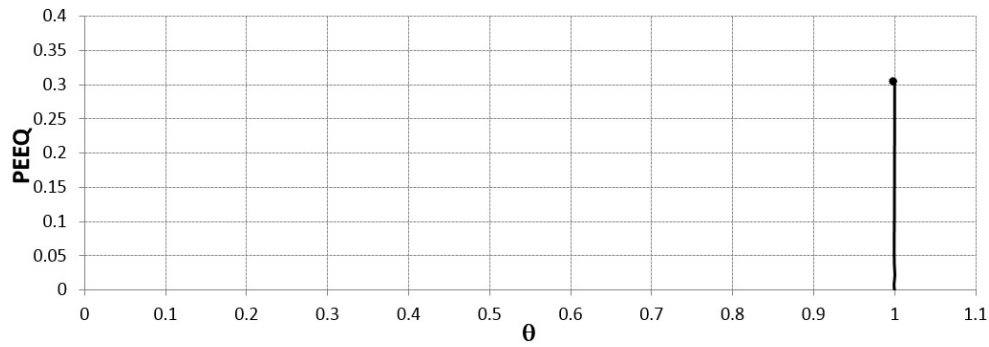
Figure 5.56: Lode angle-PEEQ evolution curve during the loading in the round specimen with 3mm notch radius.
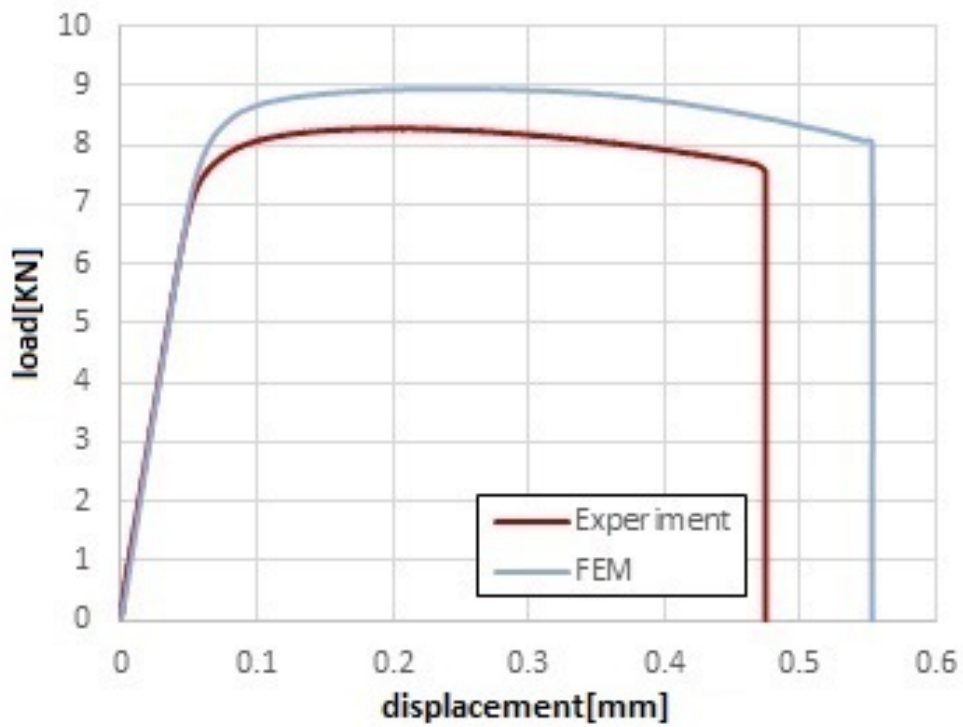
Figure 5.57: Load-displacement data comparison between experiment and numerical simulations in the round specimen with 3mm notch.

Round specimen with 1.5mm notch

Round specimen with the 1.5mm notch radius has the sharpest notch among the notched specimens of these series of tests and therefore highest values of stress

86
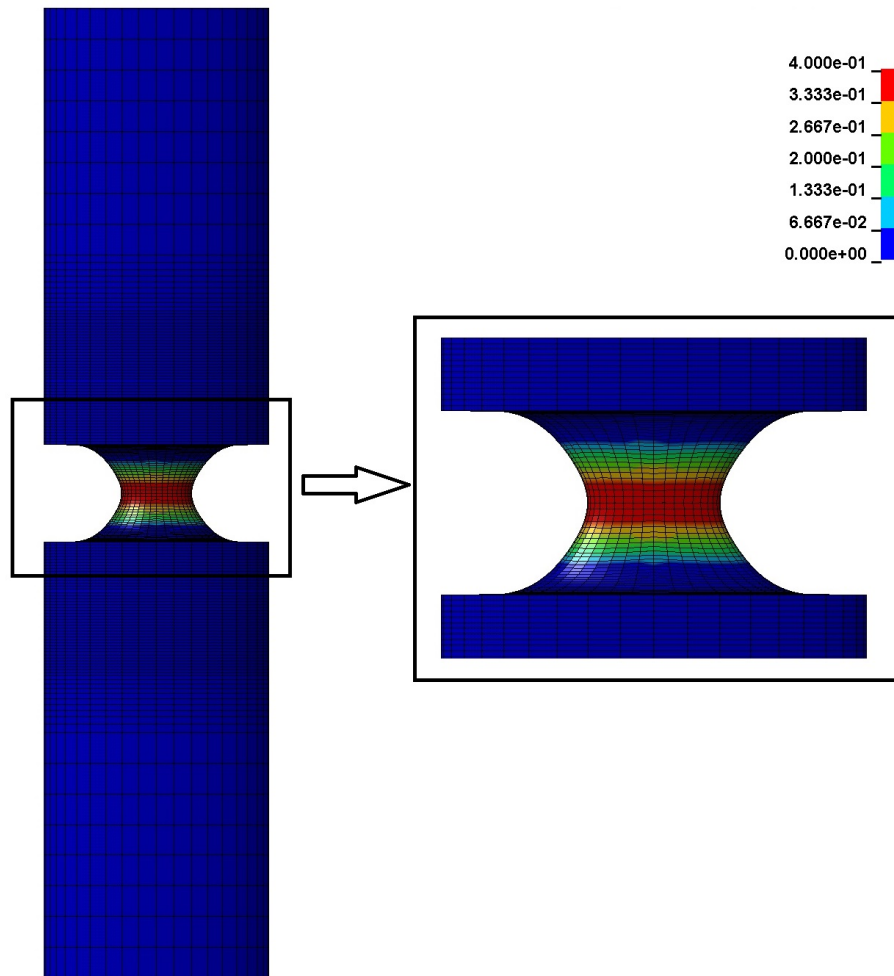
Figure 5.58: PEEQ contour at the numerical failure point in the round specimen with 1.5mm notch radius.

concentration in the notched region and highest stress triaxiality also. Figure 5.58 shows the PEEQ contour in the specimen at the numerical failure moment and as it can be seen equivalent plastic strain is highly concentrated in the notched region. Triaxiality-PEEQ and Lode angle-PEEQ evolution curves combined with the average values of triaxiliy and Lode angle during the loading have been shown also in figures 5.59 and 5.60.

As it has been mentioned before, in the all of these series of experiments due
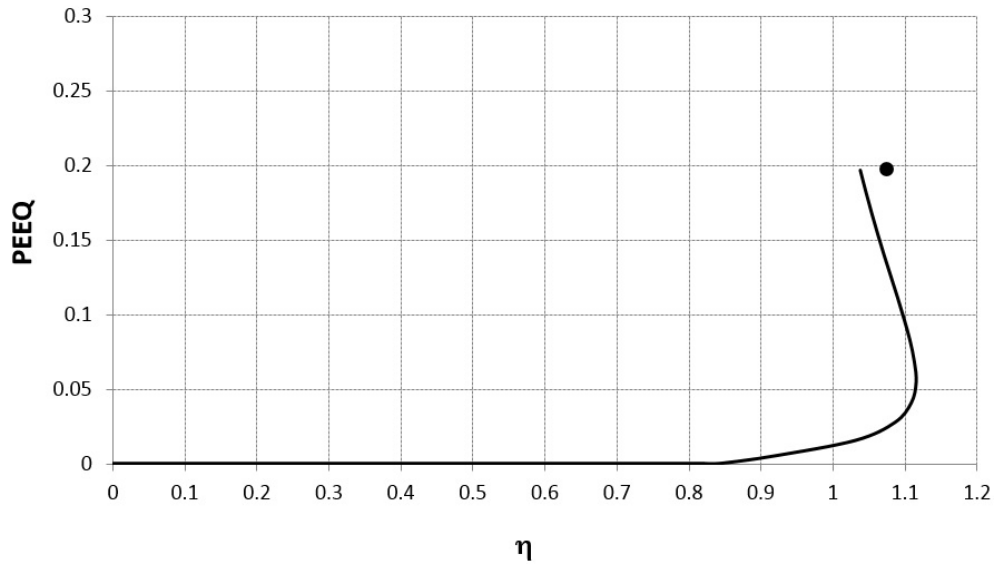
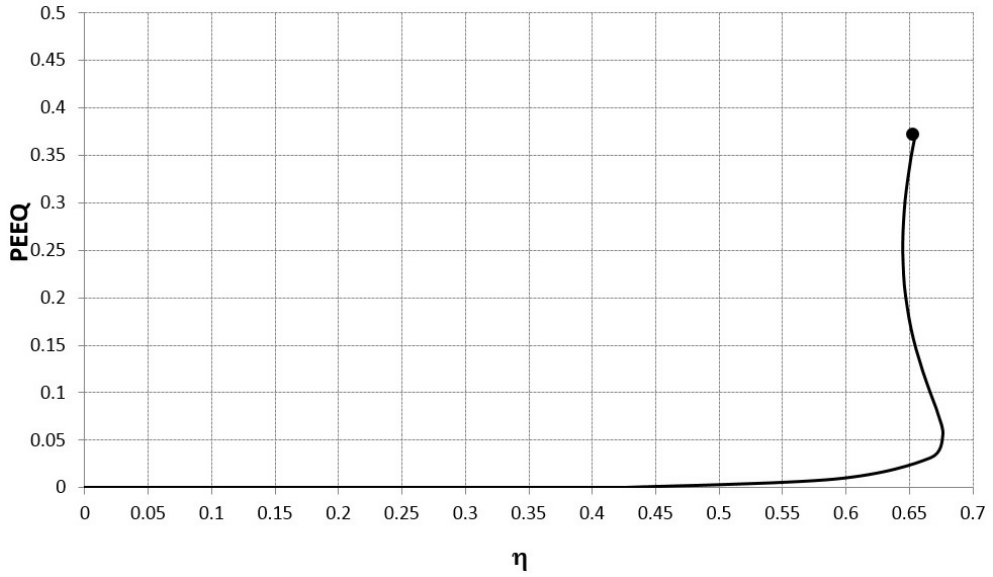Figure 5.59: Triaxiality-PEEQ evolution curve during the loading in the round specimen with 1.5mm notch radius.
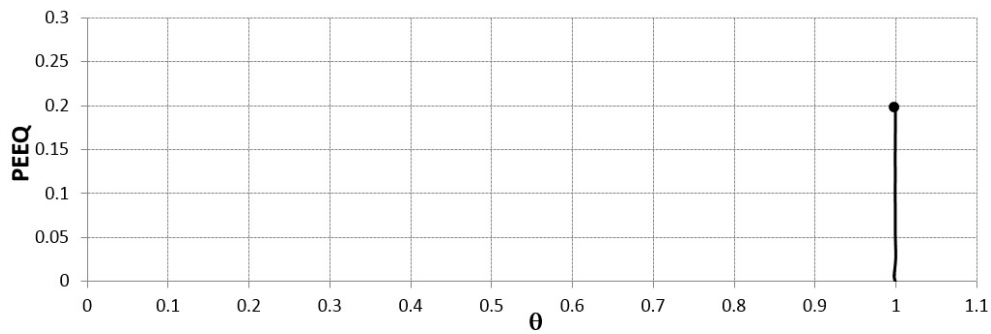
Figure 5.60: Lode angle-PEEQ evolution curve during the loading in the round specimen with 1.5mm notch radius.

the existence of the notch failure occurs in the middle of the specimen which has the minimum cross section area. Figure 5.61 shows damage, PEEQ and Von Misses stress contours in the middle cross section at the failure moment. Damage starts from the center and evolves toward the surface of the specimen. Load-displacement curves of experiment and finite element simulation can be found in figure 5.62.

Failure diameter of the third series specimens

In the third series of experiments, failure diameter of the specimens has been mea-
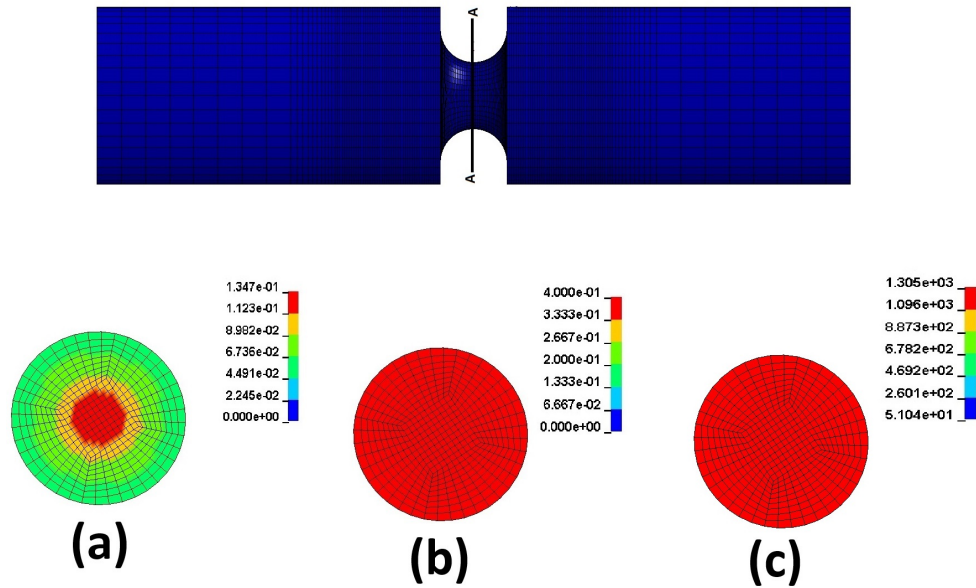
Figure 5.61: (a)Damage and (b)PEEQ and (c) Von Mises stress contours at the numerical failure moment in the round specimen with 1.5mm notch radius.

sured also. These specimens are round and therefore it is possible to measure the average failure strain using Bridgman's solution (equation 5.6):

$$\varepsilon = 2ln(\frac{\phi_0}{\phi}) \qquad (5.6)$$

Initial and failure diameter of the all of round specimens of the third series has been measured. Failure diameter of the corresponding finite element models has been measured also. Average plastic strain according to the equation 5.6 has been calculated for each test. Table 5.3 shows the obtained values.

Table 5.3: Initial and failure diameter of the round specimens.

| Specimen geometry	Experiment			FEM		
	Initial diameter(mm)	Failure diameter(mm)	Failure strain	Initial diameter(mm)	Failure diameter(mm)	Failure strain
Round smooth	3.164	2.442	0.51804	3	2.23899	0.58517
Round notch 6mm	3.097	2.71	0.26697	3	2.53728	0.33504
Round notch 3mm	2.968	2.539	0.31224	3	2.56584	0.31265
Round notch 1.5mm	2.993	2.71	0.19865	3	2.73588	0.18432

89
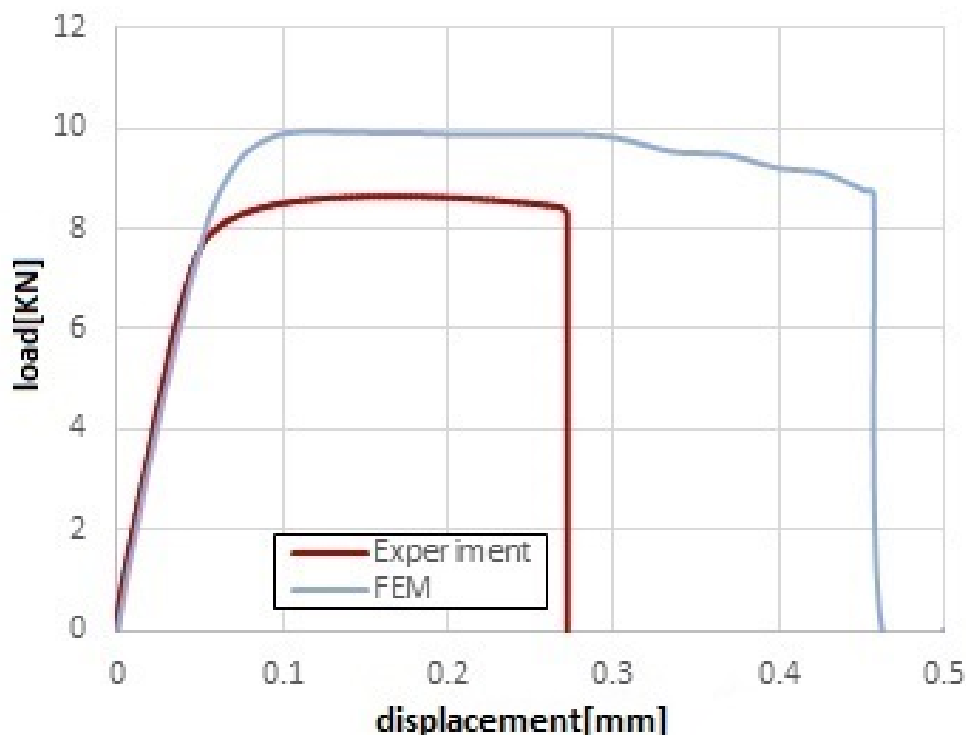
Figure 5.62: Load-displacement data comparison between experiment and numerical simulations in the round specimen with 1.5mm notch radius.

## 5.2.4   Three point bending test(TPBT)

The stress gradient near the notch in the three point bending test is remarkable and is therefore an interesting point to check the ability of the calibrated model. The calibrated model parameters have been used in the finite element models with different mesh sizes. Similar to the other experiments, the load-displacement behavior of the specimen under the test has been used as the main investigator of the models predictions and has been compared with the experimental data. Figure 5.63 shows the load displacement data obtained from the experimental test and the numerical simulations. As mentioned in section 4.3.4 , three different mesh sizes have been used in the finite element models. Figure 5.63 shows the high mesh sensitivity in the results. Decreasing the mesh size significantly affects the failure displacement and decreases its value.

Figure 5.63: Load-displacement data comparison between experiment and numerical simulations in the three point bending test-original model parameters.

The calibrated model fails to exhibit good geometry transferability to the three point bending test Although the predicted failure point for the finite element model with a 0.075mm mesh size is closer to the experimental data than with a 0.2mm mesh size element model, there is still a sufficiently high difference between the numerical and experimental failure displacements. Therefore a new series of damage model parameters has been chosen for the TPBT and another series of finite element simulations has been performed with these new model parameters. Table 5.4 shows the old and new damage model parameter values. Changing the threshold strain ε_{th} strongly affect the behavior of the Lemaitre's damage model. Physically, ε_{th} indicates the value of the strain at which damage starts. In the first series of the damage model parameters the value of the ε_{th} is 0.2, which is high for the three point bending test. Generally the value of the failure strain decreases with the increment of the triaxiality. Therefore the value of 0.2 for the threshold strain means that the failure stain will be greater than 0.2 which according to the existence of the high triaxiality in the notch tip is not very appropriate for the TPBT. According to this fact, the value of the threshold strain has been

91

reduced in the new model parameters, to 0.1. The value of the parameter S has also been reduced according to the reduction of the ε_{th}. The aim of the application of the second series of the model parameters is to show that with appropriate model parameters Lemaitres model is able to better predict the failure point in the three point bending test. The experimental and numerical load-displacement results obtained with new damage model parameters are shown in figure 5.64. The numerical results are closer to the experimental values with the new series of the model parameters. Therefore, even though Lemaitres model fails to include geometry transferability from smooth specimen to the three point bending test it is still able to predict the failure point in the three point bending test with a new calibration for the material parameters. Each calibration is valid for some loading conditions and when the loading conditions are very different from the initial case which has been used for the calibration, new calibrations are necessary.

Table 5.4: Damage model parameters

Original calibration			New calibration		
ε_{th}	S(MPa)	D_{cr}	ε_{th}	S(MPa)	D_{cr}
0.2	25	0.1356	0.1	7.5	0.1356

Also with the new series of the damage model parameters the results are significantly affected by the mesh size. The failure displacement of the 0.2mm mesh size still has 50% difference with the experimental data. However, the 0.1mm and 0.075 mesh sizes gives acceptable results. Figures 5.65 and 5.66 show respectively the accumulative equivalent plastic strain (PEEQ) and the triaxiality evolution with the displacement in the models with different mesh sizes. The values of the PEEQ and the triaxiality have been obtained from the critical elements in the model (the element which fracture starts from) and the value of the displacement represents the total displacement.

Figures 5.65 and 5.66 clearly show the general trend of the evolution of PEEQ and triaxiality are identical. However, with an increase of the mesh size, at a constant displacement, the model with the smaller mesh size predicts higher values for the
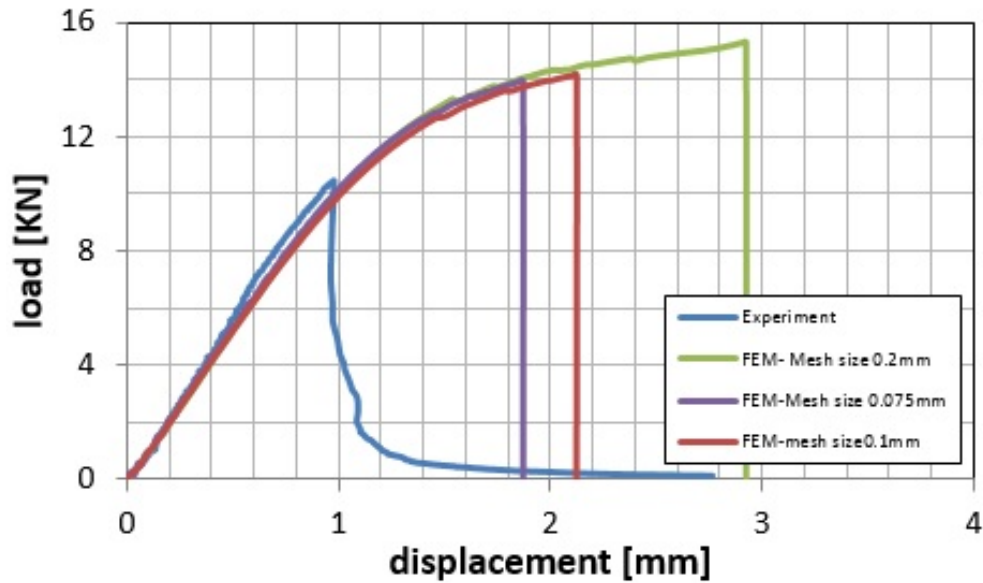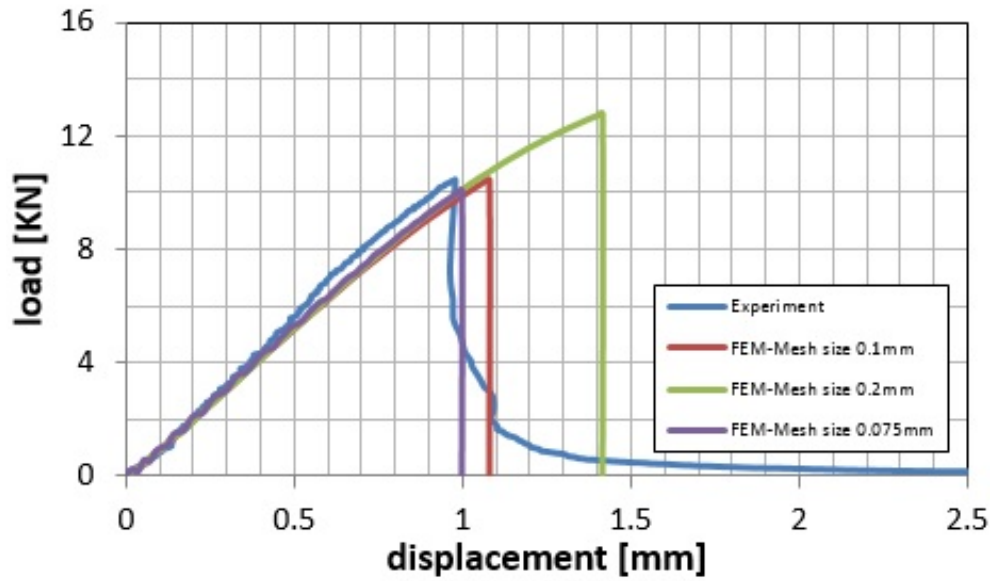
Figure 5.64: Load-displacement data comparison between experiment and numerical simulations in the three point bending test-modified model parameters.
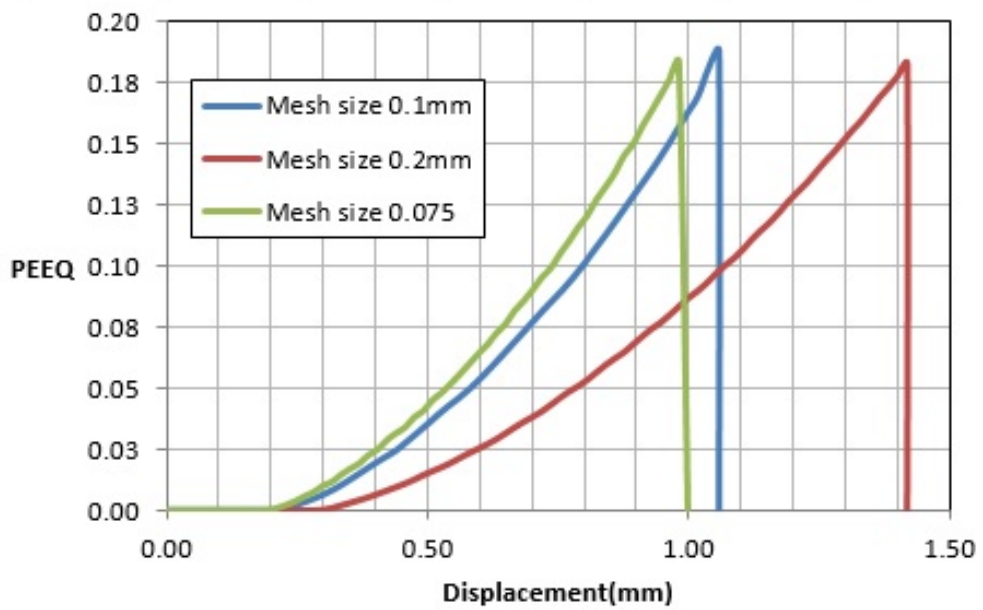
Figure 5.65: PEEQ-displacement evolution in the finite element models of three point bending test with different mesh sizes.
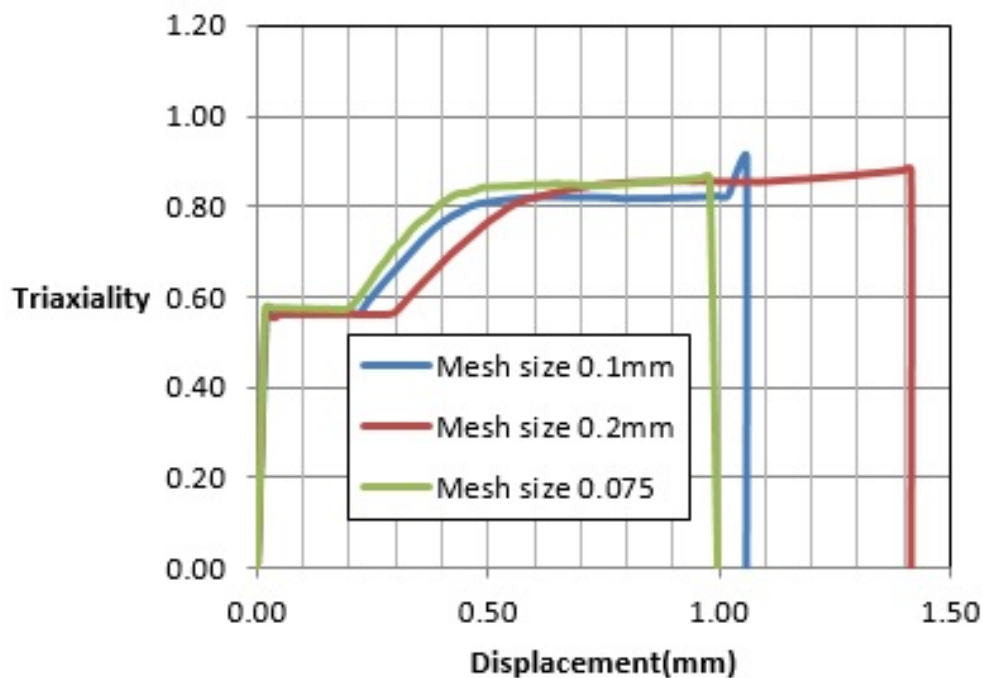
Figure 5.66: Triaxiality-displacement evolution in the finite element models of three point bending test with different mesh sizes.

PEEQ and the triaxiality, which explains the earlier occurrence of the failure in the models with a smaller mesh size. In fact, there is a delay in the results of the models with bigger element size with respect to the models with smaller elements. Due to the high stress state fields in the small areas around the notch tip and the sudden changes of the stress value, bigger elements are unable to simulate these situations as well as smaller elements. Figure 5.67 shows the PEEQ-Stress triaxiality curve obtained from the critical element in the models with the different element size. In this case there is no significant effect of the mesh size. The comparison of figures 5.65 and 5.66 with figure 5.67 shows that to obtain the same value for the triaxiality and PEEQ in the model with the bigger element size, higher values for the load (displacement) are needed. However, the trend of the triaxiality and PEEQ is the same.

Damage distribution contour at the failure point also has been shown in figure 5.68. In the numerical models fracture starts from the central point beneath the notch.
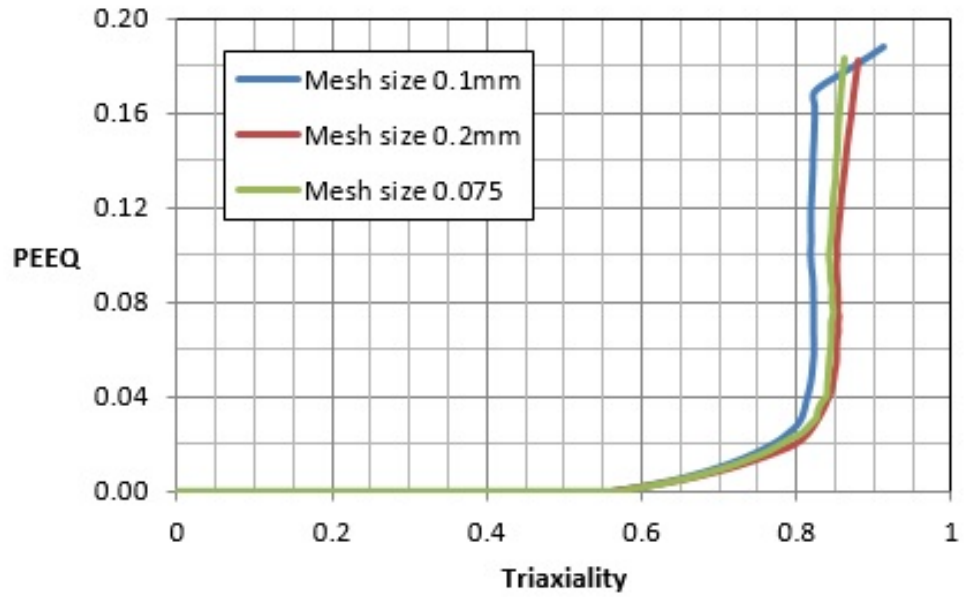
Figure 5.67: PEEQ-triaxiality evolution in the finite element models of three point bending test with different mesh sizes.
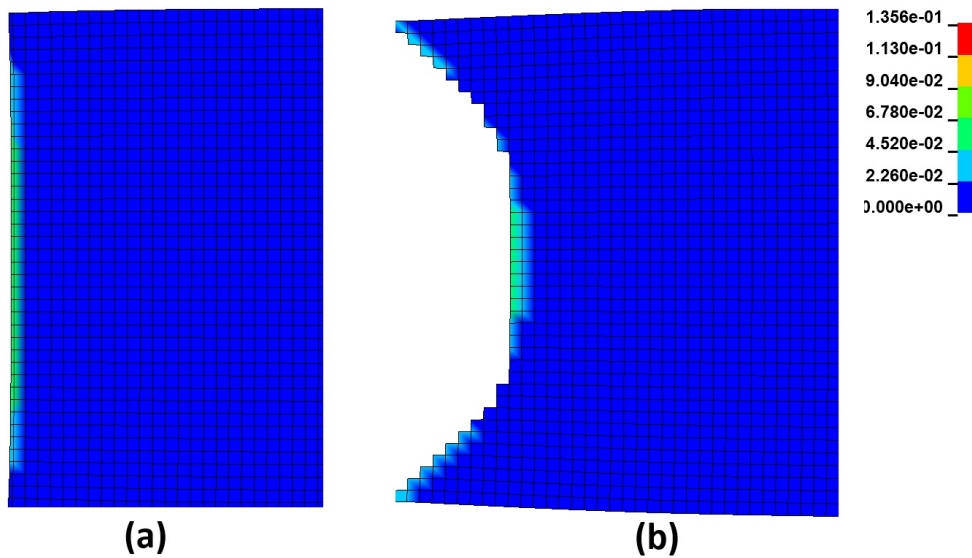
Figure 5.68: Failure initiation in the three point bending test

95
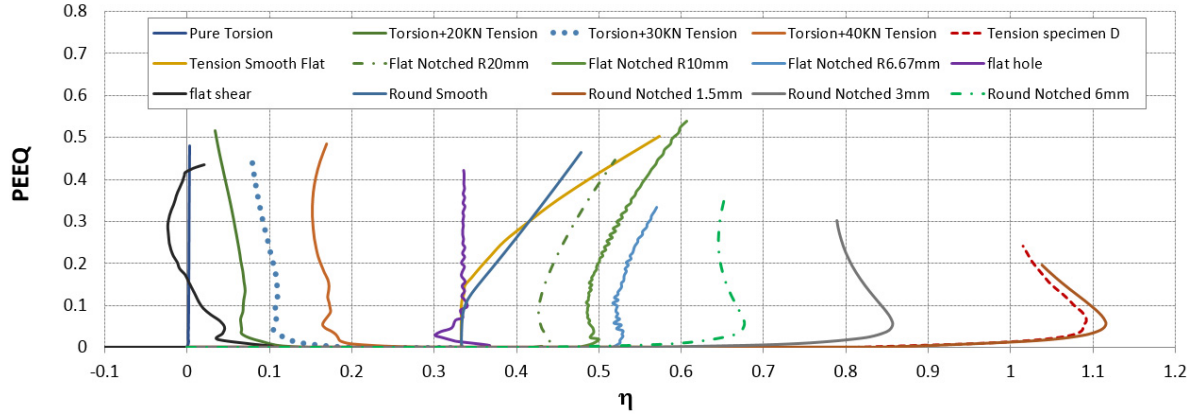
Figure 5.69: Triaxiality-PEEQ curve during the loading in the all of the experiments.

5.3 Evaluation of the experiments based on the stress triaxiality and lode angle

Triaxiality-PEEQ and Lode angle-PEEQ evolution curves for each experiment has been shown in the previous sections. Figures 5.69 and 5.70 show triaxiality-PEEQ and Lode angle-PEEQ curves together for all of the experiments in order to understand the difference in the stress state in the experiments. As it has been mentioned before, these graphs have been obtained from finite element models and extracted from the critical elements (element which failure starts from) at the experimental failure displacement. Average triaxiality and Lode angle for each experiment has been calculated using equations 5.4 and 5.5 and have been shown in figure 5.71. It can be seen that average triaxiality and Lode angle of the performed experiments are distributed in the large area, demonstrating that very different stress states have been investigated. Blue curve in figure 5.71 which demonstrates the relationship between the triaxiality and Lode angle in the plane stress situation has been calculated using equation 5.7 [62]:

$$-\frac{27}{2}\eta(\eta^2 - \frac{1}{3}) = Sin(\frac{\pi\theta}{2}) \tag{5.7}$$

In the Pure torsion test, both the triaxiality and Lode angle values are almost constant during loading and average value is approximately zero which guarantees

96
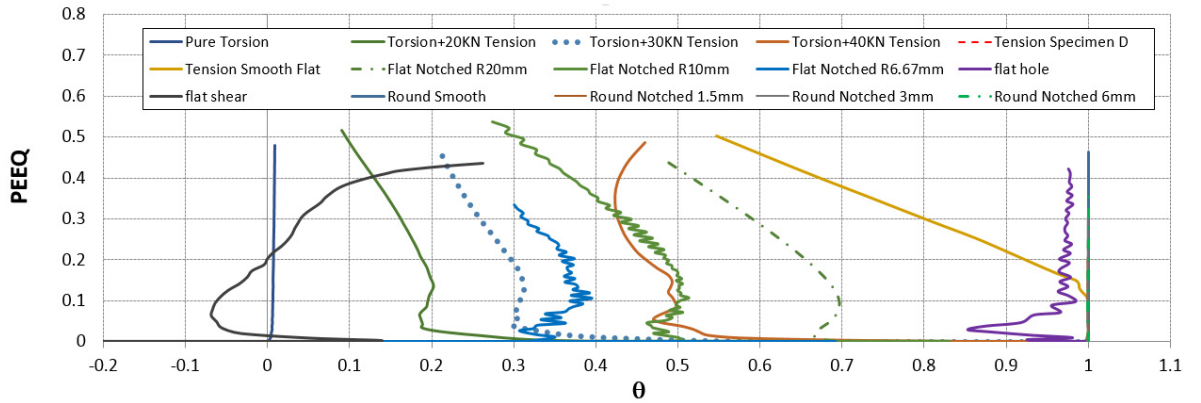
Figure 5.70: Lode angle-PEEQ curve during the loading in the all of the experiments.
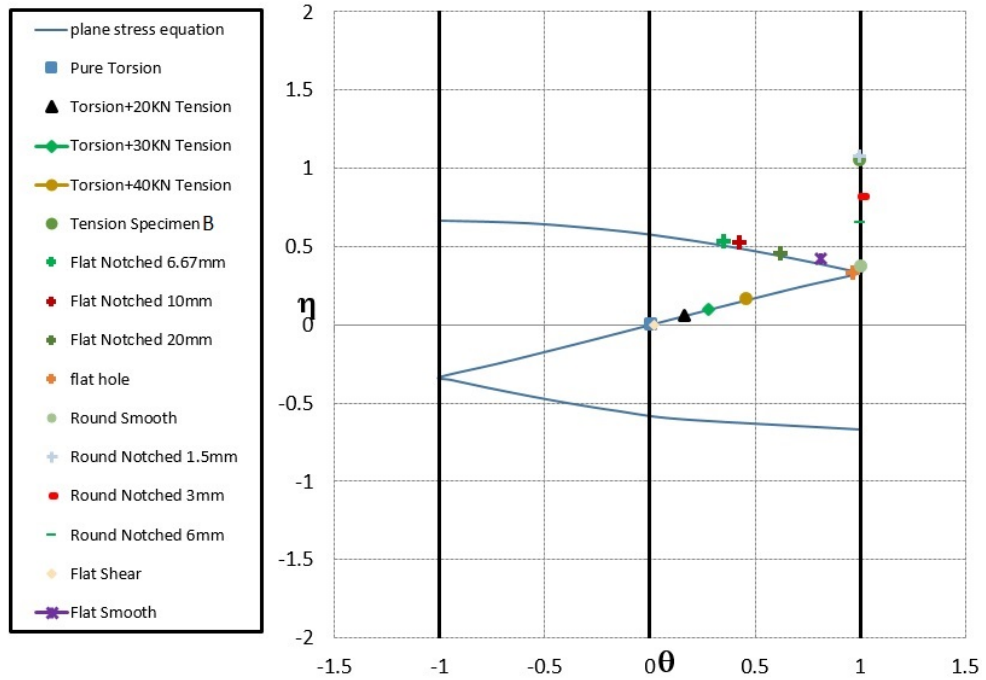
Figure 5.71: Average Lode angle-Triaxiality values in the all of the experiments.

the shear dominant failure in the specimen. In the other torsion tests with pre-applied tension loads (20, 30, 40KN) general trend of the evolution of triaxiality and Lode angle are similar. Although the general trend is the same average values of triaxialty and Lode angle increases by increasing the pre applied tension loads. Average triaxiality varies from 0 to 0.3 which causes failure due to the mixed
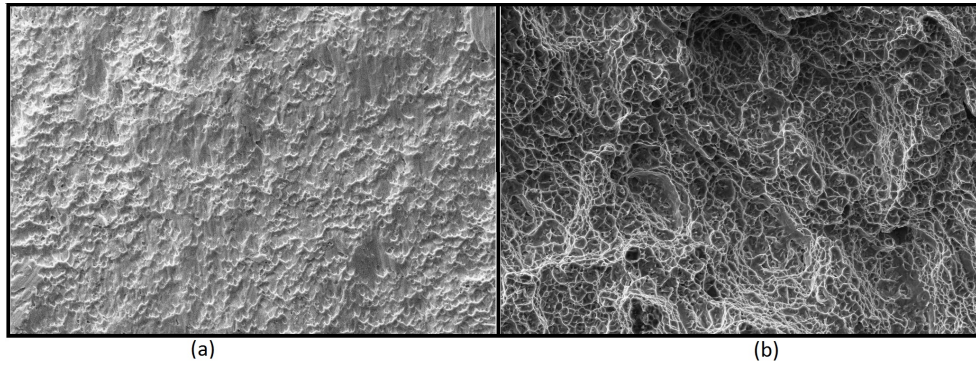
Figure 5.72: SEM photos of the failure surface (a) Torsion+30KN tension Mag.1000X (b) Tensile test of specimen D Mag.1000X.

shear and tension mechanism. Tensile test of the notched specimen B, has a stress state which is different from all of the other tests have been done in the first series of experiments. Both the trend of evolution and average values of triaxiality and Lode angle in the tensile test of the notched specimen B is different from multiaxial torsion tests. Due to the existence of the notch high values of triaxiality and Lode angle are obtained in specimen B. While the stress state is different in specimen B, failure mechanism will be also different from other experiments in the first series. Tensile dominant fracture which occurs with the large number of dimples and microvoids inside the specimen is the governing failure mechanism. Figure 5.72 shows scanning electron microscope(SEM) photos taken from the failure surface of the trosion+30KN tension test and tensile test of specimen B. In the multiaxial torsion tests, failure is characterized by several dimples on the failure surface. No micro cracks exist on the surface and the dimples are relatively uniform in size without the presence of the particularly large dimples. The overall size of surface dimples is smaller in these test specimens compared with flat notched specimens. Sliding effects of the surfaces caused by shear are also evident on the failure surface of the multiaxial torsion tests . The round notched specimen has a medium high triaxiality (around 1). The failure is ductile with typical dimple rupture which indicates that tensile stress is dominant. Many small dimples surrounded by larger ones are clearly visible.

In the second series of experiments which includes the flat specimens shear specimen as it is expected, has average stress triaxiality and Lode angle values which are close to zero and is similar from this point of view to the pure torsion exper-

iment in the first series of tests. However, during the loading in flat shear specimen stress triaxiality and load angle varies which in pure torsion test it is almost constant. In the notched flat (R20, R10 and R6.67) specimens stress triaxiality evolution during the loading has a similar trend but the average value increases by decreasing the notch radius. In these specimens triaxiality varies between 0.4-0.6 which is relatively high and causes tensile dominant failure. In the flat specimen with hole, evolution trend of the triaxiality is different from the notched flat specimens. In the specimen with hole, triaxiality is almost constant during the loading and proportional loading condition exists in the test. On the other hand, in the notched specimens triaxiality exhibits strong variations during the loading. SEM photos of the failure surfaces of flat specimens can also proves the existence of the different failure mechanisms inside the experiments. Figures 5.73 and 5.74 show SEM photos of the failure surface of the flat shear and notched flat specimens respectively. In the notched flat specimens, many dimples of varying size and secondary cracks are present on the failure surface of the specimens. This surface morphology is typical of a mostly ductile fracture and hence it is possible to state that the flat notched specimens have a ductile fracture. However, in some cases the fracture surface exhibits also some partially brittle ruptures even if the fracture is mainly ductile. Among the notched flat specimens, the specimen with a 20mm notch radius which has the smallest triaxiality value, has a more ductile failure surface with less micro cracks on the failure surface. The failure surface of the flat specimen with a hole is quite similar to the notched flat specimens. Also in this case micro cracks are detectable on the failure surface. However, it seems that failure mechanism is more ductile compared with the notched flat specimens (the triaxiality is lower for the flat specimen with a hole). The failure surface of the shear specimen is different from the other flat specimens. Average triaxiality and Lode angle values are close to zero in the shear specimen and therefore very distant from the other tested flat configurations. The shear morphology area is deformed by shear stresses and is stretched along the applied load, with no detectable cracks present on the failure surface.

In the third series of experiments(round smooth, round notch 6mm, round notch 3mm and round notch 1.5mm) all experiments provide Lode angle value which is almost constant during the loading and is approximately equal to 1. These region

(a)   **(b)**
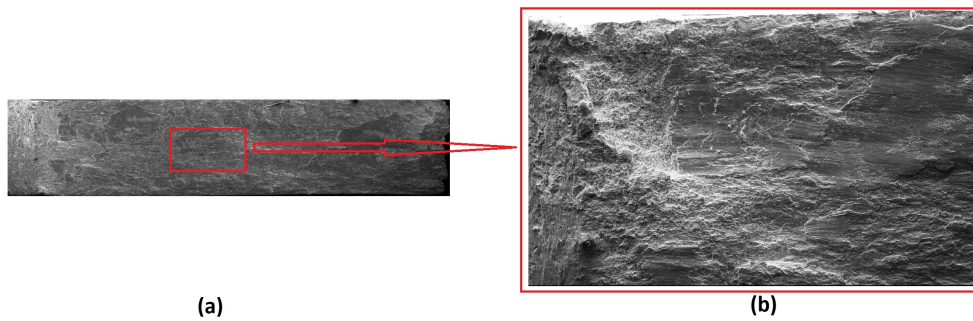
Figure 5.73: SEM photos of the failure surface in shear flat specimen (a)Mag.35X
(b)Mag.150X.

is different from other experiments in the first and second series from the Lode angle point of view. On the other hand, the triaxiality changes strongly in the all of the specimens tested in these series. In all of the round notched specimens triaxiality evolution trend is similar while average value increases with decrement of the notch radius. Round notch specimen with the 1.5 mm notch radius has the minimum fracture strain value. Like notched flat specimen, in the round notch specimens failure mechanisms occurs in the tension dominant region and is due to the micro voids and dimples nucleation and enlargement. Cup-cone fracture has been occurred in the all of the round specimens. Figure 5.75 shows the failure surface of the round specimens.
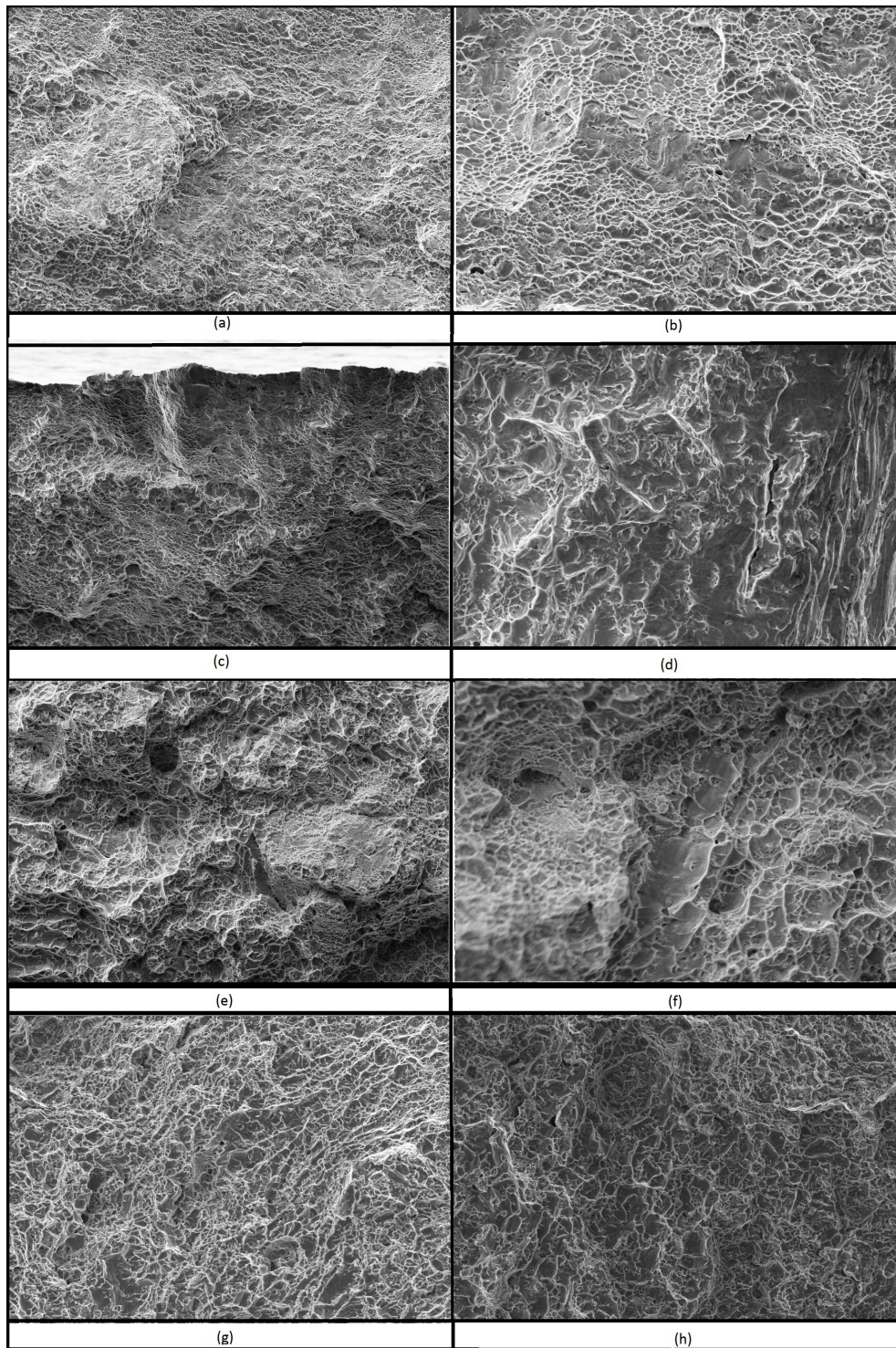
Figure 5.74: SEM photos of the failure surface of flat specimens(a)Notched 20mm 500X(b)Notched 20mm 1200X(c)Notched 10mm 500X(d)Notched 10mm 1200X(e)Notched 6.67mm 600X(f)Notched 6.67mm 1200X(g)Hole 600X(h)Hole 750X.

101
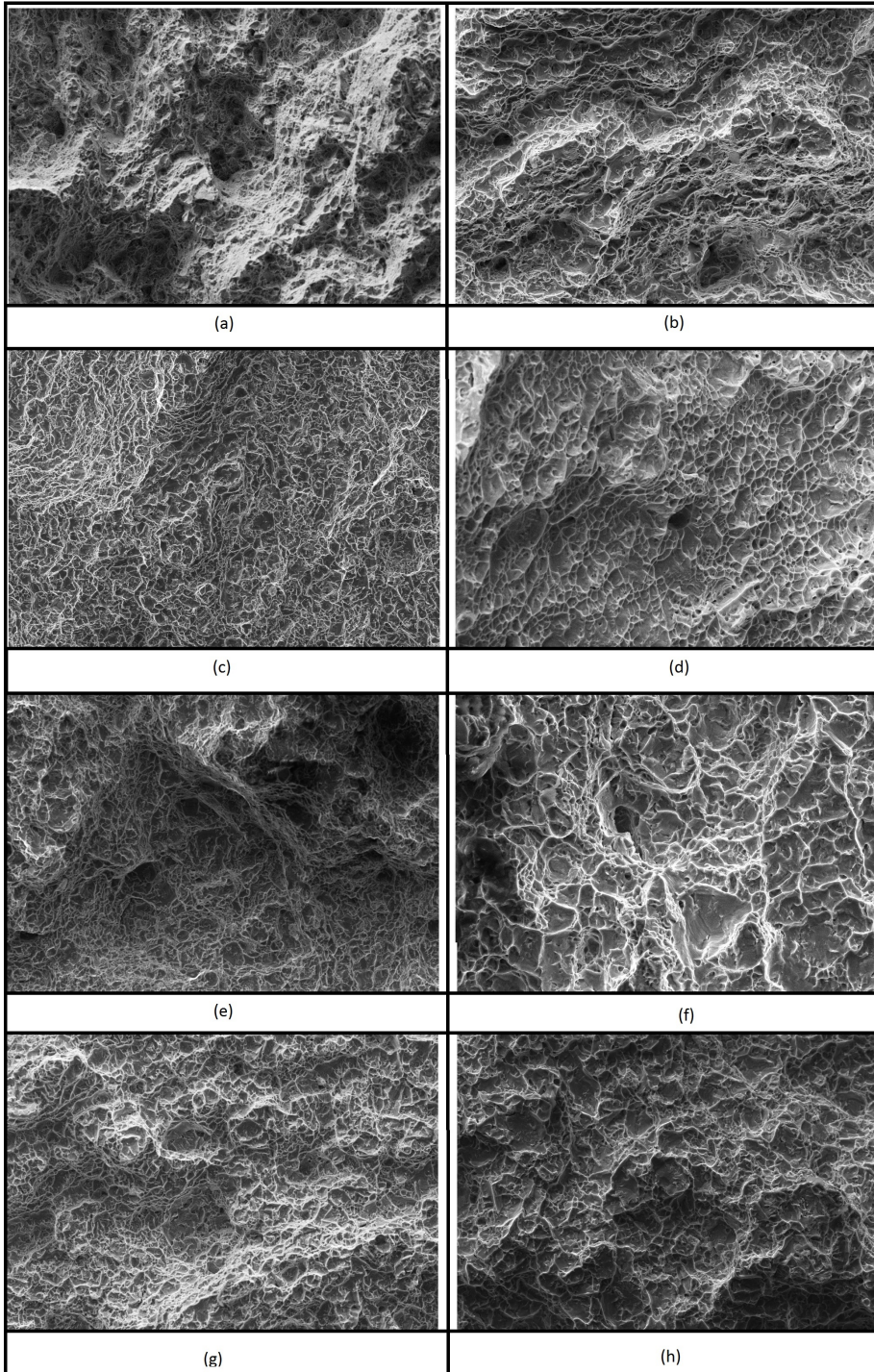
Figure 5.75: SEM photos of the failure surface of round specimens(a)Smooth 500X(b)Smooth 750X(c)Notched 6mm 500X (d)Notched 6mm 1500X(e)Notched 3mm 500X(f)Notched 3mm 1500X(g)Notched 1.5mm 600X(h)Notched 1.5mm 1000X.

5.4 Error analysis of the CDM models predictions

As it can be seen in figures of the previous sections which are related to the comparison between the experimental and numerical load-displacement data, CDM models predictions for the failure displacement are generally different from the experimental results, which shows that changing the geometry affects the damage model parameters calibration and CDM model is not able to predict the failure displacement with the same accuracy of the calibration test. This difference between the numerical and experimental results varies in the different cases, for some very good accuracy is still exist while in other cases results have considerable errors. However, in most of the cases CDM model is still able to predict the failure displacement in a satisfactory way. In order to analyze the experimental and numerical load-displacement data of all experiments together, difference between the experimental failure displacement and the value predicted by the finite element models has been calculated for each test. Figures 5.76 and 5.77 show triaxiality-error and Lode angle-error graphs for CDM model obtained from the comparison between the experiment and numerical models. These data have been obtained from load-displacement graphs presented in the previous sections. Differences between the experimental and numerical failure displacement has been determined for each test and corresponding error has been calculated. These error values has been combined with the relevant average triaxiality and Lode angle of each experiment. Red line in this figures demonstrate 20% error limit. As it can be seen in figures 5.76 and 5.77 in most of the cases error value for the CDM models is less than 20% which guaranties a reasonable accuracy of the above mentioned model for the different loading conditions. In some cases model even can predict the failure displacement with very high accuracy (less than 5% error). However, in two regions of triaxiality CDM model fails to provide appropriate predictions and the error is more than 20%, and in some cases reaches to 67%. The first region is the one between $0.15 - 0.35$ triaxiality (First series of experiments: torsion+40KN tension). Experimental test of the torsion+40KN tensile load which has the average triaxiality of 0.164 has biggest error (35%) in this region. As it can be seen in figures 5.76 and 5.77, error of the CDM model predictions in the other two experimental points which are close to this critical point is also relatively high (17.5 and 21.7%). A possible explanation for this error can be the existence of a discontinuity in the fracture locus of the material in this region. Some researches has

shown that effect of triaxiality on the fracture strain is not continuous ([8], [9], [12]) and around this triaxiality range there is a sharp discontinuity in the fracture locus and the general trend of the evolution of fracture strain with triaxiality changes. This transient region is characterized by a failure mechanism changing from shear dominant failure to the tensile dominant and failure mechanics is a combination of shear and tensile. Also in the SEM photo of the torsion+30KN tension test in figure 5.72 it can be seen that number of microvoids in the fracture surface are more than shear specimen and less the specimen B with notch. This phenomenon may lead to some additional errors in the predictions of the model when the loading condition is close to this region.
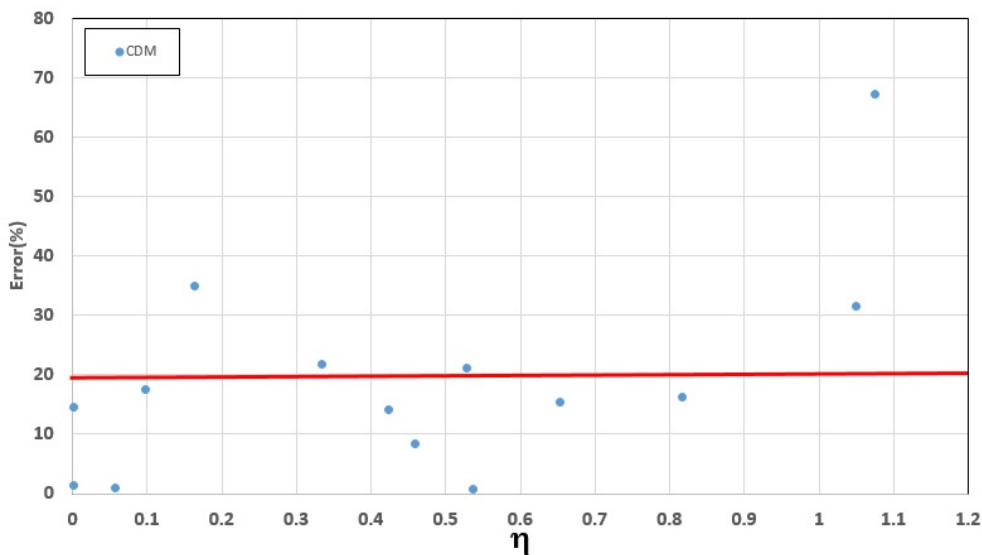
Figure 5.76: Triaxiality-error graph of the predictions of the CDM model for the failure displacement of experiments.

Other region which model has big error in the prediction of the failure displacement, is the experiments regarding to very high triaxiality around 1 (First series experiments: specimen B and third series experiments: round specimen with 1.5mm notch). CDM model has respectively 31.25% and 67.27% error in this point. This error can be related to the experimental test which has been used in order to calibrate CDM model. As it has been explained in section 4.2 tensile test of the round smooth specimen has been used for the calibration of the CDM specimen. High
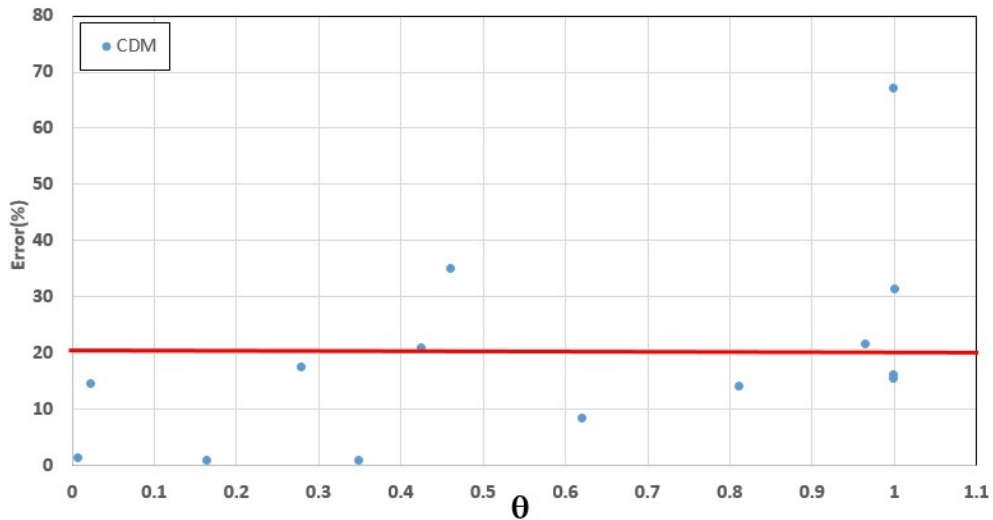
Figure 5.77: Lode angle-error graph of the predictions of the CDM model for the failure displacement of experiments.

triaxiality value in the notched round specimens is so far from the stress state of the calibration test and can be the potential reason for this error in the models prediction. In fact these error shows when it comes to the practical applications of the Lemaitre CDM model model, experimental tests which are used for the calibration is important and it is better to use damage models with more caution in the loading conditions which are very far from the calibration conditions. Having knowledge about the stress state of the component which is the aim of investigation therefore plays a crucial role in the application of the CDM model.

5.5 Effect of triaxiality and Lode angle on the plasticity constitutive law

Since the experimental results obtained in 1931 by Taylor and Quinney [63], the most spread yielding criterion is the Von Mises and the most popular continuum plasticity model is the J2-flow theory. This model can be applied with satisfactory results to many different metals but for some materials its application can lead to an inaccurate material response. The reasons for this discrepancy can be mainly attributed to the hypothesis of the model, which states that the hydrostatic stress

(first invariant of the stress tensor, J1) and the third invariant of the stress deviator (lode parameter, J3) are assumed to have no effect on plasticity. According to [64], the hydrostatic pressure can affect the size of the yield surface, whereas the lode angle parameter is responsible for its shape. The 1045 steel is an example of a metal which has no relevant hydrostatic pressure and lode angle dependence [44]. However, hydrostatic stress and especially lode angle play an important role in the plasticity of other metals like aluminum alloys such as 2024-T351 and 2A12-T4 [64],[44]. Comparison of the experimental and numerical load-displacement results obtained in this research and reported in the previous sections also clearly shows that the initially calibrated constitutive law cannot perfectly predict the experimental load-displacement data in all experiments and changing triaxiality and lode angle affects the constitutive law. Effect of triaxiality and lode angle on the constitutive law is the main reason of the difference between the experimental and numerical load-displacement data obtained in this research and damage model has no significant role in this difference before failure point. As an example to show more clearly variation of the constitutive law by changing the stress triaxiality and Lode angle, special constitutive law has been calibrated for each experiment of the second series of tests which include flat specimens (see section 3.4) in this section. Similar to the main constitutive law ls-opt software has been used and for each experiment parameters of the constitutive law has been obtained in order to minimize error between numerical and experimental load-displacement results. General shape of the constitutive law is similar to equation 5.3 and no damage model has been considered in this case. Table summarizes parameter obtained for the constitutive law for each of the second series experiments. True stress-true strain graphs according to these constitutive laws and a comparison between the experimental load-displacement data and the numerical prediction has been shown respectively in figures 5.78 and 5.79. As it can bee seen in table 5.5 and figure 5.79 constitutive laws for different experiments are generally different with each other which demonstrate the effect of the stress triaxiality and Lode angle on the constitutive law. Due to the fact that all of constitutive law in this section have been obtained separately from the optimization process, in all cases experimental and numerical load-displacement data fit perfectly to each other (figure 5.78).

it worth to mention that variation of the constitutive law might affect also the failure point in the CDM model due to the existence of the coupling between damage and plasticity in these kind of models. However, from a practical point of view,

once a model has been calibrated, it will be applied to the other loading conditions and aim of this research is to investigate the errors that may exist in the predictions of the damage models including errors due to the variation of the plasticity.

Table 5.5: Damage model parameters

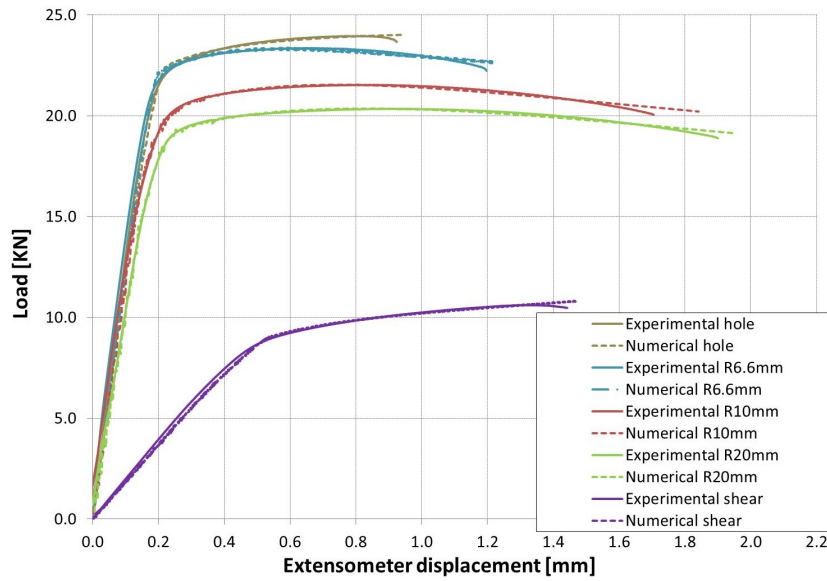|	Notch radius 6.67mm	Notch radius 10mm	Notch radius 20mm	Shear	Specimen with hole
σ_{y0}[MPa]	977.69	757.24	748.2	996.19	937.6
Q1[MPa]	72.69	129.9	139.7	331.66	96.95
C1[MPa]	26.92	19.52	18.95	4	0.0212
Q2[MPa]	30	198.15	263.24	1.5	163.43
C2[MPa]	30.47	293.7	554.73	600	6.24

Figure 5.78: Comparison between experimental and numerical load-displacement results obtained from optimized constitutive laws for flat specimens.
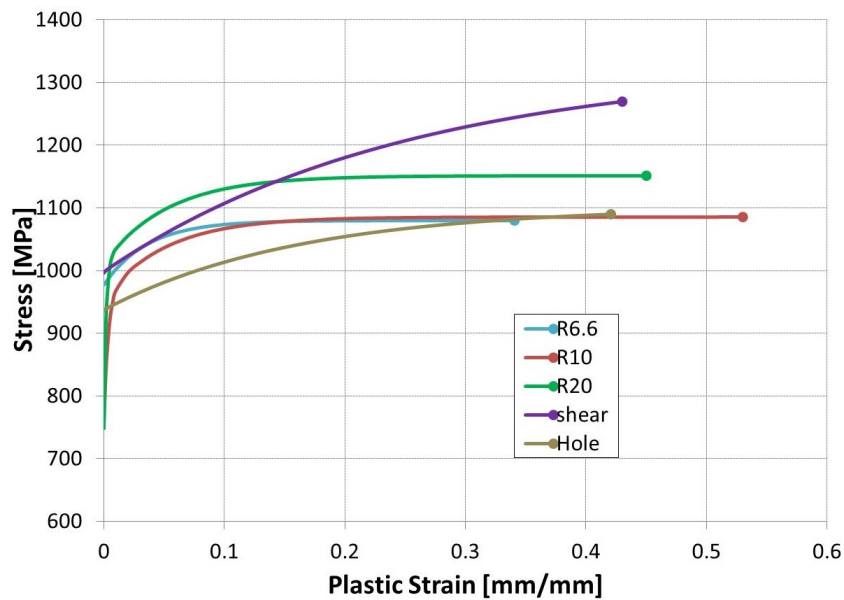
Figure 5.79: True stress-true strain curves for the flat specimens:obtained from optimized constitutive laws.

Chapter 6

Conclusions

Lemaitre's continuum damage mechanics model has been investigated in this research under different loading conditions. All specimens have been made from ti-6Al-4V titanium alloy which is a commonly used material in the different applications specially aerospace industry. Lemaitre's continuum damage mechanics model and plasticity constitutive law with five parameters, has been calibrated for ti-6Al-4V titanium alloy and material model parameters has been obtained using inverse engineering technique and uni-axial tensile test of the round smooth specimen. A comprehensive experimental test program has been performed on the specimens with different geometries and loading conditions including multi-axial torsion and uni-axial tensile tests on the smooth and notched round and flat specimens. Finite element model of all of experiments has been made using Ls-Dyna and Abaqus commercial softwares. Load-displacement data obtained from the finite element models has been compared with the experimental results in the all cases. Comparison of the failure displacement in numerical models and experiments showed that Lemaitre's continuum damage mechanics model accuracy changes by changing the geometry and loading conditions and the same accuracy of the calibration can not be achieved for the other experiments. However, Lemaitre's model was still able to predict the failure displacement in most of the cases with quite good accuracy and less than 20% error. By changing the stress state which can be represented by variation of the stress triaxiality and lode angle, accuracy of the predictions of model for the failure displacement changes. In the two region, model predictions for the failure displacement has errors bigger than 20%. First region is the triaxiality region around 0.15-0.35 and lode angle around

0.3-0.5. Combination of the shear and tensile loads is responsible for the failure in this region and transition in the failure mechanism occurs in this region. Second region which models predictions has big errors is related to the experiments with high value of triaxiality and lode angle (bigger than 1). Very different stress state in this region in compare with calibration condition can be the possible reason for big error of the model. Lemaitre's model was also able to predict the critical points in all experiments properly.

Analyze of the stress state in the experiments by calculating the average stress triaxiality and lode angle demonstrated that different loading conditions which leads to different failure mechanism has been created in the experiments. SEM photos of the failure surface of the experiments also shows different failure phenomenons in the experiments.

It has been shown by comparison of the numerical and experimental load-displacement data that changing the triaxiality and lode angle clearly affect the plasticity constitutive law which normally supposed to be independent from the geometry and loading conditions. This effect has to be taken into consideration in the practical applications.

For the three point bending test, model was not able to achieve a reasonable accuracy in the prediction of the failure displacement with original calibration obtained from the smooth specimen however new parameters for the model can improve the accuracy of the model. Very high mesh sensitivity of the results also has been observed for the three point bending test.

Investigation of the failure phenomena from the micro-structural point of view is an interesting topic for the future studies. especially in the transient region between the shear dominant and tensile dominant failure more studies will be useful to understand more clear the physical phenomena. More experiments in this region will help to improve our knowledge about behavior of the model in this region and potential errors of its applications. Changing the constitutive law indirectly affects damage model results which in some cases may lead to additional errors it is also interesting to investigate effect of variation of the constitutive law on the predictions of the damage model.

Bibliography

[1] G.R.Johnson, W.H.Cook W, *Fracture characteristics of three metals subjected to various strains, strain rates, temperatures and pressures*, Engineering fracture mechanics, 1985, Vol.21, 31.

[2] J.R.Rice, D.M.Tracey, *On the ductile enlargement of voids in triaxial stress fields*, Journal of mechanics and physics of solids, 1969, Vol.17, 201.

[3] G.Leroy, J.D.Embury, G.Edward and M.F.Ashby, *A model of ductile fracture based on the nucleation and growth of voids*, Acta metal, 1981, Vol.29, 1509.

[4] M.G.Cockcroft, D.J.Latham, *Ductility and the workability of metals*, Journal Institute of Metals, 1968, 96, 33.

[5] M. Ayada, T.Higashino, K. Mori, *Central bursting in extrusion of inhomogeneous materials.* In: Proceedings of the First ICTP, 1984, Advanced technology of plasticity, Vol. 1, 553.

[6] P.Brozzo, B.Deluca, R.Rendina, *A new method for the prediction of formability limits for metal sheets*, sheet metal forming and formability Proceedings of the seventh biennial congress of international deep drawing research group, Amsterdam, Netherlands.

[7] M.Oyan, *Criteria of DF strain*, JSME 15, 1507-1513.

[8] Y.Bao, T.Wierzbicki, *A comparative study on various ductile crack formation criteria*, Transactions of the ASME, 2004, Vol. 126, 314.

[9] Y.Bao, T.Wierzbicki, *On the fracture locus in the equivalent strain and stress triaxiality space*, International Journal of mechanical science, 2004, Vol.46, 81.

[10] Y. Bai, T.Wierzbicki, *A new model of metal plasticity and fracture with pressure and lode dependence*, International journal of plasticity, 2008, Vol.24, 1071.

[11] Y.Bai, T.Wierzbicki, *Application of extended Mohr-Coulomb criterion to ductile fracture*, International journal of fracture, 2010, Vol.161, 1.

[12] M.Giglio, A.Manes, F.Vigano, *Ductile fracture locus of Ti-6Al-4V titanium alloy*, International journal of mechanical science, 2012, Vol.5 , 121.

[13] M.Giglio, A.Manes, F.Vigano, *Numerical simulation of the slant fracture of a helicopter's rotor hub with ductile damage failure criteria*, Fatigue and fracture of engineering materials and structures, 2012, Vol.35, 317.

[14] A.Gilioli, A.Manes, M.Giglio, *Numerical simulation of a fracture toughness test of an Al6061-T6 aluminium alloy using a ductile criterion*, Mechanics Research Communications, In Press

[15] A.Gilioli, A.Manes, M.Giglio, *Numerical simulation of a fracture toughness test of an Al6061-T6 aluminium alloy using a ductile criterion*, Mechanics Research Communications, In Press

[16] X.Gao, G.Zhang, Ch.Roe, *A study on the effect of the stress state on ductile fracture*, International journal of damage mechanics, 2010, Vol.19, 75.

[17] M.Brunig, O.Chyra, D.Albrecht, L.Driemeier, M.Alves, *A ductile damage criterion at various stress triaxialities*, International Journal of Plasticity,2008, Vol.24, 1731.

[18] A.Zadpoor , J.Sinke, R.Benedictus, *Formability prediction of high strength aluminum sheets*, International Journal of Plasticity, 2009, Vol.25, 2269.

[19] G.Chiantoni, N.Bonora, A.Ruggiero, *Experimental study of the effect of triaxiality ratio on the formability limit diagram and ductile damage evolution in steel and high purity copper*, International journal of material forming, 2010, Vol. 3, 171 .

[20] A.L. Gurson, *Continuum theory of ductile rupture by void nucleation and growth, I. Yield criteria and flow rules for porous ductile media*, Journal of engineering materials and technology, 1977, Vol.99, 2.

[21] V. Tvergaard, *Material failure by void growth of coalescence*, Advanced applied mechanics, 1990, Vol.27, 83.

[22] J.Lemaitre, *A continuous damage mechanics model for ductile fracture*, Journal of engineering materials and technology, 1989, Vol.107, 83.

[23] L.M. Kachanov, *Time of the rupture process under creep condition*, TVZ Akad, S.S:r., OTD Ted Nauk, 1958, 8.

[24] N. Bonora, *A nonlinear CDM model for ductile failure*, Engineering fracture mechanics, 1997, Vol.58, 11.

[25] S. Chandrakanth and P.C. Pandey, *An isotropic damage model for ductile material*, Engineering fracture mechanics, 1995, Vol.50, 457.

[26] W. Tai and B.X. Yang, emph*A new damage mechanics criterion for ductile fracture*, Engineering fracture mechanics, 1987, Vol.27, 371.

[27] H.W. Tai, *Plastic damage and ductile fracture in mild steels*, Engineering fracture mechanics, 1990, Vol.36, 853.

[28] C.L. Chow and J. Wang, *Anisotropic theory of continuum damage mechanics for ductile fracture*, Engineering fracture mechanics, 1987, Vol.27, 547.

[29] J. Lemaitre, R. Desmorat, M. Sauzay, *Anisotropic damage law of evolution*, European journal of mechanics-A/solids, 2000, Vol.19, 187.

[30] G.Z. Voyiadjis, T. Park, *Kinematics of damage for finite strain elasto-plastic solids*, International journal of engineering science, 1999, Vol.37, 803.

[31] X. Yang, N. Li, Z. Jin and T. Wang, *A continuous low cycle fatigue damage model and its application in engineering materials*, International journal of fatigue, 1992, Vol.19, 687.

[32] F.M.A. Pires, J.M.A.C. De Sa, L.C. Sousa and R.M.N.Jorge, *Numerical modeling of ductile plastic damage in bulk metal forming*, International journal of mechanical sciences, 2003, Vol.45, 273.

[33] Perzyna, *Recent Advances in Applied Mechanics*, Academic Press: New York, 1966, 243(Chapter 9).

[34] A.Pirondi, N. Bonora, *Modeling ductile damage under fully reversed cycling*, Computational materials sciences, 2003, Vol.26, 129.

[35] J.B.Leblond, G.Perrin,J.Devaux, *An improved Gurson-type model for hardenable ductile metals*, European journal of mechanics. A, Solids, 1995, Vol.14, 499.

[36] D.Steglich, A.Pirondi, N.Bonora, W.Brocks, *Micromechanical modelling of cyclic plasticity incorporating damage* International Journal of Solids and Structures, 2005, Vol.42, Issue 2, 337.

[37] B. Bhattacharya and B.Ellingwood, *A new CDM-based approach to structural deterioration*, International journal of solids and structure, 1999, Vol.36, 1757.

[38] J. Jing, G. Meng, Y. Sun, S. Xia, *An effective damage mechanics model for creep-fatigue life assessment of a steam turbine rotor*, International journal of pressure vessels and piping, 2003, Vol.80, 389.

[39] D.R. Hayhurst, F. Vakili-Tahami and J.Q. Zhou, *Constitutive equations for time independent plasticity and creep of 316 stainless steel at* $550°C$, International journal of pressure vessels and piping, 2003, Vol.80, 97.

[40] J. Choung, *Comparative studies of fracture models for marine structural steels*, Ocean Engineering, 2009, Vol.36, 1164.

[41] T. Coppola, L. Cortese, P. Folgarait, *The effect of stress invariants on ductile fracture limit in steels*, Engineering fracture mechanics, 2009, Vol.76, 1288.

[42] T. Wierzbicki, Y.Bao, Y.W.Lee, Y.Bai, *Calibration and evaluation of seven fracture models*, International journal of mechanical sciences, 2005, Vol.47, 719.

[43] M.Huber, *Contribution to foundation of strength of the material*(in Polish translated to English by professor.M.Zyczkowski in connection with M.T.Huber century symposium, Krakov, August 2004), Czasopismo Techniczne, Lwow 1904, Vol.22,81.

[44] T.Wierzbicki, L.Xue, *On the effect of the third invariant of the stress deviator on ductile fracture*, Impact and Crashwothiness Lab Report 136, 2005.

[45] L.Xue *Damage accumulation and fracture initiation in uncracked ductile solids subject to triaxial loading*, International journal of solids and structures, 2007, Vol.44, Issue.16, 5163.

[46] M.L.Wilkins, R.D.Streit, J.E.Reaugh *Cumulative-strain-damage model of ductile fracture: simulation and prediction of engineering fracture tests*. Technical report UCRL-53058, Lawrence Livermore National Laboratory; October 1980.

[47] Y.W.Lee, *Fracture prediction in metal sheets*, Ph.D. thesis, Campridge, MA: Department of ocean Engineering, Massachusetts institute of Technology, 2004.

[48] N.Bonora, A.Ruggiero, L.Esposito, D.Gentile, *CDM modeling of ductile failure in ferritic steels: Assessment of the geometry transferability of model parameters*, International Journal of Plasticity, 2006, Vol.22, 2015.

[49] H.Li, M.W.Fu, J.Lu and H.Yang, *Ductile fracture: Experiments and computations*, International journal of plasticity, 2011, Vol.27, 147.

[50] F.A.Freudenthal, *The inelastic behavior of solids*, Wiley, 1950, New York.

[51] S.Katani, F.Madadi, M.Atapour, S.Ziaei Rad, *Micromechanical modelling of damage behaviour of Ti6Al4V*, Materials and Design, 2013, Vol.49, 1016.

[52] J.Lemaitre, *A course on damage mechanics*, Second edition, Springer, 1996.

[53] J.Lemaitre, R.Desmorat, *Engineering damage mechanics*, Springer, 2005.

[54] E.A.de Souza Neto, A fast, *One-equation integration algorithm for Lemaitre ductile damage model*, Communcations in numerical methods in engineering, 2002, Vol.18, 541.

[55] I.Doghri, *Numerical implementation and analysis of a class of metal plasticity models coupled with ductile materials*, International journal of numerical methods in engineering, 2001, Vol.50, 29.

[56] J.C. Simo, T.J.R. Hughes, *Computational Inelasticity*, Springer, 1998.

[57] M.Jr. Vaz, D.R.J. Owen, *Aspects of ductile fracture and adaptive mesh refinement in damaged elasto-plastic materials*, International journal of numerical methods in engineering, 2001, Vol.50, 29.

[58] http://www.aerospacemetals.com/titanium-ti-6al-4v-ams-4911.html.

[59] http://cartech.ides.com/datasheet.aspx?i=101E=269.

[60] C. Mapelli, A. Manes, M. Giglio, D. Mombelli, L. Giudici, C. Baldizzone and A. Gruttadauria, *Survey about effects of shot peening conditions on fatigue performances of Ti-6Al-4V titanium alloy mechanical specimens featured by different cross-section geometries*, Materials science and technology, 2012, Vol.28, 543. .

[61] M.Dunand and D.Mohr, *Hybrid experimental-numerical analysis of basic ductile fracture experiments for sheet metals*, International journal of solids and structures, 2010, Vol.47, 1130.

[62] A.M. Beese, M.Luo, Y.Li, Y.Bai, T. Wierzbicki, *Partially coupled anisotropic fracture model for aluminum sheets*, Engineering fracture mechanics, 2010, Vol.77, 1128.

[63] G.I. Taylor, H.Quinney, *The plastic deformation of metals*, Philos Trans R Soc, 1931, Vol.230, 323.

[64] F. Yang, Q. Sun, W. Hu, *Yield criterions of metal plasticity in different stress states*, Acta Metall. Sin.(Engl. Lett.), 2009, Vol.22, 123.